Durham E-Theses

Optical Trapping and Binding of Colloidal Microparticles in Evanescent Waves

WONG, LUEN,YAN

How to cite:

Use policy

Optical Trapping and Binding

of Colloidal Microparticles

in Evanescent Waves

Luen Yan Wong

A thesis presented for the degree of
Doctor of Philosophy

Durham
University

Department of Chemistry
Durham University

February 2012

Abstract

Optical trapping of colloidal microparticle arrays in evanescent fields is a relatively new area of study. Optically driven array formation is a complex and fascinating area of study, since light mediated interactions have been shown to cause significantly different behaviour for multiple particles when compared with the behaviour of a single particle in an optical field.

Array formation was studied with interference fringes in the counterpropagating evanescent fields so as to investigate the effect of a periodic trapping potential. A subtle balance between optical trapping and optical binding forces is shown to produce modulated lines and arrays. Optically trapped colloidal arrays were also studied in the absence of interference fringes, by using either orthogonally polarised laser beams or a beam delay line. When interference fringes were absent, the formation of arrays was mainly due to gradient forces and optical binding. The experimental studies presented here include the optical trapping of dielectric soft and hard spheres, Au colloids, and Janus particles.

Publications

- L. Y. Wong and C. D. Bain, "Optical trapping and binding in evanescent optical landscapes", in Optical Trapping and Optical Micromanipulation VI; K. Dholakia and G. C. Spalding editors; Proc. SPIE 2009; Vol. 7400.
- J. M. Taylor, L. Y. Wong, C. D. Bain, G. D. Love, "Emergent properties in optically bound matter", Optics Express, 2008, **16**, 6921-6929.

Acknowledgements

Contents

1. Introduction

1.1. Motivation

This thesis investigates phenomena occurring when multiple particles are confined within counterpropagating evanescent fields generated by total internal reflection (TIR) at a glass-water interface. The aim is to explore experimentally the effects of light-mediated interactions that occur between trapped particles (*optical binding*). Multiple particle interactions are often complex and computationally demanding, and so experimental observations continue to challenge our understanding of the observed phenomena.

Optical binding interactions are an important consideration for many optical trapping applications, since they are non-negligible when compared to the optical forces arising from incident beams.[1]

1.2. A brief history of optical trapping and binding

Radiation forces were first postulated 400 years ago by Kepler, who studied the laws of planetary motion and suggested that light-matter interactions were responsible for the tails of comets pointing away from the sun. Later, Maxwell's 19th century work on electromagnetism states that "in a medium in which waves are propagated there is a pressure normal to the waves and numerically equal to the energy in unit volume." This prompted Nichols and Hull to attempt the measurement of radiation pressure in 1901,[2] but it was not until the advent of coherent light sources in the 1960s that allowed Ashkin's groundbreaking work on optical micromanipulation. In 1970, Ashkin reported that microparticles were drawn to the centre of a focused laser beam, and then moved in the direction of propagation of that light.[3] *Optical trapping* was then realised by using two beams for the stable confinement of microparticles. Ashkin and co-workers then proceeded to demonstrate stable trapping and manipulation of a microparticle using a single high numerical aperture laser

beam, a technique now known as *optical tweezing*.[4]

When considering the optical trapping forces due to a highly focused beam of wavelength λ acting on a particle of radius a, it is intuitive to consider either one of these size limiting regimes: *ray optics* in which a large particle acts as a lens ($a > 5\lambda$), or *Rayleigh* in which the particle is represented by an induced point dipole ($a < \lambda/10$). Light reflected by a particle experiences a change in momentum that drives the particle in the direction of propagation of the incident beam (i.e. an axial *scattering force*). In the Rayleigh regime, movement transverse to beam propagation is due to the *gradient force*. A dipole moves along an electric field gradient (*e.g*. due to the high numerical aperture of a focused beam) to minimise its potential energy, which occurs at a point where the electric field is the greatest. Gradient forces thus impose on-axis confinement on optically trapped particles.[5] The ray optics model predicts the same optically induced behaviour due to the reflection and refraction of light at the particle surface. For particles which are similar in size to the incident wavelength, an exact treatment uses Mie-Debye theory to expand the scattered electromagnetic field about the particle surface via vectorial spherical wavefunctions (*i.e*. non-trivial and computationally demanding).

The implications of Ashkin's seminal work have been far-reaching in providing new tools for the manipulation of living cells, organelles within cells [6] and DNA, [7] and as a powerful technique that can be integrated with microfluidics[8-10] and fluorescence microscopy.[11] Optical trapping of multiple particles has been extended to two- and three-dimensions using liquid crystal spatial light modulators (SLM) to holographically generate an array of optical tweezers.[12-14]

1.2.1. Transverse optical binding

Optical binding interactions between two optically trapped dielectric spheres were first reported by Burns *et. al.* in 1989. [15, 16] Multiple particles were trapped in a plane transverse to the propagation of an ellipsoidal beam (Figure 1.1), and were observed to statistically prefer separations that were multiples of the wavelength of the applied field. The mechanism for optical binding, in this case, is an interference effect between the light scattered by the particles and the applied field. The forces on optically bound particles will then be different from the forces experienced by an optically trapped particle in isolation.
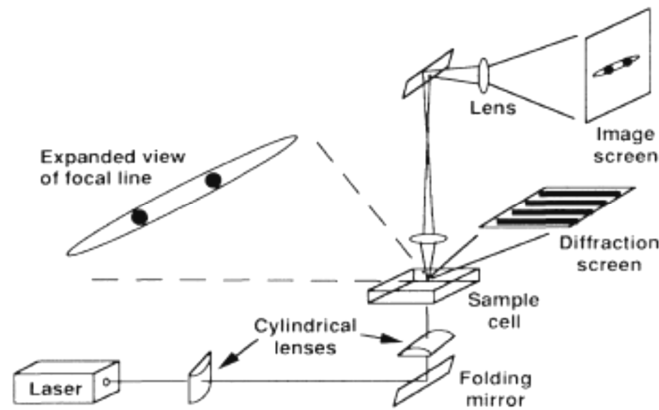
Figure 1.1: Experimental setup for transverse optical binding as performed by Burns, Fournier and Golovchenko in 1989. [15, 16]

In the experiments by Burns *et. al.*, the diameter of the trapped polystyrene particles (1.43 μm) were several times the wavelength of the trapping beam (0.387 μm in water). The same trapping configuration was employed by Mohanty *et. al.* for particles smaller (diameters of 300 nm and 600nm) than the wavelength of the trapping beam (1064 nm Nd:YAG, or 800 nm in water). [17] Particle separations were multiples of the applied wavelength in the 300 nm case, but deviated significantly in the 600 nm case. Calculations that treat the particles as point dipoles predict separations that are integer multiples of the applied wavelength (i.e. in the Rayleigh limit). [18, 19] However, when the particle

3

size approaches the applied wavelength, calculations of the scattered field and resultant particle separations must take into account the curvature of the particle surface (via Mie-Debye theory).

The 2-beam transverse trapping geometry has been studied theoretically for multiple particles by Ng *et. al.*[20] Using Mie theory to compute the multiple scattering between particles, Ng and co-workers predict 2-dimensional photonic clusters with stable or quasistable particle positions depending on levels of damping.

1.2.2. Longitudinal optical binding

Optical binding in counterpropagating Gaussian beams was first reported by Tatarkova et. al.[21] for silica microspheres of size $ka > 3.9$, where the wavenumber, $k = \dfrac{2\pi}{\lambda}$ and a is the particle radius. The microspheres were trapped on-axis, with smaller particle spacings as more particles were added to the array. Separately, Singer et. al.[22] investigated the size dependency of equilibrium spacing with the following observations:

- Microspheres with diameters less than half the laser wavelength were trapped with separations of approximately $\lambda/2$. The mechanism for optical binding is via the interference between the incident and backscattered fields.

- Microspheres with diameters on the order of the laser wavelength were arrayed with separations that increased with particle size. The mechanism for optical binding is due to forward-scattered light refocusing and the subsequent balancing of radiation pressure.

- Microspheres with diameters greater than twice the laser wavelength formed closed chains, in which the particles were in contact. The radiation pressure exerts a greater inward force on the particles than the repulsive force due to the refocusing of light, and so leads to the collapse of optical binding.

Optical binding that is predominantly the result of particle interactions with forward-scattered light has been modelled by assuming paraxial propagation of the applied and scattered fields.[23] This model of optical binding is limited to on-axis optical binding where particle diameters are greater than the incident wavelength, but successfully agrees with the sphere separations previously reported by Tatarkova *et*. *al*.[21], and observations of bistability and hysteresis in long-range optical binding.[24, 25]

Optical binding of Mie particles have been modelled using a coupled dipole method (CDM),[26] in which the microspheres are subdivided into point dipoles (or Rayleigh particles). The force acting on each particle then becomes a sum of the forces acting on its constituent dipoles due to the incident and scattered fields. CDM agrees qualitatively with the data previously presented by Metzger *et*. *al*.,[24, 25] namely that the equilibrium positions in a bistable 2-sphere array are sensitive to 1% changes in refractive index contrast. This method accounts for short range modulation in the optical binding forces which result from interference between the incident and backscattered fields, as well as the longer range forward-scattered optical binding. This approach is valid for particles of arbitrary shape and size, but is largely limited to smaller particles by computational memory requirements.

A more exact and general approach to calculating optical binding forces was presented by Gordon et. al.[27, 28], which uses a generalized multipole technique (GMT) to expand the scattered electric fields inside and outside the particle-water interface as a series of Bessel or Hankel vectorial spherical wavefunctions, respectively. Once the electromagnetic fields were calculated, Maxwell's stress tensor (MST) was evaluated to obtain the optically induced force on each particle. This approach is applicable to microspheres of all sizes and even for high refractive index contrast between the particles and host medium.

The same authors show experimentally that, for large PS microspheres ($ka =$ 4.2), the average inter-particle spacing decreases nonlinearly as the total number of trapped particles increases, and that particles near the centre of an array are more closely spaced than particles near the ends. The difference between the outer particle spacing, d_{out}, and the inner spacing, d_{inn}, increases with particle numbers (Figure 1.2). Taylor and Love[29] use a similar GMT-MST method, in combination with a more intuitive ansatz model, to illustrate how forward scattering of light explains the observed behaviour of an optically bound chain.

Consider a particle chain bound by counterpropagating beams: the force pushing inwards on particles closer to the centre is enhanced by the focusing of light due to neighbouring particles. Assuming there are some losses along the chain, then the force pushing outwards on the end particles will also increase, but by a smaller amount. Additional particles will increase the forces pushing the inner particles inwards, which increases the transmission efficiency that then pushes the outer particles outwards. As even more particles are added to an array, the array is sufficiently compressed so that the particles experience the attractive near-field gradient forces from neighbouring particles. In such cases, no repulsive forces support a well-spaced array, so the chain collapses.
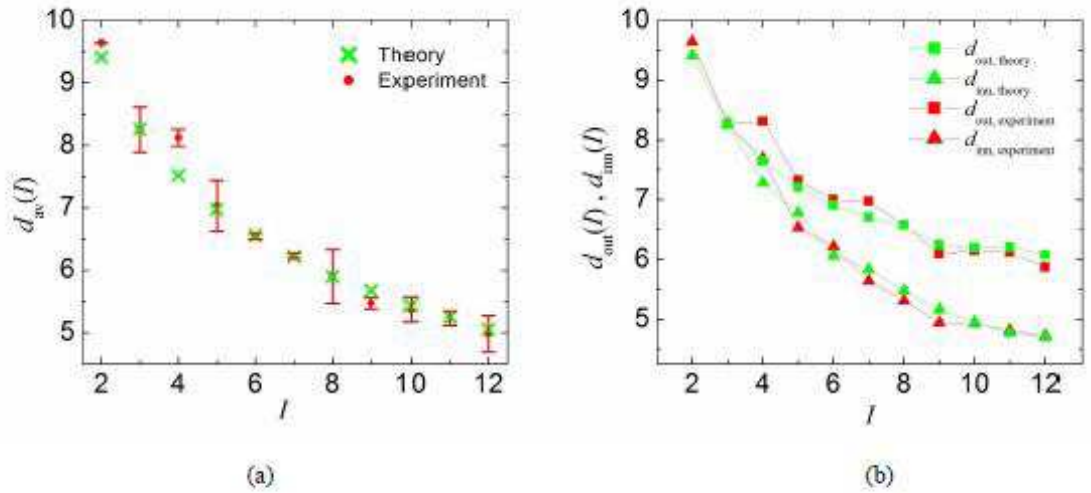
Figure 1.2: Inhomogenous properties of inter-particle spacing. (a) Averaged inter-particle spacing d_{av} as a function of the number of particles I. (b) The inner most inter-particle spacing d_{inn} and the outer most interparticle spacing d_{out}, as a function of I.[28]

Taylor and Love subsequently report spontaneous off-axis trapping and oscillation of optically bound microparticle chains in trapped counterpropagating Gaussian beams.[30] GMT-MST simulations show that small perturbations (e.g. due to Brownian motion) are amplified by a "plume" of off axis scattered light, which then pulls neighbouring particles further off axis

(Figure 1.3). This phenomenon is not expected for an array of relatively few trapped microparticles, as the particles will be too far from each other to be pushed off-axis by the scattered "plume". If particle size D, refractive index contrast Δn, or total particle number N are sufficiently high, small perturbations can lead to stable off axis trapping. If those same parameters are higher still, the array stabilizes into a closed orbit which can be asymmetric about the z-axis, or a figure-of-eight about the trap centre. In contrast, previous observations of array oscillations were attributed to an intentional beam misalignment and amplification of motion due to hydrodynamic coupling between closely spaced particles.[27, 28]
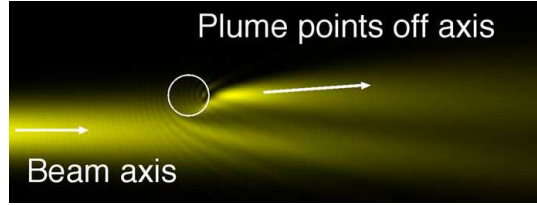
Figure 1.3: Field intensity around a single off-axis particle, showing the "plume" of light focused by the particle in this case a 3 μm diameter silica sphere. Due to the diverging nature of the beam, this is angled slightly off-axis, and so a second particle will be drawn even further away from the axis through the gradient force.[30]

While a large proportion of optical binding studies have focused on large microparticles in non-interfering incident fields, Hang *et. al.* have studied the behaviour of small (ka =1.1) polystyrene spheres trapped in interference fringes, using a multiple scattering expansion of the scattered fields similar to GMT.[31] They consider a system of two pairs of equal-intensity counterpropagating electromagnetic waves illuminating a particle chain with varying incident angle β (Figure 1.4). The incident fields interfere to form fringes that act as optical traps. The optical trapping length scale is $\lambda_{OT} = \lambda/(2 \cos \beta)$. Optical binding in this geometry occurs when the externally induced dipole on one particle is in

phase with the backscattered field from an adjacent particle. Hence, the optical binding length scale is $\lambda_{OB} = \lambda/(1 \pm \cos \beta)$. Transverse optical binding corresponds to incident angle $\beta = \pi/2$, when $\lambda_{OT} = \lambda_{OB} = \lambda/2$. Longitudinal optical binding corresponds to $\beta = 0$, when $\lambda_{OT} = \infty$, and $\lambda_{OB} = \lambda$. The authors also found other values of β for which λ_{OT} and λ_{OB} are commensurate, at which optical binding interactions act to stabilise a long chain of spheres.
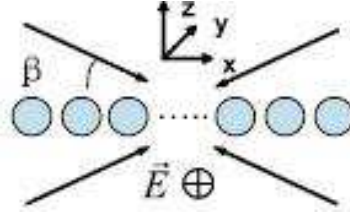
Figure 1.4: Four beam counterpropagating geometry used by Hang *et. al.* to study the effect of varying λ_{OT} relative to λ_{OB}.[31]

When λ_{OT} and λ_{OB} are incommensurate, Hang *et. al.* predict spatial modulation in the particle chains which is a multiple of λ_{OT} (Figure 1.5). Particle chains of length close to a multiple of the modulation length scale are found to be stable, while other long particle chains are unstable. The modulation amplitude increases with sphere size, but the repeat distance depends solely on the incident angle β.
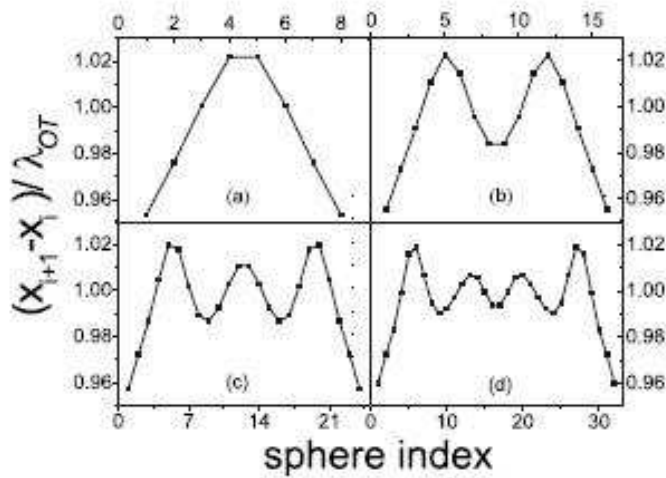
Figure 1.5: Particle separations normalized by λ_{OT} for (a) particles numbers $N=9$; (b) $N=17$; (c) $N=25$; (d) $N=33$; at $\beta=0.2\pi$ and $ka=1.1$.[31]

1.2.3. Optical binding in evanescent fields

In 1992, Kawata and Sugiura reported that the evanescent field generated by total internal reflection (TIR) of a laser beam was able to impart momentum to microspheres placed in it.[32] The particles moved along the glass-water TIR interface in the direction of evanescent wave propagation. The penetration depth of the evanescent field falls as the incident angle θ_i increases (Equation 2.11), and so the imparted velocity also decreases. The optically induced forces on a single particle in an evanescent wave have been described by various groups using ray optics,[33] Mie-Debye theory,[34] and CDM.[35, 36] They invariably show that dielectric particles with refractive index greater than the host medium will be drawn towards the TIR interface by the gradient force (in contrast to initial reports of repulsion at the interface by Kawata and Sugiura). This attraction can be rationalised as follows: the local surface force acts in an outward direction (i.e. from the sphere to the surrounding medium). Since the evanescent field decays exponentially away from the TIR interface, the net force on the particle is towards the TIR interface. The same theoretical treatments also predict stronger particle interactions when the incident beam is *p*-polarised (i.e. the electric field is in the plane of incidence), than when it is *s*-polarised (i.e. the electric field is in the TIR plane). Reece *et. al.* confirm the polarisation and incident angle dependence by measuring the particle speed when placed in an evanescent wave (Figure 1.6).[37]
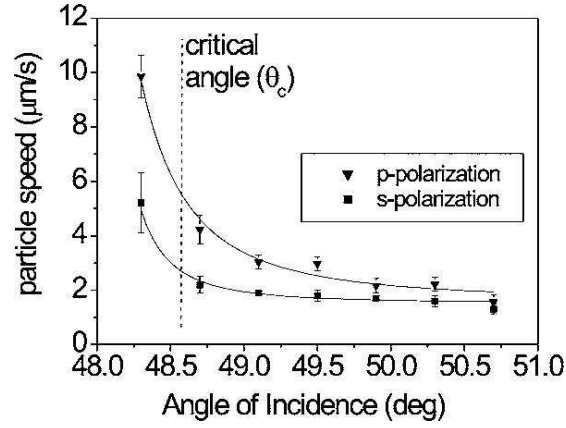
Figure 1.6: Velocity of 5 μm polymer colloids at a BK7 glass-water interface, resulting from optical interactions with evanescent waves generated by *p*-(solid triangles) and *s*-polarized (solid squares_) light incident at different incident angles around the critical angle. Solid lines are an aid to the eye. The dotted line represents the experimentally determined critical angle.[37]

The use of counterpropagating evanescent fields is then able to trap microparticles near the TIR interface, since translational forces on microparticles along the interface will be balanced out. Counterpropagating evanescent fields have been used to demonstrate optical transport,[38] and optical sorting[39] of microparticles.

Two-dimensional array formation of submicron particles in counterpropagating evanescent waves was first studied by Mellor and Bain,[40-42] using the experimental setup pictured in Figure 1.7. At an incident angle θ_i of 68° (just above the critical angle θ_c for silica), the incident beam of wavelength 1064 nm produced evanescent fields with interference fringe spacing $D \sim 400$ nm, and penetration depth $d_p \sim 800$ nm.
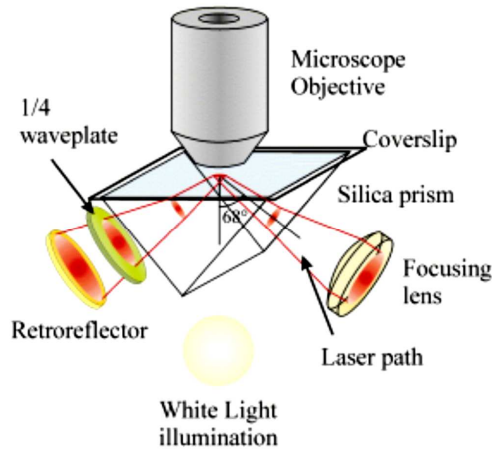
Figure 1.7: Schematic illustration of the evanescent wave optical binding experiment. A dilute suspension of monodisperse PS particles in water is introduced between the prism and a coverslip. The trapped particles are observed in white light with a 100x oil-immersion objective and recorded on a video camera.[40-42]

They report size and polarisation dependent behaviour for arrays formed in counterpropagating evanescent waves, which are briefly summarised below:

- For particles of diameter $\geq \lambda/n_{H2O}$, line arrays were formed parallel to the propagation of the evanescent fields. Trapped arrays are able to move transversely (i.e. in fringe direction), without losing structural integrity.

- For particles of diameter $< \lambda/n_{H2O}$, particles form chessboard or hexagonal two-dimensional arrays, where particle spacings are generally commensurate with the interference fringes (Figure 1.8). The unit cell symmetry was found to be polarisation dependent, and the transition from one array to the other is reversible. Occasionally, spontaneous rearrangement to an incommensurate hexagonal structure was observed.

- For particles of diameters that are slightly larger than the fringe spacing (i.e. 460 and 520 nm) trapped in the evanescent fields from *p*-polarised light, hexagonal arrays are observed where every second or third column is unoccupied (or broken hexagonal).

- For orthogonally polarised incident beams, the evanescent fields are non-

interfering but a hexagonal array is still observed. The constituent particles are not in contact, and particle spacings are not dictated by the presence of interference fringes.

(a)   (b)
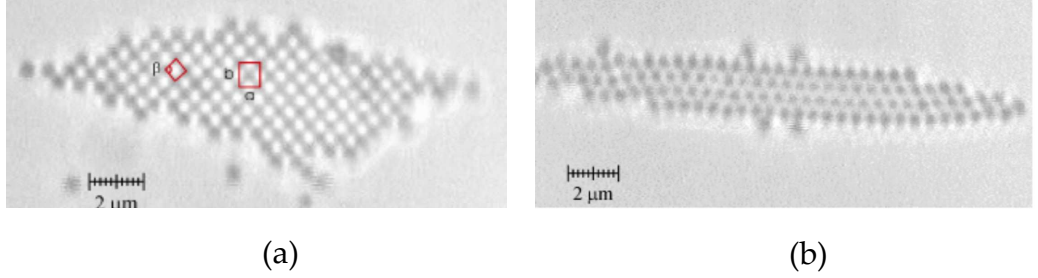
Figure 1.8: In s-polarised light: (a) array of 460-nm diameter spheres. A centred rectangular unit cell is shown, with lattice parameters *a* and *b* perpendicular and parallel to the fringes, respectively. (b) Hexagonal array formed by 520 nm particles in s-polarized light with 5 μM NaCl.[40-42]

Figure 1.9 shows the force on a single particle in a set of interference fringes as a function of particle size parameter ka, calculated by Taylor $et.$ $al.$[43] for the experimental setup used by Mellor $et.$ $al.$[40-42]: k is the wavenumber in the host medium, and a is the particle radius. A positive force indicates that the particle is attracted to a bright fringe, while a negative force means that the particle is attracted to dark fringes. The particle-fringe interaction has been calculated by other groups[44-46] with similar results giving the following rule-of-thumb: a single particle will move to cover the maximum number of antinodes (bright fringes) in an interference field. The trapping of particles on/between interference fringes is then able to explain the commensurate arrays observed by Mellor $et.$ $al.$, but does not explain the spontaneous formation of incommensurate arrays.
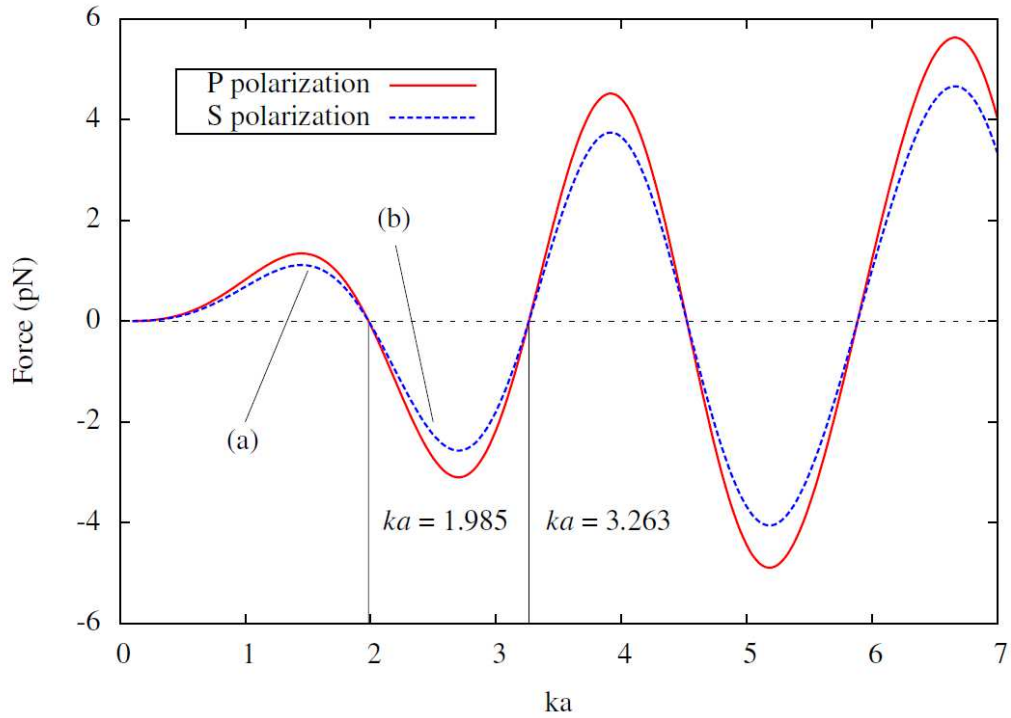
Figure 1.9: Force acting on a single particle placed halfway between a bright and dark fringe, as a function of size parameter ka as calculated by Taylor $et.$ $al.$[43]

Reece *et. al.* have enhanced the evanescent field intensities and obtained larger particle arrays by surface plasmon polariton (SPP) resonance (Figure 1.10).[47] The enhanced evanescent wave generated by SPP was shown to organise linear arrays of 5μm silica microparticles at much lower powers (by a factor of 3) than that for standard evanescent wave optical traps.

P=20mW   P=40mW

P=50mW   P=100mW
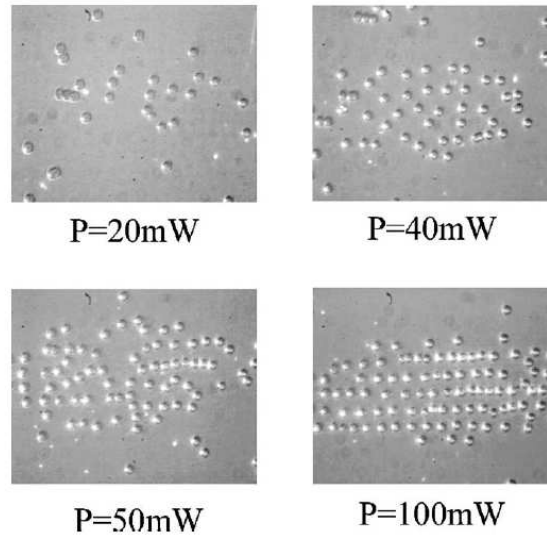
Figure 1.10: Successive frames showing the behaviour of 5μm silica microparticles as a function of increasing power. The formation of linear arrays can be seen at P= 100 mW, due to enhanced optical interaction from surface plasmon polariton excitation.[47]

Optical binding in evanescent waves have been studied using a mode locked cavity to create resonance of the counterpropagating beams.[48, 49] In these experiments, 1.0 μm silica spheres formed chains up to 150 μm in length (Figure 1.11). Such chains were transversely mobile (as reported by Mellor *et. al.*), and since the cavity mode lock rules out beam misalignment, the mechanism of this optically driven motion remains unexplained. As the number of trapped particles is increased, the spatially extended chain becomes unstable and is observed to collapse, or show angular and translational off-axis motion.
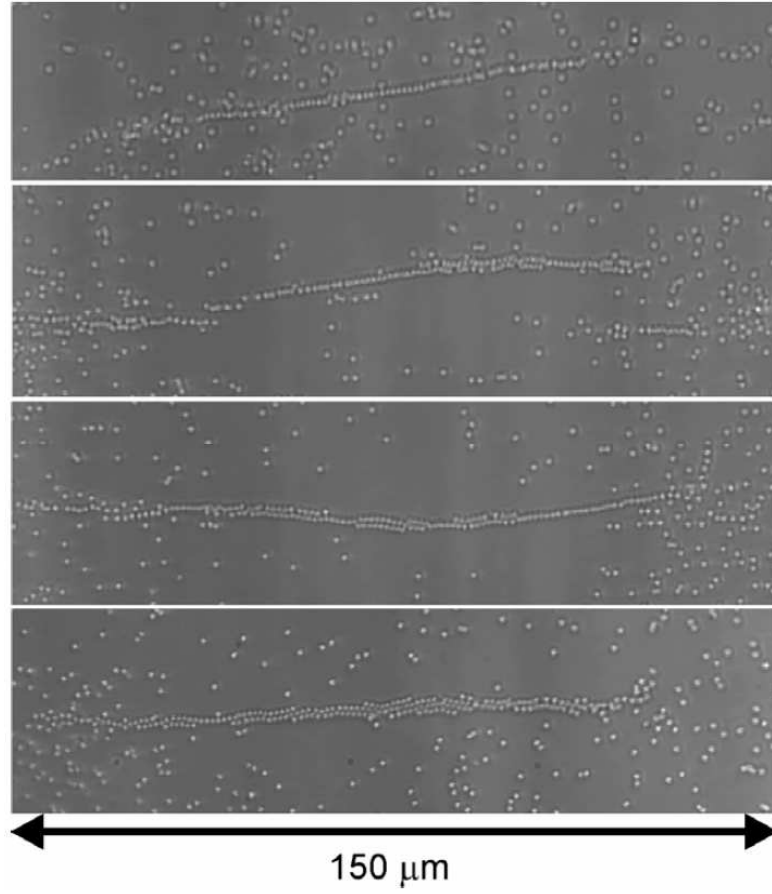
Figure 1.11: Chain-like structures of 1 μm silica formed for different input powers (corresponding peak intensity on the surface is given in brackets): (i) 100 mW (0.34 mW μm^{-2}); (ii) 175 mW (0.68 mW μm^{-2}); (iii) 219 mW (0.94 mW μm^{-2}); (iv) 266 mW (1.02 mW μm^{-2}).[49]

1.3. Thesis Outline

The aim of this thesis is to explore the behaviour of particle arrays within evanescent optical traps. The common theme throughout is the balance between optical trapping and optical binding forces, which gives rise to a rich diversity of array behaviours.

Chapter 2 begins with basic equations that are relevant to optical trapping in evanescent fields. This chapter then sets out my experimental method using an existing optical trapping setup (λ= 1064 nm Nd:YAG), and a newly developed optical trapping setup (λ= 840 -890 nm Ti:sapphire).

Chapter 3 presents results obtained on the fixed wavelength optical trapping setup (λ= 1064 nm Nd:YAG), for a number of different microparticle materials such as polystyrene (PS), silica, sterically stabilised poly(ethylene glycol) methacrylate (PEGMA-P2VP), and gold. Simulations to support our experimental observations are presented here. These simulations are the work of our collaborators (whose contribution is made clear in the text).

Chapter 4 presents results from experiments using a tunable laser source (λ= 840 -890 nm Ti:sapphire) where the two counterpropagating beams are mutually coherent. Optical trapping of PS microspheres of different sizes while varying incident wavelength allowed near-continuous tuning of ka. This enabled experimental study of array formation as the node/ antinode affinity of individual particles approached zero (Figure 1.9).

Chapter 5 presents results from experiments using a tunable laser source (λ= 840 -890 nm Ti:sapphire) where the two counterpropagating beams are mutually incoherent. Use of a beam delay line enabled optical trapping experiments where the two beams were of the same polarisation but did not not form stable interference fringes. Without the periodic potential provided by the

interference fringes, stable arrays will mainly be due to gradient forces and optical binding.

Chapter 6 highlights two interesting phenomena that occurred during optical trapping experiments. While neither phenomenon is particularly helpful for elucidating array forming mechanisms, they serve as a reminder of the unpredictability of optical binding interactions.

Finally, Chapter 7 summarises some of the common themes drawn from the results presented in the preceding chapters.

References

1.   K. Dholakia and P. Zemanek, *Rev Mod Phys*, 2010, **82**.

2.   E. F. Nichols and G. F. Hull, *Physical Review* 1901, **13**, 301.

3.   A. Ashkin, *Physical Review Letters*, 1970, **24**, 156-&.

4.   A. Ashkin, J. M. Dziedzic, J. E. Bjorkholm and S. Chu, *Optics Letters*, 1986, **11**, 288-290.

5.   J. E. Molloy and M. J. Padgett, *Contemp Phys*, 2002, **43**, 241-258.

6.   A. Ashkin, J. M. Dziedzic and T. Yamane, *Nature*, 1987, **330**, 769-771.

7.   C. Bustamante, Z. Bryant and S. B. Smith, *Nature*, 2003, **421**, 423-427.

8.   E. Eriksson, J. Enger, B. Nordlander, N. Erjavec, K. Ramser, M. Goksor, S. Hohmann, T. Nystrom and D. Hanstorp, *Lab on a Chip*, 2007, **7**, 71-76.

9.   S. Cran-McGreehin, T. F. Krauss and K. Dholakia, *Lab on a Chip*, 2006, **6**, 1122-1124.

10.   S. J. Cran-McGreehin, K. Dholakia and T. F. Krauss, *Optics Express*, 2006, **14**, 7723-7729.

11.   M. Goksor, J. Enger and D. Hanstorp, *Applied Optics*, 2004, **43**, 4831-4837.

12.   E. R. Dufresne, G. C. Spalding, M. T. Dearing, S. A. Sheets and D. G. Grier, *Review of Scientific Instruments*, 2001, **72**, 1810-1816.

13.   P. C. Mogensen and J. Gluckstad, *Optics Communications*, 2000, **175**, 75-81.

14.   I. R. Perch-Nielsen, P. J. Rodrigo and J. Gluckstad, *Optics Express*, 2005, **13**, 2852-2857.

15.   M. M. Burns, J. M. Fournier and J. A. Golovchenko, *Physical Review Letters*, 1989, **63**, 1233-1236.

16.   M. M. Burns, J. M. Fournier and J. A. Golovchenko, *Science*, 1990, **249**, 749-754.

17.   S. K. Mohanty, J. T. Andrews and P. K. Gupta, *Optics Express*, 2004, **12**, 2746-2753.

18.   F. Depasse and J. M. Vigoureux, *Journal of Physics D-Applied Physics*, 1994, **27**, 914-919.

19.   L. E. Malley, D. A. Pommet and M. A. Fiddy, *Journal of the Optical Society*

of America B-Optical Physics, 1998, **15**, 1590-1595.

20.   J. Ng, Z. F. Lin, C. T. Chan and P. Sheng, *Physical Review B*, 2005, **72**, 11.

21.   S. A. Tatarkova, A. E. Carruthers and K. Dholakia, *Physical Review Letters*, 2002, **89**, 4.

22.   W. Singer, M. Frick, S. Bernet and M. Ritsch-Marte, *Journal of the Optical Society of America B-Optical Physics*, 2003, **20**, 1568-1574.

23.   D. McGloin, A. E. Carruthers, K. Dholakia and E. M. Wright, *Physical Review E*, 2004, **69**, 6.

24.   N. K. Metzger, E. M. Wright and K. Dholakia, *New Journal of Physics*, 2006, **8**, 14.

25.   N. K. Metzger, K. Dholakia and E. M. Wright, *Physical Review Letters*, 2006, **96**, 4.

26.   V. Karasek, K. Dholakia and P. Zemanek, *Applied Physics B-Lasers and Optics*, 2006, **84**, 149-156.

27.   R. Gordon, M. Kawano, J. T. Blakely and D. Sinton, *Physical Review B*, 2008, **77**, 24125.

28.   M. Kawano, J. T. Blakely, R. Gordon and D. Sinton, *Optics Express*, 2008, **16**, 9306-9317.

29.   J. M. Taylor and G. D. Love, *Optics Express*, 2009, **17**, 15381-15389.

30.   J. M. Taylor and G. D. Love, *Phys Rev A*, 2009, **80**, -.

31.   Z. H. Hang, J. Ng and C. T. Chan, *Phys Rev A*, 2008, **77**, -.

32.   S. Kawata and T. Sugiura, *Optics Letters*, 1992, **17**, 772-774.

33.   R. J. Oetama and J. Y. Walz, *Colloid Surface A*, 2002, **211**, 179-195.

34.   E. Almaas and I. Brevik, *Journal of the Optical Society of America B-Optical Physics*, 1995, **12**, 2429-2438.

35.   P. C. Chaumet and M. Nieto-Vesperinas, *Physical Review B*, 2000, **61**, 14119-14127.

36.   M. Nieto-Vesperinas, P. C. Chaumet and A. Rahmani, *Philosophical Transactions of the Royal Society of London Series a-Mathematical Physical and Engineering Sciences*, 2004, **362**, 719-737.

37. P. J. Reece, V. Garces-Chavez and K. Dholakia, *Applied Physics Letters*, 2006, **88**, 3.

38. V. Garces-Chavez, K. Dholakia and G. C. Spalding, *Applied Physics Letters*, 2005, **86**, 3.

39. T. Cizmar, M. Siler, M. Sery, P. Zemanek, V. Garces-Chavez and K. Dholakia, *Physical Review B*, 2006, **74**, 6.

40. C. D. Mellor and C. D. Bain, *Chemphyschem*, 2006, **7**, 329-332.

41. C. D. Mellor, C. D. Bain and J. Lekner, in *Optical Trapping and Optical Micromanipulation II*, eds. K. Dholakia and G. C. Spalding, Proc. SPIE, 2005, vol. 6930, p. 352.

42. C. D. Mellor, T. A. Fennerty and C. D. Bain, *Optics Express*, 2006, **14**, 10079-10088.

43. J. M. Taylor, L. Y. Wong, C. D. Bain and G. D. Love, *Optics Express*, 2008, **16**, 6921-6929.

44. J. Lekner, *Journal of Optics a-Pure and Applied Optics*, 2005, **7**, 238-248.

45. P. Zemanek, A. Jonas and M. Liska, *Journal of the Optical Society of America a-Optics Image Science and Vision*, 2002, **19**, 1025-1034.

46. J. Ng and C. T. Chan.

47. V. Garces-Chavez, R. Quidant, P. J. Reece, G. Badenes, L. Torner and K. Dholakia, *Physical Review B*, 2006, **73**, 5.

48. M. D. Summers, R. D. Dear, G. A. D. Ritchie and J. M. Taylor, in *Optical Trapping and Optical Micromanipulation VII*, eds. K. Dholakia and G. C. Spalding, Proc. SPIE, 2010, p. 776213.

49. N. J. van Leeuwen, L. J. Moore, W. D. Partridge, R. Peverall, G. A. D. Ritchie and M. D. Summers, *J Optics-Uk*, 2011, **13**.

2. Experimental Method

2.1. Equations and parameters

2.1.1. The evanescent field

The generation of evanescent fields by total internal reflection (TIR) is described[1,2]. For a plane wave incident at a planar interface at an incident angle θ_i, part of the wave is reflected and part is transmitted through the interface (*Figure 2.1*).
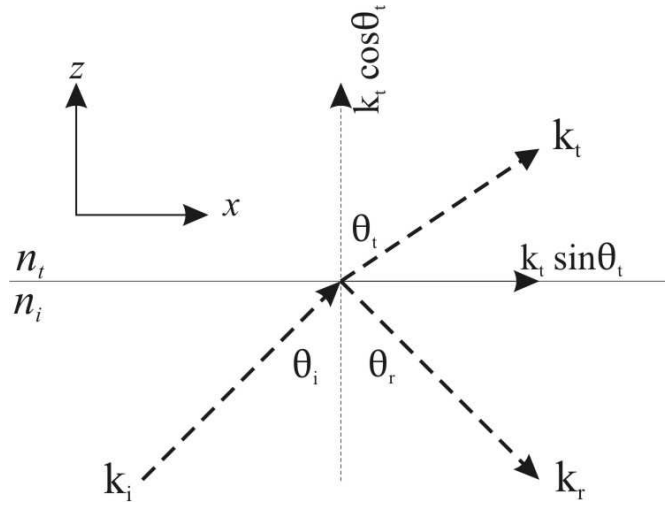
Figure 2.1: Propagation vectors for internal reflection. The *x-y* plane is the interface, and the *x-z* plane is the plane of incidence.

The wavefunction of the transmitted electric field, $\mathbf{E}_t$ is

$$\mathbf{E}_t = \mathbf{E}_{0t} exp^{i(\mathbf{k_t} \cdot \mathbf{r} - \omega t)} \tag{2.1}$$

where $\mathbf{E}_{0t}$ is the electric field at the interface, and ω is the angular frequency of the transmitted light, t is time, $\mathbf{k}_t$ is the wavevector of the transmitted wave and $\mathbf{r}$ is the position vector.

$$\mathbf{k_t} \cdot \mathbf{r} = k_{tx} x + k_{tz} z \tag{2.2}$$

$$\mathbf{k_t} \cdot \mathbf{r} = k_t x \sin \theta_t + k_t z \cos \theta_t \tag{2.3}$$

there being no *y*-component of $\mathbf{k}$. Equation (2.1) can be rewritten as

$$\mathbf{E}_t = \mathbf{E}_{0t} exp(-i[k_t x \sin \theta_t + k_t z \cos \theta_t - \omega t]) \tag{2.4}$$

The angle of propagation of the transmitted beam, θ_t is given by Snell's Law

$$\sin\theta_t = \frac{\sin\theta_i}{n_{ti}} \tag{2.5}$$

where $n_{ti} = {}^{n_t}\!\big/\!_{n_i}$. Equation (2.5) can be used to show that

$$k_t\cos\theta_t = \pm k_t\left(1 - \frac{\sin^2\theta_i}{n_{ti}^2}\right)^{1/2} \tag{2.6}$$

When the incident medium is the more optically dense of the two ($n_i > n_t$), there exists a critical angle, θ_c, above which all incoming energy is reflected back into the incident medium. This phenomenon is called total internal reflection (TIR). If $\theta_i \geq \theta_c$, Equation (2.6) gives

$$k_{tz} = \pm i k_t\left(\frac{\sin^2\theta_i}{n_{ti}^2} - 1\right)^{1/2} \equiv \pm i\beta \tag{2.7}$$

$$k_{tx} = \frac{k_t}{n_{ti}}\sin\theta_i \tag{2.8}$$

Substituting Equations (2.7) and (2.8) into Equation (2.4) gives

$$\mathbf{E}_t = \mathbf{E}_{0t}exp(\mp\beta z\,)exp\left[i\left(k_t x\sin\theta_i\Big/n_{ti} - \omega t\right)\right] \tag{2.9}$$

The positive exponential suggests an increasing field at greater distance from the interface, and so is physically untenable. Thus, the evanescent wave must have amplitude that decays exponentially from the interface into the less dense medium. Energy transport occurs parallel to the interface, but not in the z-direction.

Equation (2.9) can be manipulated to find the penetration depth, d_p, which is defined as the distance from the interface that the electric field falls to $1/e$ of the amplitude at the interface.

$$\mathbf{E}_t = \mathbf{E}_{0t}exp(-\beta d_p\,) = \mathbf{E}_{0t}exp(-1)$$

$$\beta d_p = 1 \tag{2.10}$$

$$d_p = \frac{1}{\beta} = \frac{\lambda_0}{2\pi n_t \left[\left(\dfrac{\sin^2 \theta_i}{n_{ti}^{~2}} \right) - 1 \right]^{\frac{1}{2}}} \tag{2.11}$$

where λ_0 is the wavelength in vacuum.
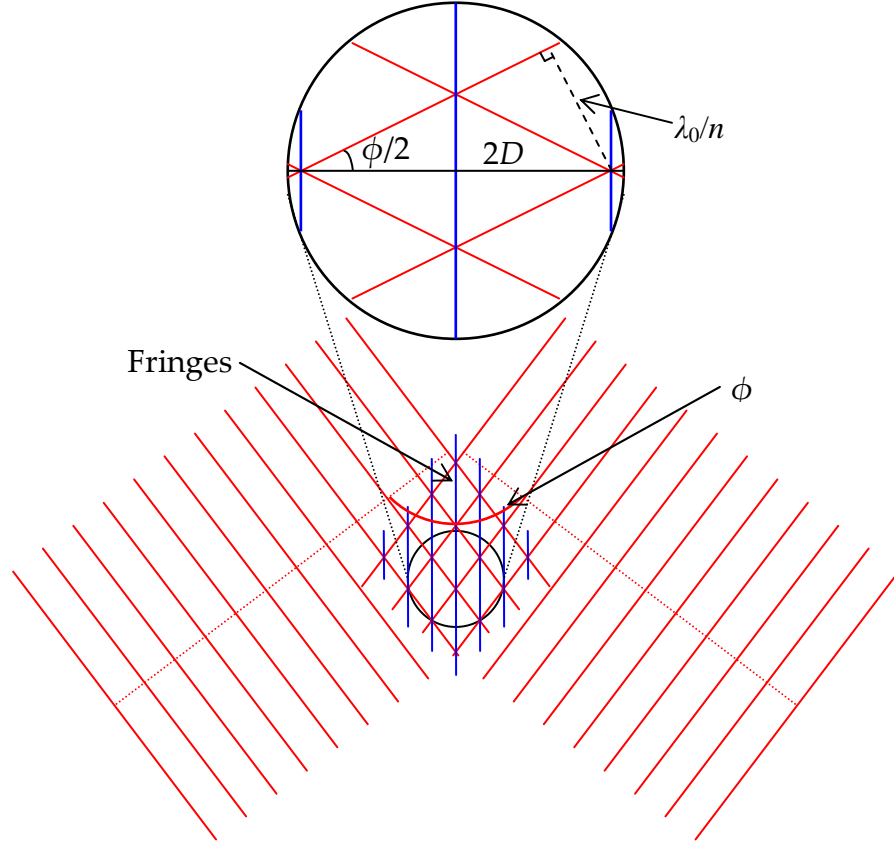
Figure 2.2: Side view of two overlapping plane waves (wavefronts shown as red solid lines) with an angle between the beams, ϕ, thus creating an interference pattern (in blue). The inset shows the right angled triangle used to find the fringe spacing D.

The interference fringe spacing D formed by two crossing plane waves can be found using the trigonometric identity from the right angled triangle shown in Figure 2.2 to be as follows:

$$\sin(\frac{\phi}{2}) = \frac{\lambda_0}{2Dn} \tag{2.12}$$

$$D = \frac{\lambda_0}{2n\sin(\frac{\phi}{2})} \tag{2.13}$$

where λ_0 is the wavelength of light in a vacuum, n is the refractive index of the host medium, and ϕ is the angle between the beams. When the plane waves are counterpropagating, the fringe spacing is simply $\lambda_0/2n$.

The fringe spacing D for an evanescent interference pattern depends on the angle of incidence θ_i.

$$D = \frac{\lambda_0}{2n_i \sin\theta_i} \tag{2.14}$$

At the critical angle ($\theta_i = \theta_c$) the fringe spacing equals $\lambda_0/2n$, with $n = n_{H_2O}$. For $\theta_i > \theta_c$, the fringe spacing is reduced from this value by a factor $\sin\theta_c/\sin\theta_i$. Finally, as θ_i approaches 90°, D tends to $\lambda_0/2n_{glass}$.

2.1.2. Generalized Lorentz-Mie Theory for optical binding

The theoretical treatment of optical binding using Generalized Lorentz-Mie Theory (GLMT) is especially appropriate for the particles sizes used in my experimental work. The following section summarises the application of GLMT to optical binding as described in Taylor's work.[3]

We begin by showing that an electromagnetic field $\mathbf{e}(\mathbf{r})$ can be decomposed into a complete orthonormal basis of eigenfunctions $\mathbf{e}_i(\mathbf{r})$, each with amplitude a_i:

$$\mathbf{e}(\mathbf{r}) = \sum_i a_i \mathbf{e}_i(\mathbf{r}) \qquad (2.15)$$

Next, a particle exposed to a given incident field will produce a scattered field which can again be represented in that same basis, with amplitudes s_i:

$$\mathbf{s} = \mathbf{T} \cdot \mathbf{a} \qquad (2.16)$$

where $\mathbf{T}$ is a matrix describing the scattering behaviour of the particle. In general $\mathbf{T}$ will depend on the shape and physical properties of the particle, and for dielectric particles can be determined by considering the boundary conditions on the electromagnetic field at the dielectric interface.

GLMT is ideal for studying spherical particles as it represents incident and scattered fields in terms of vector spherical wavefunctions (VSWFs) comprised of spherical Bessel and Hankel functions, respectively. For further details of the beam expansion as represented using VSWFs, the interested reader is directed to other texts.[3-5] Each individual VSWF is a solution to Maxwell's equations. Since the VSWFs form a complete orthogonal set, any coherent field can be represented as a sum of normalized VSWFs. This method can be applied to particles of any size, from the Rayleigh limit up to the ray optics regime, but is most efficient for particles in the Mie regime where particle sizes are comparable to the wavelength of light.

GLMT generalises easily to multiple particles due to the linearity of the electromagnetic field equations. The scattering behaviour of each individual particle is calculated from the total field incident on the particle, which is the sum of the external field and all the scattered waves from other particles. Thus the total field $\mathbf{a}^{(k)}$ incident on particle k (as in Equation (2.16)) is:

$$\mathbf{a}^{(k)} = \mathbf{a}_{(ext)}^{(k)} + \sum_{j \neq k} \mathbf{s}'^{(j)} \tag{2.17}$$

where $\mathbf{s}'^{(j)}$ are the field coefficients for the field scattered by sphere j, in the basis of VSWFs centred on particle k. Equation (2.17) applies simultaneously to every particle k in the system, written in their individual bases, and the result is a large system of coupled equations which can be solved to determine the resultant field.

The effect of multiple scattering, where the scattered light from one particle is re-scattered by another particle, are only a small perturbation to the first-order solution. Where the effect of multiple scattering is significant, an iterative solution can be obtained, as follows:

Firstly, Equation (2.17) can be expressed as:

$$\underline{\mathbf{a}} = \underline{\mathbf{a}}_{ext} + \underline{\mathbf{F}}\underline{\mathbf{s}} \tag{2.18}$$

where $\mathbf{F}_{ij}$ is the translation matrix which transforms a scattered field in the basis of sphere i into an incident field in the basis of sphere j, as given by:

$$\mathbf{s}^{(j)} = \mathbf{F} \cdot \mathbf{s}^{(i)} \tag{2.19}$$

Using the notation of Equation (2.18), the scattered field $\underline{\mathbf{s}}_0$ is the field obtained by treating every sphere as a scatterer in isolation.

$$\underline{\mathbf{s}}_{(0)} = \underline{\mathbf{T}} \cdot \underline{\mathbf{a}}_{ext} \tag{2.20}$$

The next incident field due to the zero-order scattered field is then:

$$\underline{\mathbf{a}}_{(1)} = \underline{\mathbf{a}}_{ext} + \underline{\mathbf{F}} \cdot \underline{\mathbf{s}}_{(0)} \tag{2.21}$$

The first-order scattered field is then:

$$\underline{\mathbf{s}}_{(1)} = \underline{\mathbf{T}} \cdot \underline{\mathbf{a}}_{(1)} \tag{2.22}$$

The second-order net incident fields is then:

$$\underline{\mathbf{a}}_{(2)} = \underline{\mathbf{a}}_{ext} + \underline{\mathbf{F}} \cdot \underline{\mathbf{s}}_{(1)} \tag{2.23}$$

and so on until the field converges.

Multiple scattering can be represented using the infinite sum:

$$\underline{\mathbf{s}} = \left[\underline{\mathbf{T}} + \left(\underline{\mathbf{T}} \cdot \underline{\mathbf{F}} \cdot \underline{\mathbf{T}} \right) + \left(\underline{\mathbf{T}} \cdot \underline{\mathbf{F}} \cdot \underline{\mathbf{T}} \cdot \underline{\mathbf{F}} \cdot \underline{\mathbf{T}} \right) \dots \right] \cdot \underline{\mathbf{a}}_{ext} \tag{2.24}$$

Taylor's calculations suggest that a solution to Equation (2.18) which is accurate to one part in 10^{-5} can be obtained within about 10 to 20 iterations, even for particles whose centres are only 3 radii apart.[3]

2.2. Optics setup

2.2.1. Optical trapping with Nd:YAG

A schematic diagram of the setup is shown in Figure 2.3(a). An optical trap was created at the glass-water interface by overlap of the forward and retroreflected λ=1064 nm beams.
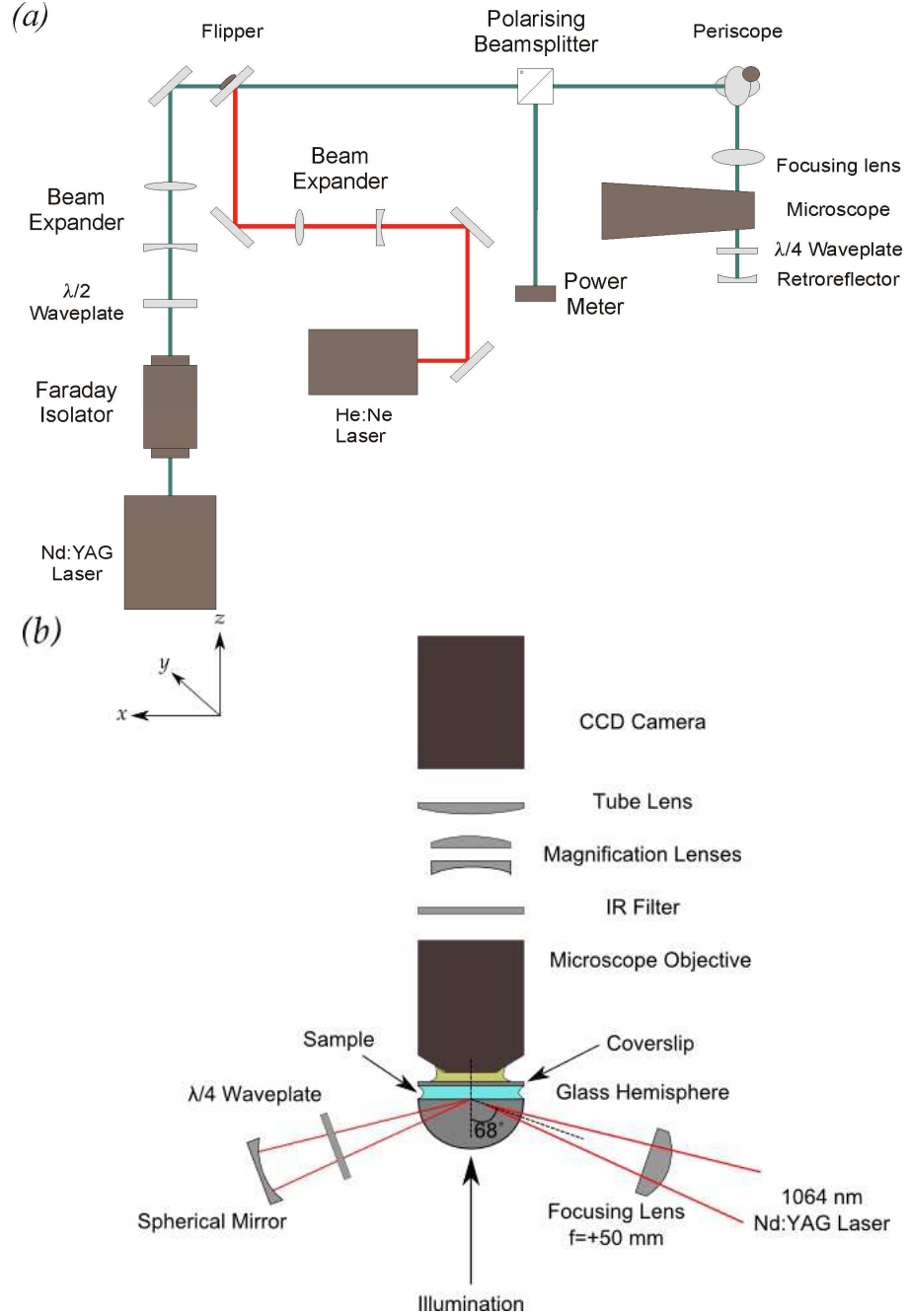

Figure 2.3: Schematic showing (a) the optical bench layout, and (b) the experimental setup around the microscope for optical trapping in evanescent waves generated by TIR with a Nd:YAG λ=1064 nm laser.

For trapping, a continuous wave 500 mW Nd:YAG diode pumped laser (1064 nm) [Forte 1064-S, Laser Quantum Ltd.] was used. It is sufficiently powerful for the intensities (I) required to interact with the colloidal particles ($I \approx 0.2$ mW μm^{-2} compared to $I \approx 0.02$ mW μm^{-2} recorded by Kawata,[6] and has a sufficiently long coherence length of > 240 mm. To create interference fringes, the coherence length of the laser must be greater than the pathlength difference between the two wavefronts. Twice the distance between the TIR interface and the spherical retroreflector is around 300 mm, and so the coherence length of the laser should be greater than that. To minimise losses, optics were purchased with anti-reflection coatings for 1064 nm and mirrors were gold-coated, wherever possible.

A Faraday Isolator [IO-3-1064-HP, OFR] prevents the retroreflected beam from returning to the laser, to avoid distortion and instability in the wavefront and potential damage to the laser. The Faraday isolator consists of a Faraday Rotator (a glass cylinder within a magnetic field) sandwiched between two air-gap polarizer cubes aligned 45° to each other (Figure 2.4). The input polariser (P1) was aligned to allow the entire forward beam through. As the light passes through the Faraday Rotator, the magnetic field rotates the polarisation by 45° (the Faraday Effect), and so the output polariser (P2) is rotated 45° to P1. Any reflected light returns through P2, and is rotated a further 45° within the Faraday Rotator. The returning beam is now polarised 90° to P1, and so is rejected by the polariser cube.

P1   Faraday Rotator   P2

Beam leaving laser

45°

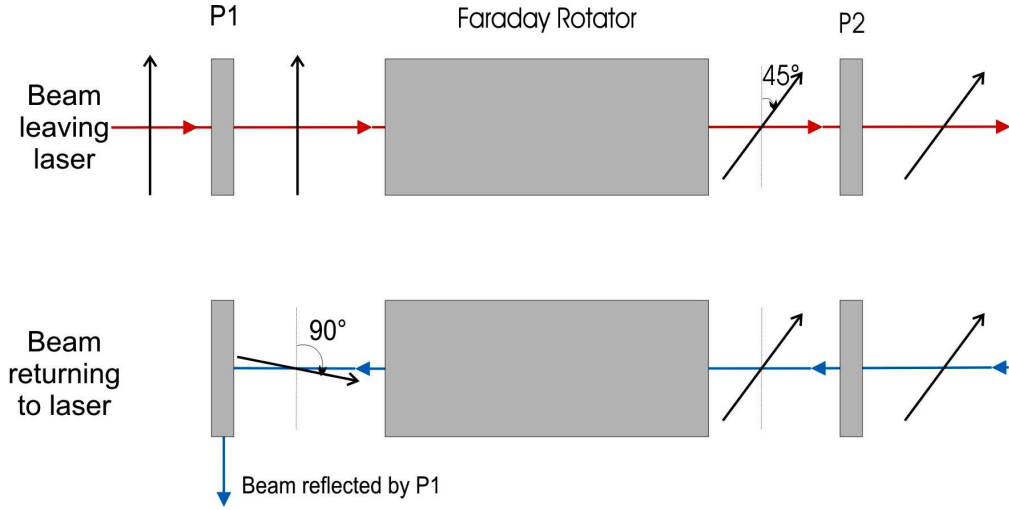Beam returning to laser

90°

Beam reflected by P1

Figure 2.4: Schematic showing a Faraday Isolator. Black arrows indicate the polarisation of light.

After the Faraday Isolator, there is a $\lambda/2$ waveplate to allow either *s*- or *p*-polarised light to be used in the experiments. The beam is then expanded by a Galilean telescope (a concave lens with focal length f = -50 mm, followed by a convex lens with f = +250 mm) from ≈ 1 mm to a beam diameter of 6 mm.

The hazardous 1064 nm Nd:YAG laser used for trapping is invisible, and so a low power visible laser was used for most of the alignment. A 633 nm He:Ne laser at 1 mW was directed onto the beam axis using a mirror mounted in a flipper mount [New Focus, model 9891].

A standard microscope (DM/LM, No. 11888500, Leica) was used as the basis of the experiment, with the hemispherical lens [BK7 or SF10, diameter = 10.0 mm] mounted on the microscope stage (Figure 2.3(b)). The beam was raised via a periscope and focused onto the flat prism surface using a convex lens with focal length f = +50 mm [Newport, KPX082AR.33]. To create evanescent waves that

penetrate sufficiently far into the sample to interact strongly with colloidal particles of diameter $2a \approx D$ near the TIR interface, the angle of incidence needs to be just above the critical angle. As the incidence angle approaches the critical angle, the penetration depth increases steeply (Equation(2.11)). However, the beam is focussed and can be thought of as an infinite sum of plane waves with a spread of incident angles. For total internal reflection of the entire beam, the spread of angles should be no more than half the difference between the incident angle and the critical angle. The N.A. of a lens is given by

$$N.A. = \sin\left(\frac{\varphi}{2}\right) = \frac{d}{2f} \qquad (2.25)$$

where φ is the focussing angle, d is the diameter of the beam before the lens, and f is the focal length of the lens. If $d = 6$ mm, and $f = 50$ mm, then the focussing angle $\varphi = 6.8°$.

$$(\theta_i - \theta_c) \geq \frac{\varphi}{2} = 3.4°$$

The hemispherical lens was either BK7 [n_{BK7} =1.507; $\theta_c(BK7)$ = 62.2°] or SF10 [n_{SF10} = 1.702; $\theta_c(SF10)$ = 51.6°] glass. Table 2.1 shows the fringe spacings D and penetration depths d_p for the incident angles and incident media used, as calculated using Equations (2.11) and (2.14).

Incident angle, θ_i	BK7		SF10	
	Fringe spacing, D/ nm	Penetration depth, d_p/ nm	Fringe spacing, D/ nm	Penetration depth, d_p/ nm
53			392	640
56			378	370
60			362	270
64	393	705	348	226
68	382	400	338	200

Table 2.1: Fringe spacings and penetration depths for the different incident angles and incident media used [λ= 1064 nm; n_{BK7} =1.507; n_{SF10} = 1.702; $\theta_c(BK7)$ = 62.2°; $\theta_c(SF10)$ = 51.6°].

The beam was retroreflected to the same spot at the glass-water interface with a spherical mirror, thus creating interference fringes in the overlapping evanescent fields. The spherical mirror was made in-house by coating a concave lens [f = -150 mm, radius of curvature = 77.52 mm, Newport KPC031] with chromium and then gold in a thermal evaporator. The chromium layer allows the gold to adhere to the substrate. The spherical mirror is mounted directly onto the microscope stage with three fine control actuators to focus the reflected spot as required. Since the spherical mirror and prism are connected, the mirror does not need to be readjusted whenever the stage is raised to refocus the objective.

For some of the experiments a $\lambda/4$-waveplate was inserted into the beam path between the spherical mirror and the prism. When the $\lambda/4$-waveplate has its fast axis aligned 45° to the polarisation of the forward beam, two passes through the $\lambda/4$-waveplate rotates the plane of polarisation of the returning beam by 90°. The two beams are now orthogonally polarised with respect to each other. The $\lambda/4$ waveplate must be used with the polarising beamsplitter cube (PBC) [10BC16PC.9, Newport] and power meter in place (Figure 2.3(a)). The PBC allows p-polarised light to pass straight through, while s-polarised light is reflected by 90°. If the forward beam is p-polarised and the returning beam is s-polarised, the PBC prevents the reflected beam from returning to the laser source via the Faraday Isolator. When the $\lambda/4$-waveplate has converted the returning beam to s-polarised light, the power meter reading is at its maximum.

The evanescent spot was observed by a CCD camera [JVC TK-S350] via the microscope objective (100x magnification, N.A. = 1.25, oil immersion [C Plan, No. 11506072, Leica]). An IR filter placed before the CCD camera was used to screen scattered laser light, and prevent bleaching of the camera. A series of magnification lenses were mounted on a wheel so as to allow the magnification to be changed between 100 x 1.0, 100 x 1.5, and 100 x 2.0 during the experiment.

Above the magnification lens, a convex tube lens focuses the light onto the CCD chip of the camera. MPEG-2 videos were recorded on a computer using a PCI framegrabber [WinTV2K Version 4.0.21126, Hauppage] and observed during experiments on a separate monitor.

2.2.2. Optical trapping using a tunable Ti:sapphire laser

The Ti:Sapphire optical trapping setup incorporates several improvements:

- A tunable laser was used to optically trap PS microspheres of different sizes allowing near-continuous tuning of *ka*. This enabled experimental study of array formation as the node/ antinode affinity of individual particles approached zero (See Figure 1.9). From Taylor's calculations,[7] the crossover point occurs at *ka* =1.985 and 3.263. For my experiments, the first crossover point is expected for a PS particle diameter of 420 nm with trapping wavelengths λ_{H2O} =665 nm, or λ_{air} =886 nm (Figure 2.5). The second crossover point is expected for 700 nm PS at λ_{H2O} =674 nm, or λ_{air} =898 nm, which is just out of the tuning range for the Coherent Indigo-S oscillator.
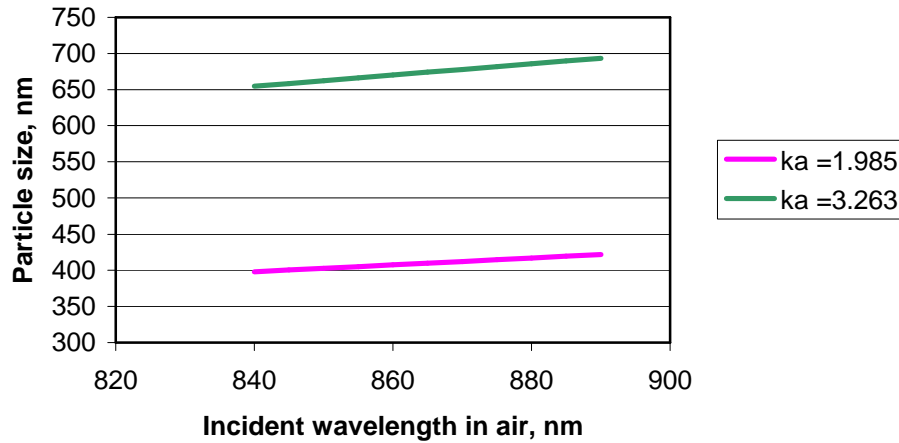
Figure 2.5: Plot showing particle size vs wavelength for ka values where the particles is attracted to neither bright nor dark interference fringes, based on the calculations of Taylor *et. al.*[7]

- A more powerful laser and a 50:50 beamsplitter were used to generate two separate trapping beams (in contrast to previous work with a single beam and a retroreflecting mirror). One of the beam paths included a delay line so as to introduce a pathlength difference. A pathlength difference greater than the coherence length leads to mutually incoherent beams arriving at

the TIR interface. This enables experimental study of optical trapping and binding in non-interfering evanescent fields.

- To adjust the focus of the microscope objective, the objective is translated instead of the hemisphere. Thus, the TIR interface is not moved during the experiment and the trapping beams remain well aligned relative to the centre of the hemisphere.

- The microscope optics are designed to provide even illumination that fully fills the numerical aperture of the microscope objective (described further in Section 2.2.2.1).

- Videos were recorded using an area scan CMOS camera [Pixelink PLB761U], instead of a CCD camera [JVC TK-S350] with interlaced readout. The CMOS camera resolved previous issues such as interlaced readout, and enabled better control of exposure time, gain and frame rate.

A schematic of the Ti:sapphire optical trapping setup is shown in Figure 2.6.

Figure 2.6: Schematic showing the optical bench layout for optical trapping in evanescent waves using a Ti:Sapphire laser.

The trapping laser is the infrared fundamental emitted from a Ti:sapphire oscillator [Coherent Indigo-S] which is tuneable over the range λ= 840-890 nm. The output power of the laser varies less than 10% over the wavelength tuning range Table 2.2. The Ti:sapphire laser is driven by a frequency-doubled Nd:YAG source, at a frequency of 4.0 kHz. The Coherent Indigo-S is a pulsed laser source, but can be treated as quasi-continuous with a long pulse width of 35 ns.

Wavelength, λ/nm	Pump current, I/A	Output Power, W
840.2	16.2	1.275
849.8	16.3	1.327
860.0	16.5	1.322
865.0	16.4	1.320
870.5	16.5	1.337
880.0	16.9	1.347
890.5	17.3	1.360

Table 2.2: Output power for the Coherent Indigo-S measured between the first mirror and the Faraday isolator shown in Figure 2.6. The pump current is adjusted slightly when the wavelength is changed to ensure that only one lasing mode is excited.

A broadband Faraday Isolator [Thorlabs IO-5-TiS2-HP] prevents any retroreflected light from returning to the oscillator. The beam diameter is then expanded from 2 to 5 mm by a Galilean telescope (two achromatic doublet lenses with focal lengths, f= -25 mm[Thorlabs ACN 127-025-B], and f = +50 mm[Thorlabs AC 127-050-B]).

Trapping beam power is attenuated using a zero-order λ/2 waveplate [Edmund Optics NT46-413] and a polarising beamsplitter cube [Edmund Optics NT49-870]. The polarising beamsplitter cube only transmits p-polarised light, so rotation of the zero-order waveplate will allow all or none of the beam to pass into the rest of the optical setup as horizontally polarised light. Next, an

achromatic $\lambda/2$ waveplate [Edmund Optics NT46-561] allows selection of horizontally or vertically polarisation. Placement of mirrors and other reflecting surfaces in the optical beam path has been carefully considered to ensure that both beams reach the TIR interface with the same linear polarisation.

The trapping beam is then split along two beam paths using a 50:50 beamsplitter cube [Thorlabs BS011]. One beam path incorporates a delay line comprised of a 25 mm right angle prism mounted with 25 mm horizontal translation (resulting in a path length difference of zero to 50 mm). For light with a Lorentzian optical spectrum, the coherence length L_{coh} can be defined as[8]

$$L_{coh} = c\tau_{coh} = \frac{c}{\pi\Delta\nu} = \frac{1}{\pi\Delta\tilde{\nu}}$$

τ_{coh} is the coherence time, $\Delta\nu$ is the full-width at half-maximum of the optical bandwidth (in Hz), and $\Delta\tilde{\nu}$ is the full-width at half-maximum of the optical bandwidth (in cm^{-1}). Since the Coherent Indigo-S has a single-shot linewidth of <1 cm^{-1}, $L_{coh}\approx$ 3 mm. A path length difference of 50 mm is therefore sufficient to enable optical trapping experiments to switch between mutually coherent and mutually incoherent laser beams.

Both beams are then raised via periscopes and focused using f = +50 mm achromatic doublet lenses [Thorlabs AC127-050-B] onto the flat surface of a BK7 half-ball lens with an incident angle, θ_i = 64.5˚. At the BK7 surface, the laser spot is approximately 20 μm x 30 μm (20 μm along the y-axis, and 30 μm along the x-axis). Table 2.3 shows the fringe spacing, D and penetration depth, d_p as the incident wavelength is varied over λ= 840-890 nm.

Wavelength, λ/nm	Fringe Spacing, D/ nm	Penetration Depth, d_p /nm
840	309	556
850	312	563
860	316	570
870	320	576
880	323	583
890	327	590

Table 2.3: Fringe spacings and penetration depths for optical trapping with the Ti:sapphire laser [λ= 840-890 nm; n_{BK7} =1.507; $\theta_c(BK7)$ = 62.2°, $\theta_i(BK7)$ = 64.5°]. Uncertainty in θ_i of ±0.5° translates to an error of ±2 nm in fringe spacing.

As on the previous optical trapping setup, the hazardous λ= 840-890 nm laser is invisible. A low power 633 nm He:Ne laser at 1 mW was used for most of the alignment. The red alignment beam was directed onto the infrared beam path using the two irises indicated in Figure 2.3, and a mirror mounted in a flipper mount [New Focus, model 9891].

2.2.2.1.Microscope imaging

To maximise the large numerical aperture of the microscope objective (N.A. =1.25), a condenser should be placed under the sample in an upright microscope (Figure 2.7). The function of a condenser is to produce even illumination at large angles to match the numerical aperture of the microscope objective.[1, 9] The collector and condenser lenses act to produce parallel rays of illumination at the sample plane from any one point of the illumination source. This form of microscope illumination is call Kohler illumination. This type of illumination ensures that the optical resolution of the microscope objective is fully utilised and that even illumination is obtained without imaging the light source.

Even though any one point of the LED light source produces coherent illumination at a range of angles, the total illumination from all points of an extended source is almost incoherent since each coherent plane wave will have random phases. When the sample is incoherently illuminated, the resolution limit is given by the Rayleigh criterion[1]

$$d = {0.61\lambda}/{N.A.}$$

where *N.A.* is the numerical aperture of the objective, λ is the wavelength of illumination, *d* is the distance between the objects. Thus

$$d \approx 320 \text{ nm}$$

if imaging in blue light λ =455 nm, N.A. = 1.25, and *n* =1.333. (The microscope objective used is corrected for chromatic aberrations.) Aberrations in the optics will reduce the optical resolution from the theoretical limit.
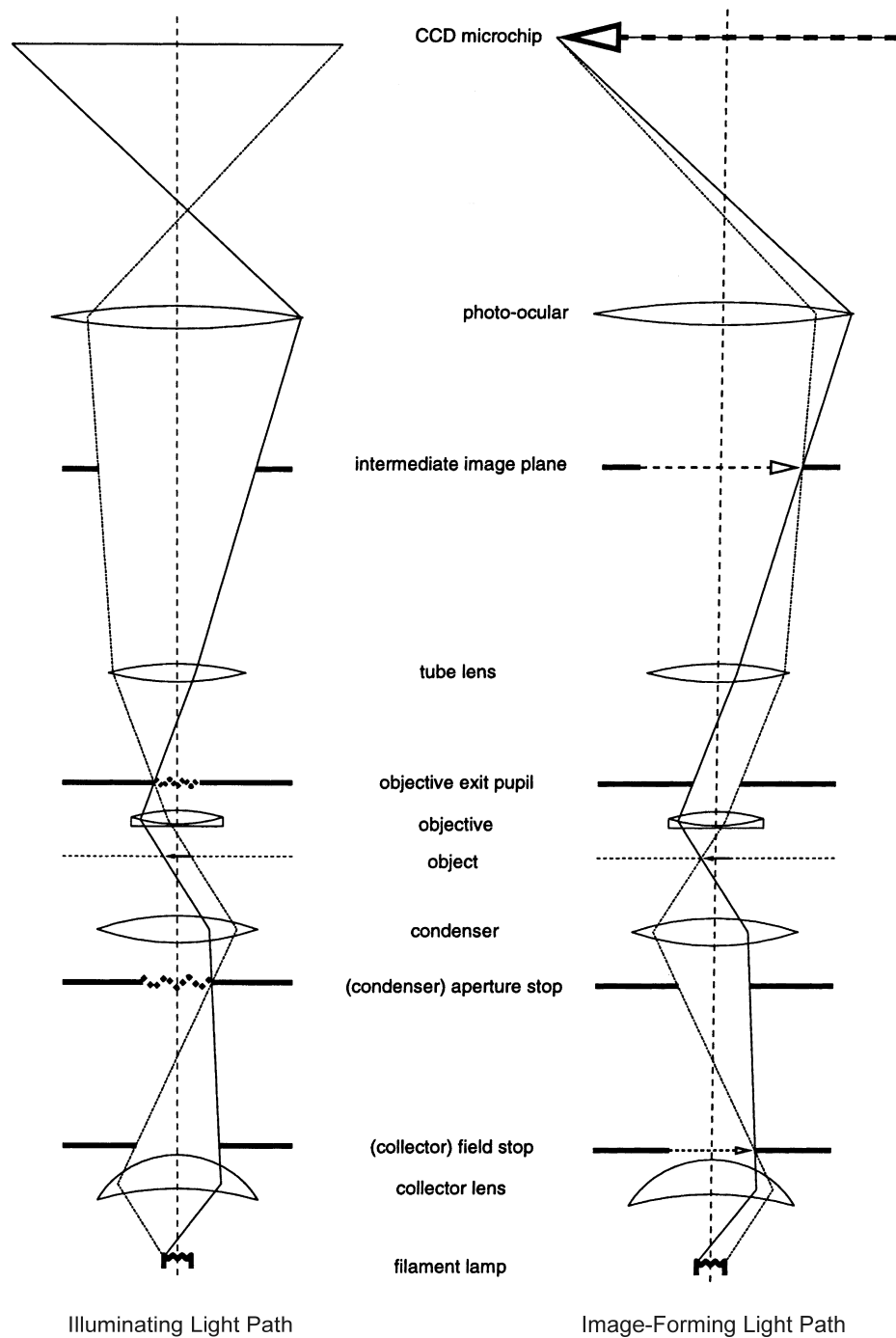
CCD microchip

photo-ocular

intermediate image plane

tube lens

objective exit pupil

objective

object

condenser

(condenser) aperture stop

(collector) field stop

collector lens

filament lamp

Illuminating Light Path   Image-Forming Light Path

Figure 2.7: Ray-tracing diagrams for an infinite-tube length compound microscope set up for Kohler illumination. For the illuminating light path, the filament lamp, condenser stop and objective exit pupil are shown to be in conjugate planes. For the image-forming light path, the collector stop, object, intermediate image plane and CCD microchip are shown to be in conjugate planes. In my setup, the photo-ocular is absent so the CCD is positioned at the intermediate image plane (or the back focal plane of the tube lens).[9]

The illumination optics in a typical standard microscope (e.g. DM/LM, Leica) consist of an aspheric collector lens, and a simple two-lens Abbe condenser. In place of an aspheric collector lens, I used two off-the-shelf achromatic doublets [Thorlabs AC254-030-A1, and AC508-075-A1], shown as L1 and L2 in Figure 2.8. In place of an Abbe condenser, the BK7 half-ball lens (which is necessary for creating the evanescent fields by TIR) is used in combination with lenses L3 [Thorlabs AC508-075-A1] and L4 [Thorlabs AC254-030-A1] to produce illumination at large angles at the sample plane.
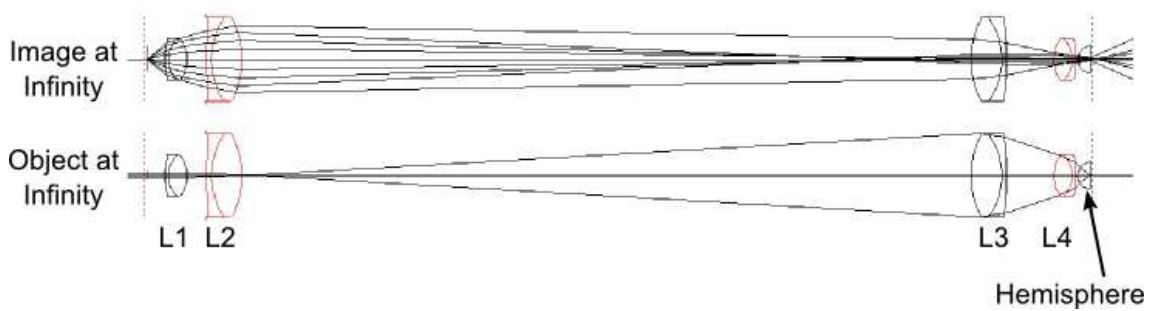
Figure 2.8: Ray tracing diagrams for the illumination optics on the Ti:sapphire optical trapping setup showing: (Image at infinity) Rays from a single point of the light source are out of focus on the flat face of the hemisphere; (Object at infinity) Parallel rays from the light source are focused at large angles on the flat face of the hemisphere. To achieve Kohler illumination, components should be separated by the distances shown in Table 2.4.

WinLens [published by LINOS Photonics], a simple raytracing program, was used to configure the illumination optics. To achieve Kohler illumination using the optics shown in Figure 2.8, the optics should be separated by the distances listed in Table 2.4 below. Rays from a single point of the light source are out of focus on the flat face of the hemisphere. Parallel rays of light from the LED light source are focused at large angles on the sample plane, resulting in illumination N.A.= 0.90.

Optical Component	Separation, mm
LED	0
L1	12.1
L2	12.9
L3	476.5
L4	31.1
BK7 Hemisphere	1.5

Table 2.4: Separation between optics shown in Figure 2.8, as calculated by paraxial raytracing in Winlens. Separation is calculated as the distance between the last surface of the preceding optical component and the first surface of the optical component listed on the left.

The evanescent spot was imaged using a CMOS camera [Pixelink PLB761U] via a microscope objective (100x magnification, N.A. = 1.25, oil immersion [HI Plan, No. 11506238, Leica]), as shown in Figure 2.9. Magnification lenses were mounted using screw-in lens tubes to enable magnifications of 100 x 2.0 during the experiment. Above the magnification lenses, an IR filter was placed to prevent scattered laser light from bleaching the camera. Next, an achromatic doublet lens [f=+200 mm, Thorlabs AC25-200-A1] focuses an image of the sample plane onto the CMOS detector. Videos were recorded on a computer via a USB link, at a frame rate of 50Hz.
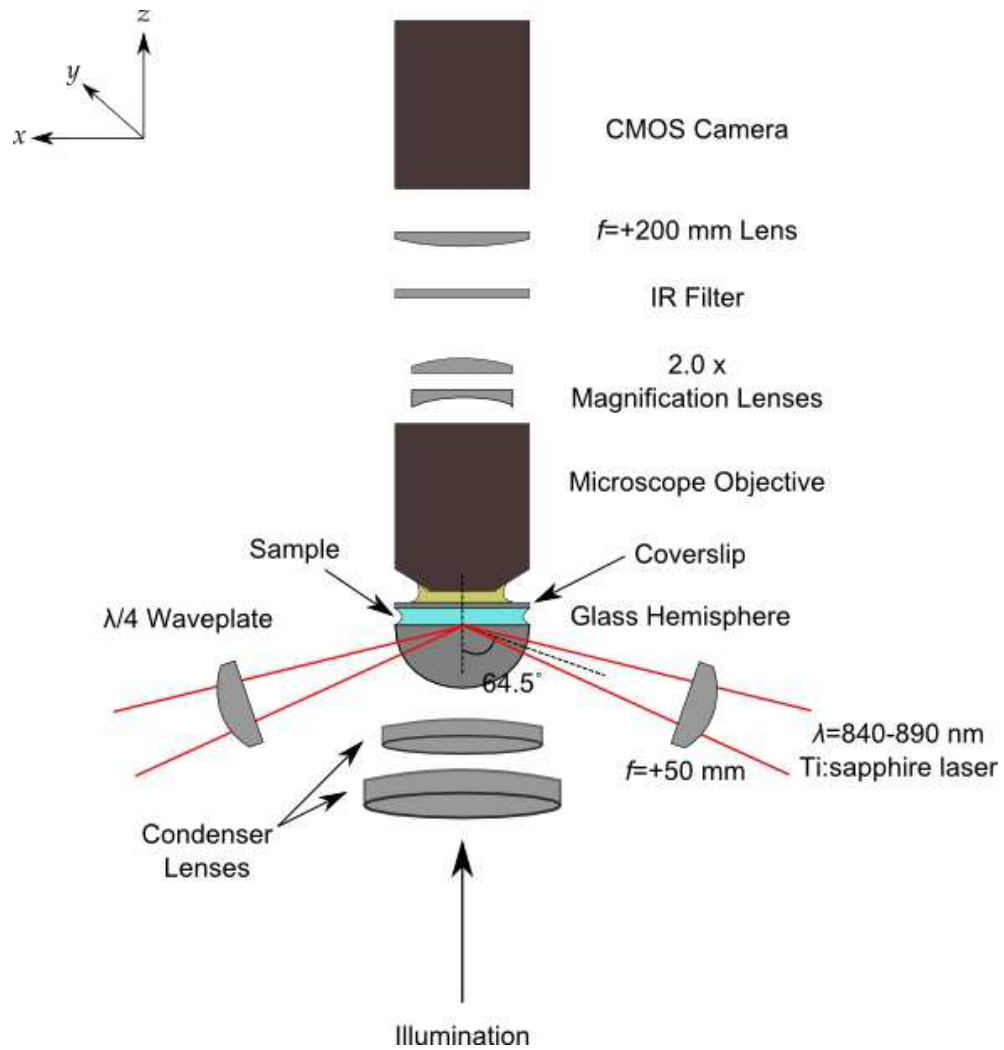
Figure 2.9: Schematic showing a close-up of the experimental setup around the

BK7 hemisphere for optical trapping in evanescent waves generated by TIR

with a Ti:sapphire λ= 840-890 nm laser.

2.3. Sample preparation

One drop of the sample was sandwiched between the half-ball lens (diameter = 10 mm) and a coverslip [L4096-2, Agar Scientific]. During experiments, evaporation of the sample led to capillary currents destabilising the particle arrays. To reduce this effect, an excess of lens immersion oil [L4082, Agar Scientific] was applied on top of the coverslip and allowed to overflow the edges of the prism. This technique was messy but enabled stable trapping experiments to run for over 20 minutes.

The half-ball lens was cleaned in acetone using an ultrasonic bath for 15 minutes. It was then rinsed with ethanol, and then rinsed several times in deionised water. The lens was further sonicated for 15 minutes in 70% concentrated nitric acid, before multiple rinses in deionised water. Finally, the lens was dried under nitrogen. This cleaning procedure removed most particle aggregates, as well as any dirt that might allow particles to adhere to the prism surface. The polystyrene (PS) have a slight negative charge originating from the sulphate groups on the particle surface, while the Au particles are stabilised by citrate present from their synthesis. As a result, the negative charge of the clean BK7 or SF10 surface is usually sufficient to prevent adhesion of negatively charged particles.

2.3.1. Polystyrene

PS solutions (Bangs Labs 390 nm [PS02N/6703], 420 nm [PS02N/2141], 460 nm [PS02N/5895], 620 nm [PS03N/ 6001], 700 nm [PS03N/ 6012], 800 nm [PS03N/6388]; Agar Scientific Ltd. 520 nm [S130-6], 300 nm [S130-5], 945 nm [S130-7]) and silica solution (Bangs Labs 520 nm [SS03N/7190]) were diluted 1:1000 with deionised water (Millipore), or 10 μM NaCl solution.

2.3.2. PVP-PEGMA

Poly(ethylene glycol) methacrylate (PEGMA) stabilised poly-2-vinylpyridine (P2VP) microspheres were synthesised by Damien Dupin[10, 11] in 3 diameters: 380, 640 and 830 nm. The PEGMA-P2VP microspheres were provided as suspensions in water and were diluted by 1:2000 (380nm) or 1:1000 (640 and 830 nm) into a solution of 0.62 mM cetyl trimethylammonium bromide (CTAB).

The presence of 0.62 mM CTAB is sufficient to prevent the adhesion of PEGMA-P2VP to the negatively charged glass surface during trapping experiments. The cationic surfactant adsorbed to the negatively charged BK7 surface so that PEGMA-P2VP no longer adhered to the BK7 surface, even during optical trapping at maximum laser power. The diluted samples were pH 8, regardless of CTAB concentration. Our collaborators measure a small negative charge on the microspheres at pH 8 by electrophoresis (Figure 2.10),[11] which seems to contradict our observation that a cationic surfactant is necessary in preventing the PEGMA-P2VP from adhering to the glass-water interface during evanescent wave optical trapping experiments.
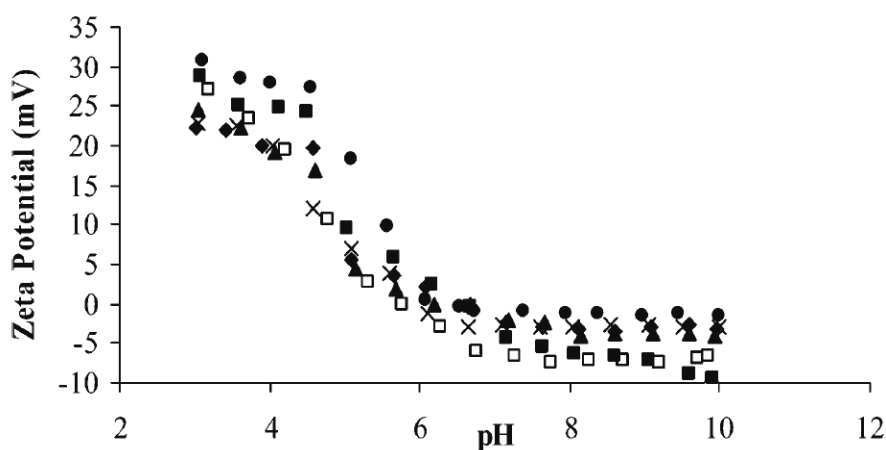

Figure 2.10: Electrophoretic mobility vs pH curves obtained for 0.01 wt% aqueous solutions of PEGMA-P2VP latexes in the presence of 0.01 M NaCl: (♦) 370 nm diameter; (▲) 480 nm diameter; (x) 560 nm diameter; (□) 640 nm diameter; (●) 830 nm diameter; (■) 1010 nm diameter.[12]

2.3.3. Au

The Au solution (British Biocell International 250 nm [GC250]) was diluted 1:5, and then the particles were allowed to settle out overnight. Half the supernatant was removed by pipette and the remainder was shaken up to redistribute the colloid. The Au colloid is supplied with citrate stabilisers to prevent aggregation of the particles. The ionic strength of undiluted Au solution is high enough to allow adhesion of Au particles to the BK7 surface during experiments, but a fivefold dilution removes this problem. Sonication of the sample for ~5 minutes helped reduce the number of colloidal aggregates observed in the sample.

2.3.4. Janus particles

Janus particles (881 nm amino-modified silica, coated with 10 nm Cr and 20 nm Au) were kindly prepared by Olivier Cayre using a gel trapping technique[12]. Aggregates within the sample were broken up using a VC-505 Sonics Vibracell ultrasonic horn (3mm tapered microtip, four 5-second pulses at 36% amplitude). For comparison, 2% wt. 881 nm amino-modified silica was also supplied, which was diluted 1:100 with deionised water before use.

2.4. Measurement of lattice parameters

An IR filter is required to prevent saturation of the camera due to the strong scattering of the laser light by the colloidal particles. With the IR filter in place, the weak scattering off imperfections at the glass-water interface is undetectable. The interference pattern can therefore only be inferred from the movements of the colloidal particles on interaction with the evanescent fields.

The DM/LM Leica microscope was calibrated using a stage micrometer with a 100 μm scale and 2 μm sub-divisions[Agar Scientific L4202, line width= 1 μm, overall accuracy = ±1 μm]. At a magnification of 150x, each image pixel is 47.6 nm, and 43.3 nm along the x- and y-axis, respectively. This calibration has 1%

uncertainty associated with the accuracy of the stage micrometer.

On the Ti:sapphire optical trapping setup, the position of the f=+200 mm tube lens needed fine adjustment to produce the correct magnification. The stage micrometer was found to be too grainy for fine calibration, and so a 1000 lines per mm holographic diffraction grating film [Edmund Optics NT01-307] was used instead. At a magnification of 100x, each image pixel is 59.86 nm in both x- and y-axes.

Videos were recorded in 25 Hz MPEG-2 and 50 Hz .avi formats on the Nd:YAG λ=1064 nm, and Ti:sapphire λ=840-890 nm optical trapping setups, respectively. Wherever possible, 50 consecutive video frames of stable trapped arrays were extracted as .JPEG files using VirtualDub-MPEG2 1.6.19. In Matlab, the images were processed with an algorithm comprised of bandpass, peak find, centroid weighting, particle tracking and particle sorting routines to calculate average particle positions and their associated statistical error.[13-15] Since particle positions are typically averaged over 100 frames, dimensions are quoted with sub-pixel accuracy[14]. Uncertainties in particle positions and array lattice parameters are quoted as standard error of the mean $\sigma_{\bar{x}}$.

$$\sigma_{\bar{x}} = \frac{\sigma_x}{\sqrt{N}} = \sqrt{\frac{\sum_i (x_i - \bar{x})^2}{N(N-1)}} \qquad (2.26)$$

If N measurements of particle position, x_i were repeated there should be a 68% probability the new mean value of would lie within $\bar{x} \pm \sigma_{\bar{x}}$.

Larger PS particles of diameters 620nm -800nm are imaged as dark donuts with a bright centre against a bright background. A semi-automatic flood-fill routine is run on the image to generate a background that is even darker than the 'dark' donut (Figure 2.11). The flood-fill routine starts near the edges of an image and darkens adjacent pixels until a pixel which is much darker is encountered. The

user can input parameters to control the boundary value at which the flood-fill routine detects the particle edge. The particle centres are not darkened and can then be detected correctly using the bandpass and peak find routines.
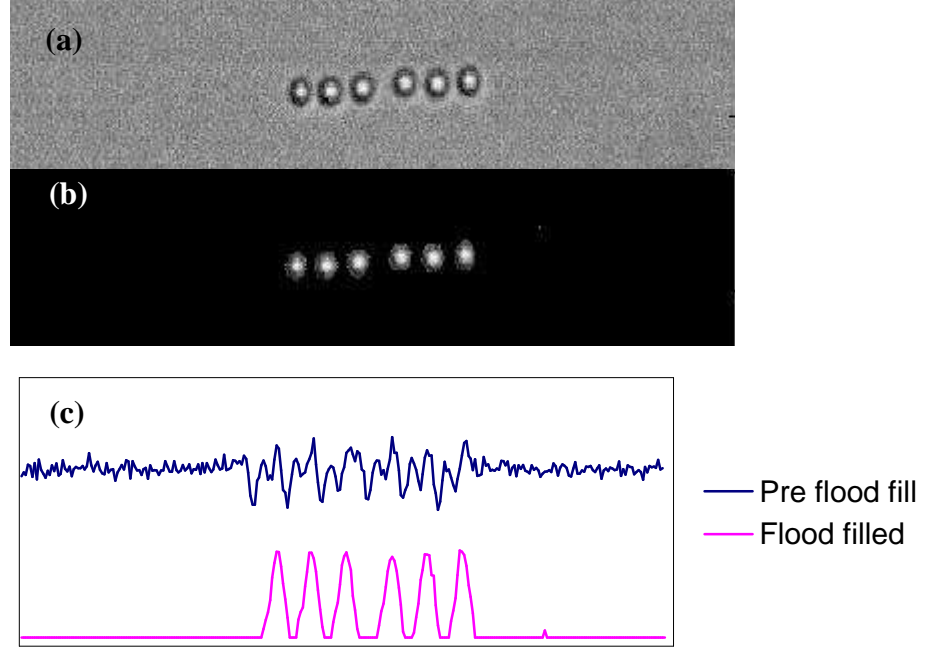

Figure 2.11: Line array of 620 nm PS (λ= 880 nm, *p*-polarised): (a) unprocessed image; (b) image after flood fill routine; (c) line profiles of images before and after.

2D FFT in Matlab was also used to obtain array lattice parameters. For square and hexagonal arrays, the values obtained agreed with those obtained by particle tracking. For modulated arrays, it was more difficult to interpret the FFT peaks to obtain the appropriate lengthscale. Tilted arrays gave a 'tailing' effect on the 2D FFT plot. For consistency, I used the particle tracking routine for all arrays.
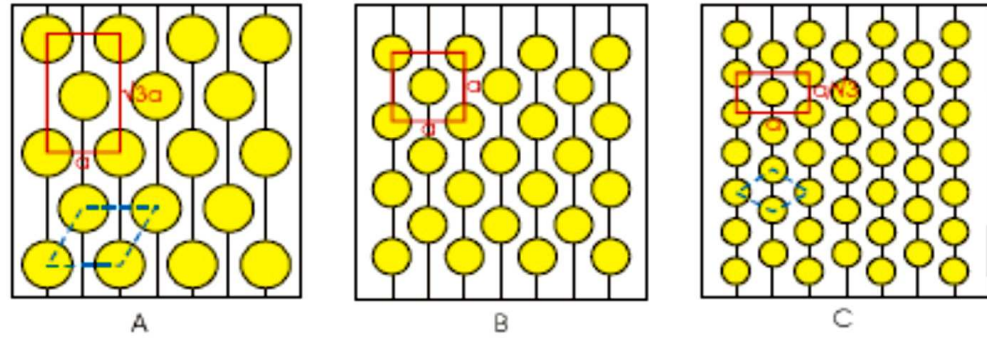
Figure 2.12: Commensurate lattices formed on interference fringes: (A) is a hexagonal lattice denoted hex1, where $b = \sqrt{3}a$; (B) is a square lattice (*a=b*); and (C) is a hexagonal lattice denoted hex2, where $a = \sqrt{3}b$. Centred rectangular unit cell shown in red; primitive hexagonal unit cells shown in blue dashes.[16]

Lattice parameter *a* is the particle spacing along the direction of propagation of the incident light, and lattice parameter *b* is the particle spacing along the interference fringes (Figure 2.12). When array spacings are commensurate with the interference fringes, the appearance of square or hexagonal packing can be rationalised as follows: If a square array(*a=b*) is used as a starting point(Figure 2.11(b)), increasing the effective particle size expands the *b* parameter. When $b = \sqrt{3}a$, the lattice is hexagonal, so denoted as hex1(Figure 2.11(a)). Conversely, decreasing the effective particle size leads to compression of the *b* parameter to a point where the lattice is hexagonal ($a = \sqrt{3}b$), but with a unit cell that is a 30° rotation of the hex1 case. This second type of hexagonal array is denoted hex2 (Figure 2.11(c)).

Experimentally formed arrays are very often distortions of the above array types. The halfway point between square and hex1 is $b = 1.366a$. If $1.00a < b < 1.30a$, the array is unambiguously hex1. If $1.30a < b < 1.40a$, the array is described as a square-hex1 intermediate. Similarly, if $1.00b < a < 1.30b$, the array is unambiguously hex2. If $1.30b < a < 1.40b$, the array is described as a square-hex2 intermediate.

References

1.   S. G. Lipson, H. Lipson and D. S. Tannhauser, *Optical physics*, 3rd edn., Cambridge Univ. P., Cambridge, 1995.

2.   E. Hecht, *Optics*, 3rd edn., Addison-Wesley, Reading, Mass., 1998.

3.   J. M. Taylor, Doctoral thesis, Durham University, 2009.

4.   T. Cizmar, E. Kollarova, Z. Bouchal and P. Zemanek, *New Journal of Physics*, 2006, **8**, 23.

5.   J. P. Barton, D. R. Alexander and S. A. Schaub, *Journal of Applied Physics*, 1989, **66**, 4594-4602.

6.   S. Kawata and T. Sugiura, *Optics Letters*, 1992, **17**, 772-774.

7.   J. M. Taylor, L. Y. Wong, C. D. Bain and G. D. Love, *Optics Express*, 2008, **16**, 6921-6929.

8.   D. R. Paschotta, *Encyclopedia of Laser Physics and Technology*, RP Photonics Consulting GmbH, http://www.rp-photonics.com/coherence_length.html, 2009.

9.   M. S. Elliot and W. C. K. Poon, *Adv Colloid Interfac*, 2001, **92**, 133-194.

10.   D. Dupin, S. P. Armes, C. Connan, P. Reeve and S. M. Baxter, *Langmuir*, 2007, **23**, 6903-6910.

11.   D. Dupin, S. Fujii, S. P. Armes, P. Reeve and S. M. Baxter, *Langmuir*, 2006, **22**, 3381-3387.

12.   V. N. Paunov and O. J. Cayre, *Advanced Materials*, 2004, **16**, 788-791.

13.   D. Blair and E. Dufresne, *http://physics.georgetown.edu/matlab/*.

14.   J. C. Crocker and D. G. Grier, *J Colloid Interf Sci*, 1996, **179**, 298-310.

15.   M. K. Cheezum, W. F. Walker and W. H. Guilford, *Biophys J*, 2001, **81**, 2378-2388.

16.   C. D. Mellor, D. Phil. Thesis, University of Oxford, 2005.

3. Optical Trapping using λ= 1064 nm Nd:YAG

Array formation of submicron dielectric particles in counterpropagating evanescent fields was studied, using an experimental setup modified from Mellor's original setup.[1] The TIR incident medium was a hemispherical lens instead of an equilateral prism, so as to reduce astigmatism when focusing the incident laser beams. The following section describes array behaviour that was often qualitatively different from Mellor's observations, even though the experimental method was very similar. Optical binding phenomena are size and refractive index dependent, and so the following discussion is organised according to particle sizes and materials that display similar types of array behaviour.

3.1. Setting up the Optical Trapping Area

Rough alignment of the trapping beams was achieved with a low magnification objective (10x or 20x) by observing the He-Ne spots at the TIR interface in the absence of the infrared filter. Even though both beams were undergoing total internal reflection, speckle was visible at the TIR interface due to the coherent scattering from imperfections of the glass surface. Both forward and reflected beams were centred on the flat side of the half-ball lens and on the video monitor, and then focused using the f = +50 mm lens and spherical mirror (Figure 2.3(b)). A drop of sample was then sandwiched between the TIR interface and the glass coverslip. Immersion oil was applied to the coverslip, and the 100x objective was focussed at the glass-water interface. Fine adjustment of the He-Ne spots was then made before switching to the infrared beams. At low power, the speckle from the infrared laser beams was useful for confirming the alignment of the trapping area. The infrared filter could then be replaced, the 1064 nm laser power increased and particle interactions observed in brightfield illumination.

It was often useful to begin trapping with the laser spots slightly moved apart as shown in Figure 3.1(a). Particles that enter the non-overlapping evanescent fields would then be drawn towards the interface and pushed into the overlapped trapping region. When sufficient particles were collected in the trapping region, the spots were moved closer together to increase the stable trapping area. When the forward and retroreflected beams have the same polarisation, interference fringes are formed by the overlapped evanescent fields. Particles that interacted with the interference fringes were restricted to one-dimensional Brownian motion along the interference fringes. Since the interference fields were not directly imaged, the overlap and interference fringes were inferred by the motion of particles. As previously reported by Mellor,[1] at low particle densities, particles diffuse up and down the fringes independent of each other.
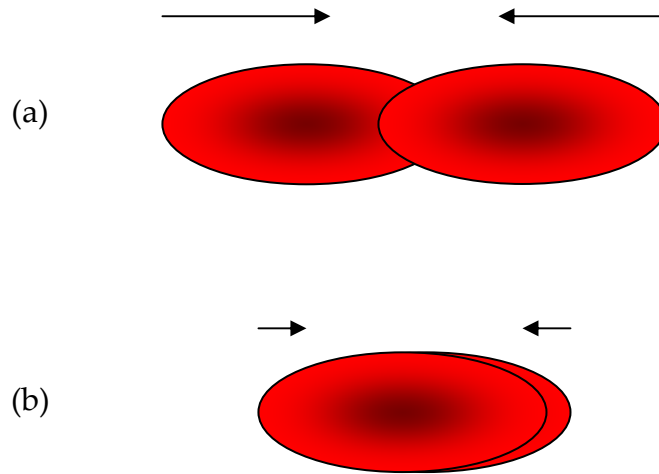
Figure 3.1: Illustration of (a) how the laser spots are arranged at the start of an experiment, and (b) how they are overlapped as the array forms. Particles are trapped within the overlapped evanescent fields, but feel translational forces (indicated by arrows) in the non-overlapped areas which are useful for increasing particle movement into the array. Evanescent fields are ellipsoidal as the beams are impinging the TIR surface at an angle.

3.2. Polystyrene

3.2.1. Close packed arrays of small PS particles (390, 420 and 460 nm)

When the incident beams are *p*-pol and close to the critical angle (θ_i =53°; θ_c =51.6°; n_{SF10} =1.702), 460 nm PS particles formed a square array. Particle positions were commensurate with the interference fringes, as can be seen from the *a*-parameter in Table 3.1. On switching to incident *s*-pol, or orthogonal polarisation, the array became compressed along the fringe direction (Figure 3.2(b) and 'Video 3.1: 460nm PS compression'). Since the individual particles were difficult to resolve, *b* was estimated from the number of particles present along a fringe when individual particles could be resolved in *p*-pol(Table 3.1). Since the compressed array was assumed to be commensurate, then *a* =775 nm, *b* =570 nm and nearest neighbours are separated by only 480 nm. Particles in the tightly packed *s*-pol array were still separated by the electrical double layer repulsion, as the array readily broke up into individual particles when the trapping fields were turned off. Since the particles in the compressed array are virtually in contact with one another, this is an example of collapsed optical binding.[2] Smaller PS microspheres of diameters 390 and 420 nm formed similarly compressed and unresolvable arrays in both *s*-pol and *p*-pol. *P*-pol light scatters more strongly than *s*-pol light along the fringe direction,[2] giving rise to non-contact particle separations.
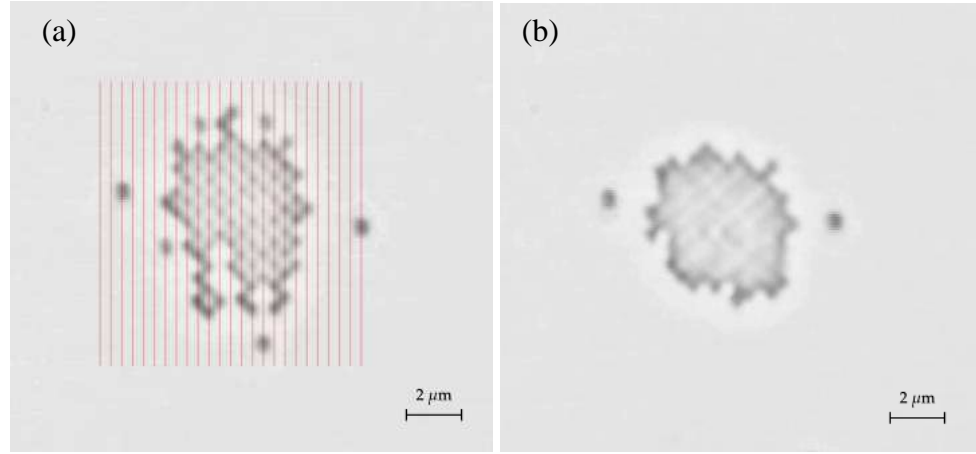
Figure 3.2: Arrays of 460 nm PS (a) in *p*-pol, forming a square array; (b) in *s*-pol, which is then compressed parallel to the fringes (θ_i =53°; D = 390nm; n_{SF10} =1.702°; λ=1064 nm).

Incident angle	Polarisation	*a*, nm	*a/D*	*b*, nm	Nearest neighbour separation, nm
53°	*s*	unresolved	-	≈ 570	-
	p	775±5	1.98	700±10	520
56°	*s*	780±5	2.07	705±10	525
	p	770±5	2.04	740±10	530

Table 3.1: Lattice parameters for square arrays of 460 nm PS, as shown in Figure 3.2

3.2.2. Broken hex2 arrays of 460 nm PS

Increasing the incident angle from 53° to 56° decreased the fringe spacing from 390 to 380 nm, while also decreasing the penetration depth (Table 2.1). At θ_i=53° in p-pol, lattice parameter a was commensurate with the fringe spacings. As the incident angle was increased to θ_i=56°, a was expected to decrease but in reality the array remained commensurate. The reduction in interference fringe spacing introduced strain which acted to destabilise the square lattice, and so other array types have been observed. Figure 3.3(a) shows a region of square packing coexisting with a region in which every third or fourth fringe was vacant, and the particles on the adjacent fringes were displaced towards the vacant fringe. Such 'broken' hexagonal structures are denoted broken hex2, and were first described by Mellor et $al.$ for 460 and 520 nm PS.[1, 3-5] The broken hex2 packing cannot be converted to a condensed array simply by filling in the vacant fringes, but also requires a lattice translation of half a unit cell in the b-direction for every other pair of particle columns. This requirement may provide some kinetic stabilization to the 'broken' hexagonal structure. Other intermediate structures were sometimes observed, such as three occupied fringes with the fourth fringe vacant (Figure 3.3(b)).
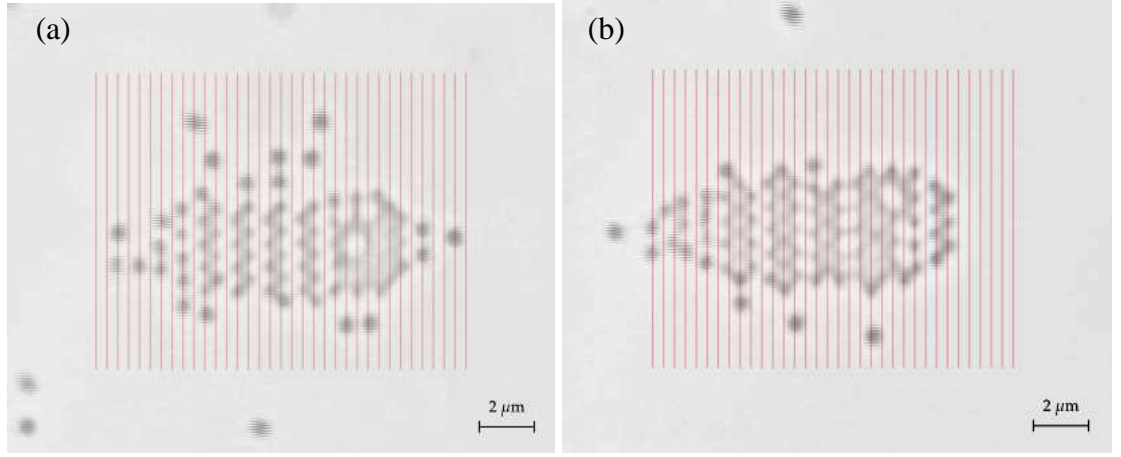
Figure 3.3: Arrays of 460 nm PS particles showing (a) an unstable broken hex2 array with every third fringe vacant; which rearranges to (b) a broken hex2 array with every fourth fringe vacant. These arrays are obtained in *p*-pol (θ_i =56°; D = 380 nm; n_{SF10} =1.702°; λ=1064 nm).

Generalized Lorenz-Mie theory (GLMT) simulations by Love *et. al.*[2] successfully reproduced broken hex2 arrays of 520 nm PS in *p*-pol, which are similar to the arrays shown above. When the incident beams are *p*-polarised, the scattered field from a particle located on a bright fringe has significant intensity along the interference fringe which acts to stabilise other particles occupying the same fringe. Particles of diameter 460 and 520 nm are too large to occupy every fringe in a hexagonal array, and so the most stable structure is one that contains vacant columns.
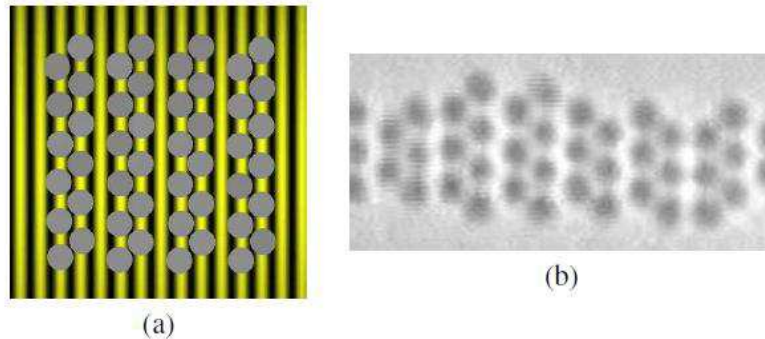
Figure 3.4: Broken hex2 array of 520 nm polystyrene particles: (a) a snapshot of a Brownian dynamics simulation[2] (b) experimentally observed array[3-5].

3.2.3. A discussion of array stability

Mellor observed that the transition from square to broken hex2 array could be effected reversibly by changing the polarization;[1, 3-5] I found however that once a large square array had formed it persisted in both incident polarisations (Figure 3.5). In my experiments, the evanescent fields are expected to be more intense due to reduced astigmatism in the focused of the laser beams. Increasing the field intensity would have the same effect as turning down the temperature, kT, and so I should expect a larger variety of array configurations (corresponding to local minima in potential energy). Instead, my experiments showed fewer rearrangements to kinetically stable structures once the arrays are in the lowest energy configuration. The electric field amplitudes, penetration depths and fringe spacings are, however, not identical in the two experiments and the most stable structure results from a subtle balance between optical trapping, optical binding and electrostatic repulsions.
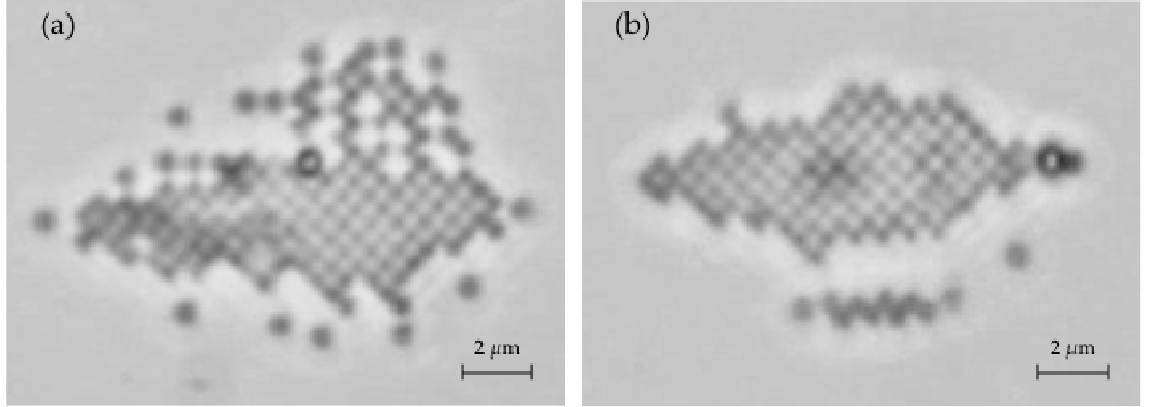
Figure 3.5: Arrays comprised of large numbers of 460 nm PS are square (a) in *p*-pol, but with many edge defects; (b) in *s*-pol. (θ_i =56°; D = 380nm; n_{SF10} =1.702°; λ=1064 nm).

3.2.4. Arrays of larger PS particles

3.2.4.1. Arrays of 620 nm PS

Arrays of 620 nm PS have hexagonal ordering, with the orientation of the unit cell dependent on incident beam polarisation. Figure 3.6(a) shows a commensurate hex1 array of 620 nm PS obtained in *s*-pol, and Figure 3.6(b) an incommensurate hex2 array in *p*-pol. Lattice parameters *a* and *b* for arrays of 620 nm PS are listed in Table 3.2. Particle positions in the incommensurate hex2 array were not solely due to interaction with interference fringes in the evanescent field. Light mediated interactions seem to stabilise the incommensurate hex2 array. On changing the incident polarisation from *p*-pol to *s*-pol, the incommensurate hex2 array rearranged to a commensurate hex1 array. The rearrangement was not instantaneous on changing the polarisation, and sometimes proceeded via a commensurate metastable square array that persisted for more than a minute (Figure 3.6(b)) before final rearrangement to the hex1 structure. The reverse transition from hex1 to hex2 occurs instantaneously on changing the polarisation from *s*-pol to *p*-pol. The forward and reverse rearrangements between hexagonal arrays appear to proceed via different metastable states with different energy barriers.
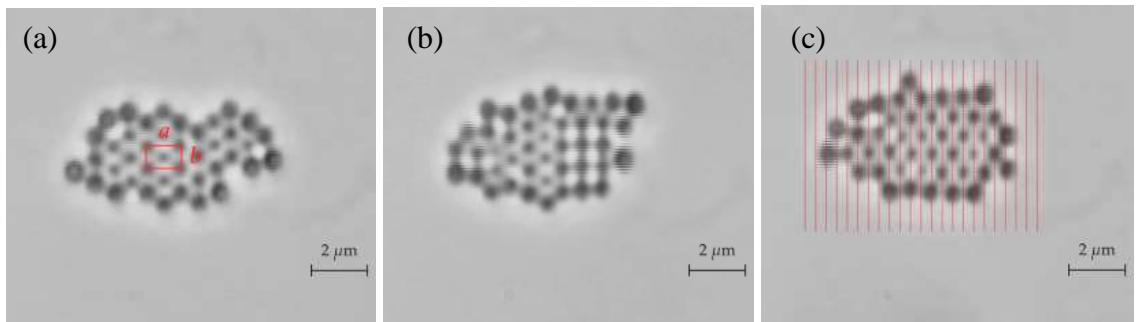

Figure 3.6: Arrays of 620 nm PS particles showing (a) incommensurate hex2 in *p*-pol, (b) transitory square in *s*-pol, and (c) commensurate hex1 in *s*-pol. (θ_i=60°; θ_c =51.6°; n_{SF10}=1.702°; λ=1064 nm)

Incident angle, θ_i Polarisation	a /nm	b /nm	a/D	Commensurate/ Incommensurate
56°; s	770±5	1165±15	2.03	Commensurate
56°; p	1190±5	720±10	3.14	Incommensurate
60°; s	735±5	1175±10	2.03	Commensurate
60°; s (transitory square)	705±5	665±10	1.94	Commensurate
60°; p	1175±5	770±20	3.24	Incommensurate
60°; orthogonally polarised	1205±5	720±20	3.32	Incommensurate
68°; s	760±5	1105±15	1.99	Commensurate
68°; p	1210±10	740±20	3.16	Incommensurate

Table 3.2: Lattice parameters for hexagonal arrays of 620 nm PS particles. Larger errors in the *b*-parameter reflect the oscillatory movement of the entire array during trapping.

In the absence of interference fringes, 620 nm PS particles formed an incommensurate hex2 array, similar to that formed in *p*-pol. The *p*-pol hex2 array had more defects along the periphery of the array, while array particles in orthogonally polarised fields were observed to fill edge defects more freely. It appears that particle-fringe interactions affect particle dynamics and act to stabilise the hex1 array observed in *s*-pol, but optical binding leads to the incommensurate hex2 array observed in *p*-pol and in the absence of interference fringes.

3.2.4.2. Arrays of 700 and 800 nm PS

For arrays of 700 and 800 nm PS, it was difficult to determine the most stable array for large numbers of particles. For larger particles, the strength of optical binding interactions dominates the behaviour of arrays,[6] and so a large number of point and line defects are stabilised in the observed arrays. Figure 3.7(a) shows a stable array of 700 nm PS containing line defects and no obvious symmetry, which finally rearranged to a hex2 array Figure 3.7 (b).
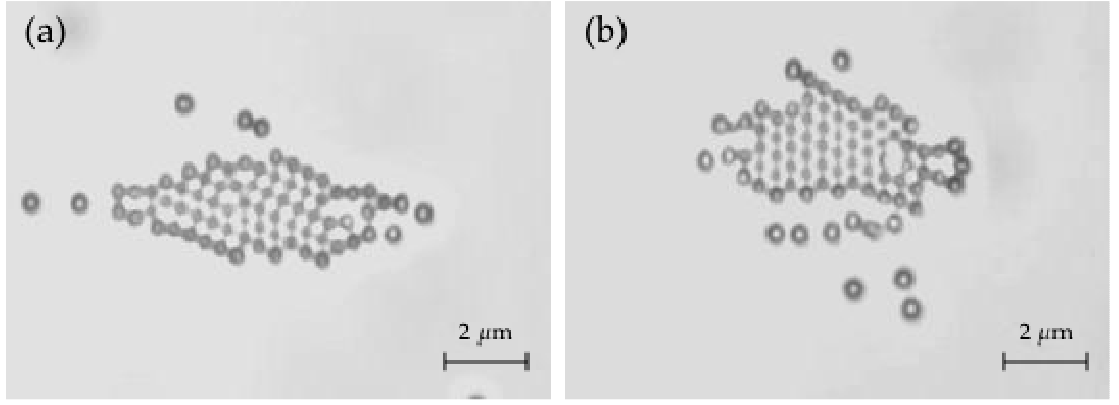
Figure 3.7: Arrays of 700 nm PS particles in *p*-pol showing (a) a stable but highly defective array; and (b) an incommensurate hex2 array that formed eventually (n_{BK7} =1.507; θ_c =62.2°; θ_i =68°°; λ=1064 nm).

Similarly, Figure 3.8(a) shows a commensurate hex2 array of 800 nm PS formed in *s*-pol (a =1460±5 nm; b =820±5 nm; D =360 nm; D/a = 4.06). On changing to *p*-pol, the hex2 array rearranged to a stable but irregular array (Figure 3.8(b)). This rearrangement raises the question of whether the hex2 array is always the lowest energy state in *p*-pol.
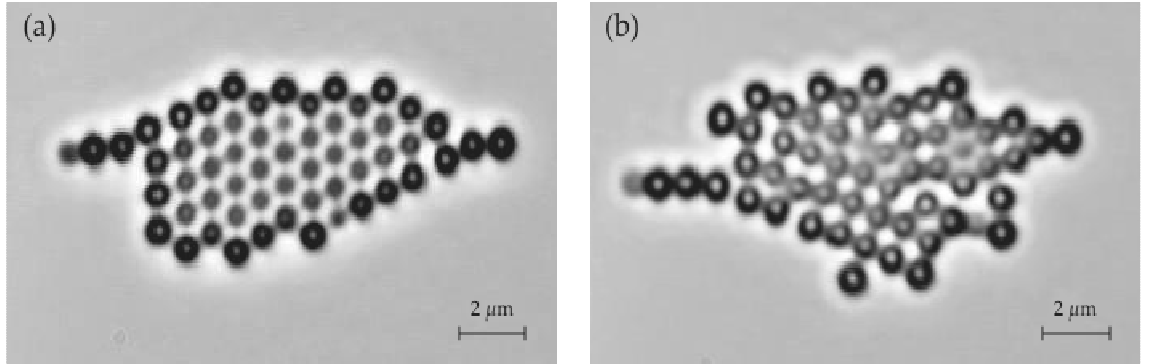
Figure 3.8: Arrays of 800 nm PS particles showing (a) in *s*-pol, a commensurate hex2 arrangement; and (b) in *p*-pol, a stable but highly defective array. (n_{SF10}=1.702; θ_i=60°; λ=1064 nm; [NaCl] =1 μM)

3.2.5. Modulated lines of larger PS (800 nm)

As PS particles diffuse into the interfering evanescent fields, they formed a line along the direction of propagation of the evanescent waves. For a line of fewer than six 800 nm PS particles, the particle separation was uniformly 1140 nm (*i.e.* 3x the interference fringe spacing). As more particles joined the line, the particles rearranged to form a modulated array of 'pairs' and 'triplets' (Figure 3.9). Adjacent particles were not separated by a multiple of the fringe spacing. However, 2nd nearest neighbours in both pair and triplet modulated lines were separated by 5D, in both p-pol and s-pol (Figure 3.9 and Table 3.3). When the forward and reflected beams were orthogonally polarised, the line had uniform particle spacing of ca. 880 nm (for n_{BK7}=1.507; θ_i=68°) which equals the shorter particle spacing in the modulated linear array, and is not a multiple of the evanescent wavelength parallel to the glass-water interface. In the absence of interference fringes, optical binding interactions account for the non-contact linear array observed. The recurrence of the same particle separation for linear arrays of 800 nm PS formed with and without interference fringes suggests that this length scale could be due to optical binding. In the presence of interference fringes, there is competition between optical binding and optical trapping forces that leads to the modulation of the linear array.

Figure 3.9: Lines of 800 nm PS particles showing (a) uniform spacings of 3D, which subsequently rearranges to (b) pairs, and (c) triplets

(n_{SF10}=1.702; θ_i=56°; λ=1064 nm; s-pol; [NaCl] =1 μM).

Incident angle, θ_i; Polarisation	Uniform separations /nm	Separations of 2nd nearest neighbours in pairs or triplets /nm	Fringe spacing, D /nm
56°; s	-	(triplet) 880 +990 =1870 =5.0D	378 (SF10)
56°; p		(triplet) 860 +930 =1790 =4.7D	
68°; p	1140 =3.0D	(pair) 905 +1030 =1935 =5.1D	382 (BK7)
		(triplet) 890 + 945 =1835 =4.8D	

Table 3.3: Particle spacings for 800 nm PS in a linear array. 2nd nearest neighbour spacings are the sum of averaged "small" and "large" adjacent particle separations as indicated in Figure 3.9(b) and (d).

3.3. Silica arrays (520 nm Silica)

In the presence of interference fringes, arrays of 520 nm silica particles were commensurate squares (a = 770 nm; b = 840 nm; a/D = 2.02). Switching between s-pol and p-pol incident light did not change the arrays observed, but did affect particle dynamics. In p-pol, the arrays grew more quickly in the y direction, while in s-pol the arrays grew faster in the x direction. Silica has a lower refractive index than PS (n_{silica} = 1.37, n_{PS} = 1.55), and so will interact less strongly with the evanescent field. The behaviour observed for 520 nm silica is qualitatively similar to that of 390 and 420 nm PS, as previously reported by Mellor.[1] No stable arrays were obtained in the absence of interference fringes.
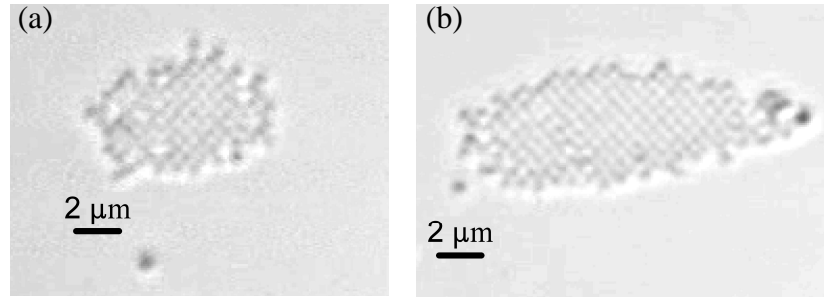
Figure 3.10: Arrays of 520nm silica particles are square and commensurate in (a) p-pol, and (b) s-pol. (n_{SF10}=1.507; θ_i=68°; λ=1064 nm)

3.4. Sterically Stabilised Microparticles

PS particles are charge-stabilised soft spheres, and so the equilibrium distance between particles in a close-packed array is affected by the electrical double-layer repulsion. Colloidal hard spheres of poly(ethylene glycol) methacrylate (PEGMA) stabilised poly-2-vinylpyridine (P2VP) microspheres were synthesised and sent to us by our collaborators.[7] Stable arrays of optically trapped 380 and 640 nm PEGMA-P2VP were obtained in both p-pol and s-pol.

3.4.1. 380 nm PEGMA-P2VP

Figure 3.11 shows a series of optically trapped arrays of 380 nm PEGMA-P2VP with interference fringes in the evanescent field. Lattice parameters (Table 3.4) indicate that arrays have the same packing in both incident polarisations, even if particle dynamics differ. Array packing is observed to depend on the evanescent field intensity as the array is formed. It is difficult to measure the incident spot size and hence to quantify the evanescent field intensity. However, by beginning experiments with a tightly focused laser spot and then translating the f = +50 mm lens (Figure 2.3(b)) to reduce the evanescent field intensity, we can still obtain a qualitative comparison of the different arrays formed at different trapping intensities. When the evanescent fields have high intensity (i.e. the incident beams are tightly focused), close-packed hexagonal arrays were formed (as shown in Figure 3.11 (a) and (b)). On reduction of the incident field intensity, either by turning the laser power down, or by defocusing the incident beams, the hexagonal array did not rearrange to a more loosely packed array. Particles on the edges of the hexagonal array seemed to be less stably trapped; sometimes diffusing out of the trapping area or rearranging to give some transient checkerboard packing. Square arrays were only formed if the hexagonal array was completely disrupted, and a new array allowed to form at lower evanescent field intensities (Figure 3.11(c) and (d)). At even lower field intensities in p-pol, a weakly bound array is observed where every other column is occupied (Figure 3.11(e)). Initially, the loosely bound array showed

small regions of square packing. As more particles joined the array, particles were more stably bound when occupying the same fringe. Eventually, rearrangements led to the loose array where every other column was occupied.
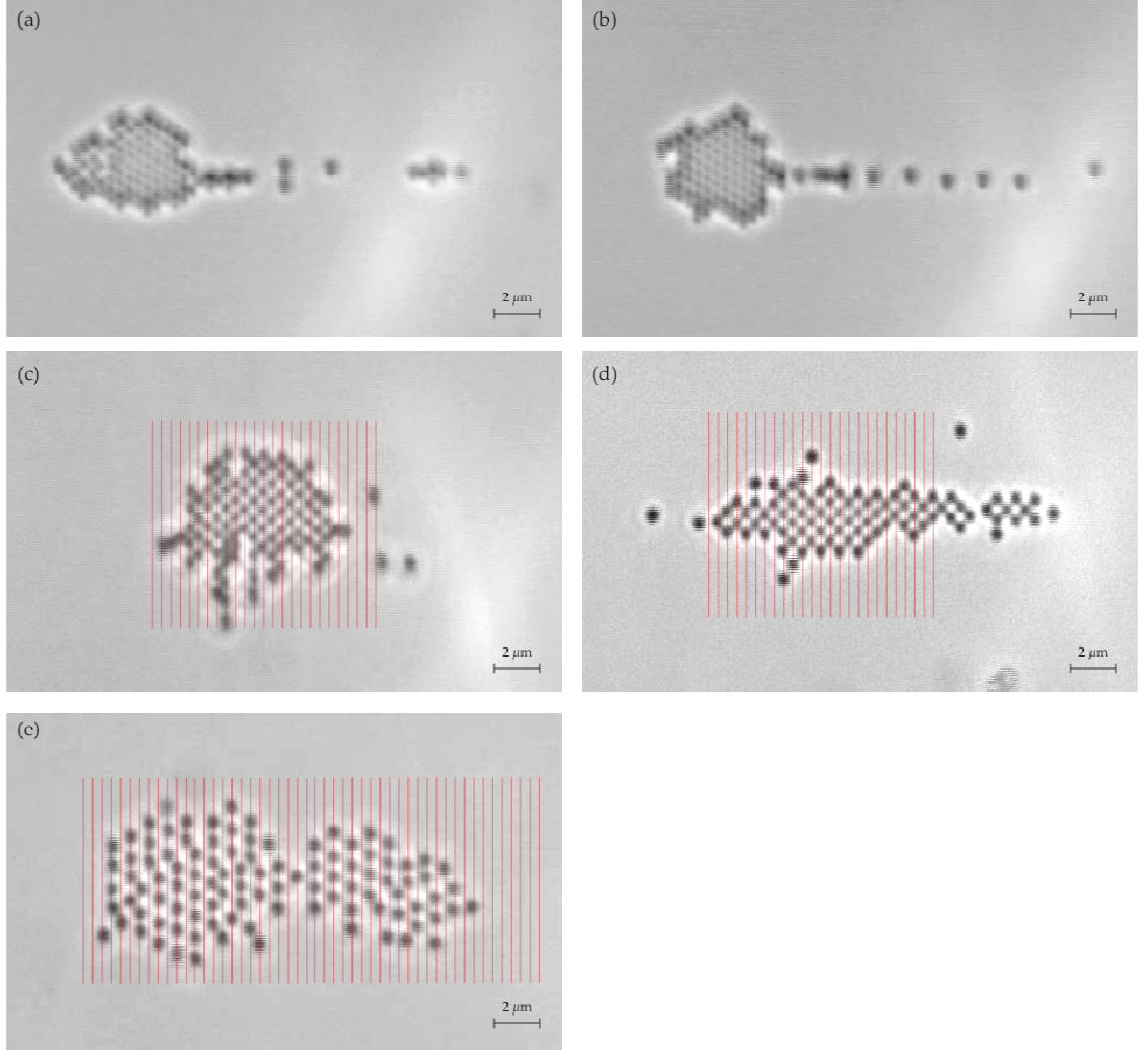

Figure 3.11: Arrays of 380 nm PEGMA-P2VP: (a),(c), and (e) are in *p*-pol; (b) and (d) are in *s*-pol. The images are ordered with decreasing field intensity (and array stability) from top to bottom. Calculated interference fringes are superimposed in red to guide the eye (n_{BK7} = 1.507; θ_i = 64.5°; λ=1064 nm).

Image	Polarisation	Array type	a /nm	a/D	b /nm
Figure 3.10 (a)	p	hexagonal	780 ±5	2.00	442 ±20
Figure 3.10 (b)	s	hexagonal	782 ±5	2.01	432 ±20
Figure 3.10 (c)	p	square	784 ±5	2.01	724 ±20
Figure 3.10 (d)	s	square	802 ±5	2.06	731 ±10
Figure 3.10 (e)	p	hex2 (column vacancies)	1563 ±10	4.01	823 ±40

Table 3.4: Lattice parameters for arrays of 380 nm PEGMA-P2VP particles, as shown in Figure 3.11. Larger errors in the b-parameter reflect the oscillatory movement of the entire array along the fringe direction during optical trapping. (n_{BK7} = 1.507; θ_i = 64.5°, D = 390 nm)

Decreasing the field intensity (equivalent to an increase in temperature) should result in the lowest energy array being formed more easily. Arrays of 380 nm PEGMA-P2VP are observed to increase in packing density as the field intensity was increased. Higher packing densities should be entropically less favourable due to a loss of particle motion about the lattice points, and so the formation of these arrays must be driven by the tight focus of the Gaussian beam leading to strong gradient forces along the y-axis.

3.4.2. 640 nm PEGMA-P2VP

Arrays of 640 nm PEGMA-P2VP were hex1 and hex2 in incident s-pol and p-pol, respectively (Figure 3.12). The commensurate hex1 array formed in s-pol sometimes underwent a non-reversible spontaneous rearrangement which resulted in an incommensurate hex2 array(Figure 3.12(c)). In s-pol, the incommensurate hex2 array was a non-contact array with a nearest neighbour separation of 783 nm. This incommensurate hex2 array is still significantly more compressed than the commensurate array formed in p-pol (Table 3.5). This is qualitatively different from the case for 620 nm PS, where a hex2 array in p-pol was incommensurate with the interference fringes (Table 3.2). Comparison of the lattice parameters in Table 3.2 and Table 3.5 indicates that the arrays were more compressed in both a and b for 640 nm PS than it was for 620 nm PEGMA-

P2VP. This is counterintuitive as the PS particles are not only larger, but are charge stabilised soft spheres. On the other hand, it is unsurprising that the incommensurate array was obtainable in both *p*-pol (as seen with 620 nm PS) and *s*-pol (as seen with 640 nm PEGMA-P2VP). Given sufficient particle numbers, optical binding interactions could eventually overcome optical trapping forces, resulting in a lowest energy array that is incommensurate.
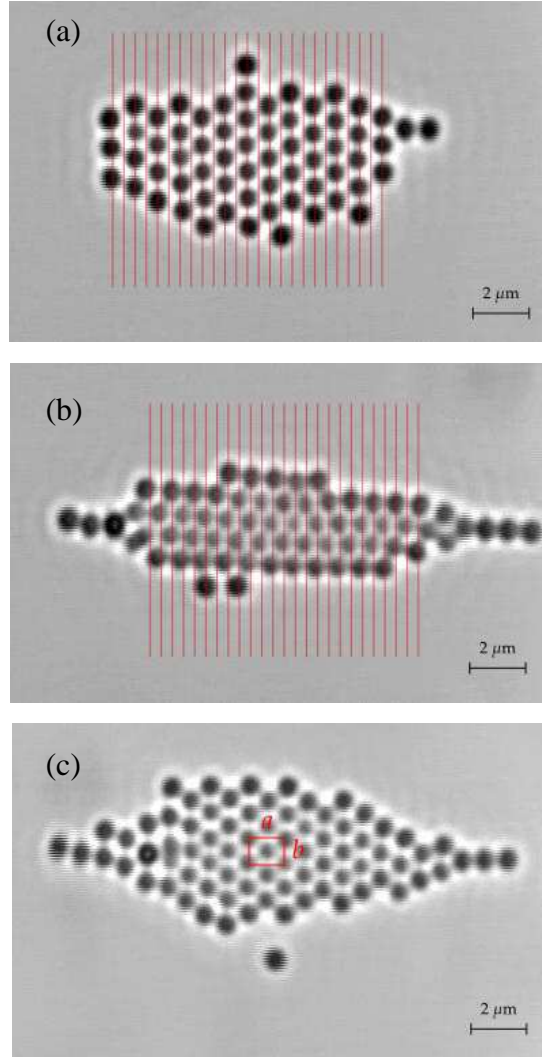

Figure 3.12: Arrays of 640 nm PEGMA-P2VP: (a) commensurate hex2 array in *p*-pol; (b) commensurate hex1 array in *s*-pol, which spontaneously rearranges to (c) an incommensurate hex2 array in *s*-pol. Calculated interference fringes are superimposed in red (n_{BK7} = 1.507; θ_i = 64.5°; λ=1064 nm).

Array	a /nm	a/D	b /nm
(a) Commensurate p-pol hex2	1550 ±10	3.97	840 ±80
(b) Commensurate s-pol hex1	785 ±10	2.01	1305 ±20
(c) Incommensurate s-pol hex2	1350 ±10	3.46	795 ±40

Table 3.5: Lattice parameters for arrays of 640 nm PEGMA-P2VP particles, as shown in Figure 3.12. Larger errors in the b-parameter reflect the oscillatory movement of the entire array along the fringe direction during optical trapping.

(n_{BK7} = 1.507; θ_i = 64.5°; λ=1064 nm; D = 390 nm)

3.5. 250 nm Au Microparticles

In this section, experiments involve the optical trapping of Au microparticles in evanescent fields. Sasaki and co-workers studied the radiation pressure exerted on an optically tweezed Au particle near an interface, with and without an applied evanescent field.[8] They showed that a metallic particle smaller than the wavelength of the evanescent field was pushed towards the interface and along the direction of propagation of the evanescent wave. The electromagnetic forces on a metallic particle near a dielectric surface were analysed by Chaumet and Nieto-Vesperinas using a coupled dipole method (CDM).[9] They predicted that at incident angles close to the critical angle, the gradient force acting on a metallic particle can be either repulsive or attractive. In the case of small particles (0.097 < ka <0.25), when the imaginary part of the permittivity is >3/2, the real part of the particle polarisability is always positive and so the gradient forces act toward the interface. At λ =1064 nm, the complex permittivity of Au is $-53.65+i4.18$,[10, 11] so we might expect stable trapping of small Au microparticles using evanescent fields.
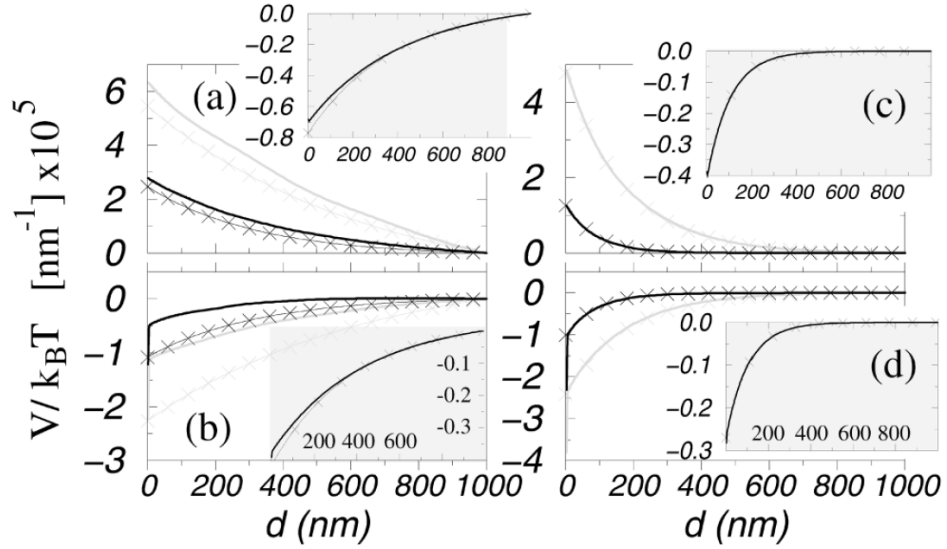
Figure 3.13: Potential energy in the vertical direction for a gold cylinder (radius $a = 125$nm) in water within an evanescent wave created under TIR (Gaussian incidence, beam waist $W_0=10$ μm). (a) $\theta_i = 62.5°$ (*s*-pol); (b) $\theta_i = 62.5°$ (*p*-pol); (c) $\theta_i = 70°$ (*s*-pol), (d) $\theta_i = 70°$ (*p*-pol). Thicker curves, interaction with the plane considered; thinner curves with crosses, no interaction with the plane. Darker curves, $\lambda = 532$ nm; lighter curves, $\lambda = 1064$ nm. Insets, the same curves for a glass cylinder in water and $\lambda = 632.8$ nm.[10]

Subsequent work by Arias-Gonzalez and Nieto-Vesperinas used multiple scattering calculations to study the forces on 250 nm Au particles located near a dielectric surface in propagating beams and evanescent waves with different polarisations[10]. Figure 3.13 shows the potential energy in the vertical direction created by a propagating evanescent field acting on a 250 nm Au cylinder in water (*i.e.* 2D model for a sphere). The angle of incidence $\theta_i = 62.5°$, in Figure 3.13(a) and (b); while $\theta_i = 70°$, in Figure 3.13(c) and (d). The respective insets correspond to a glass cylinder in water and $\lambda = 632.8$ nm. Lighter curves correspond to $\lambda = 1064$ nm (nonresonant), and darker curves correspond to $\lambda = 532$ nm (plasmon excitation), highlighting the weaker gradient potential under resonant conditions. Most remarkable in this work is the prediction that a Au cylinder would be attracted to the interface in *p*-pol, but repelled from it in *s*-pol. This is in contrast to my experimental observations, as discussed below.

In my experiments, 250 nm Au microspheres were successfully trapped by counterpropagating evanescent waves near a TIR interface when both incident beams are *p*-pol or *s*-pol. When the incident light was *s*-pol, the Au microspheres formed lines perpendicular to the interference fringes. Particles in a line occasionally 'hop' onto neighbouring particles, stacking away from the interface. Figure 3.14 a still frame captured in *s*-pol, where stacked particles were seen as larger and darker spheres than single particles. Stacked gold microspheres readily broke up into single particles and were seen to diffuse out of the trapping area (see 'Video 3.2: 250 nm Au *s*pol', which plays at 0.25x speed). Large 2D arrays of Au microspheres were not been observed in *s*-pol. Previous work by Mellor showed that PS particles form a large 2D array before particles begin to occupy a second layer.[1, 3-5] In contrast, 250 nm Au particles trapped in *s*-pol are able to stack on individual particles. In *s*-pol, there must be sufficient scattering from Au particles in the *z*-direction to allow stacking by a second particle in *s*-pol.
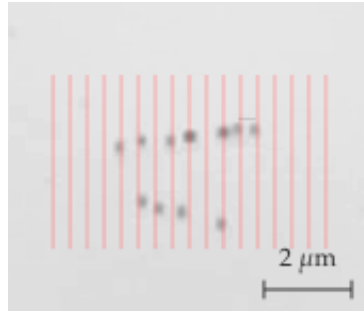

Figure 3.14: Reptating lines of 250 nm Au particles in incident *s*-pol. Stacked particles are seen as darker spots. Calculated interference fringes are superimposed in red. (n_{BK7} =1.507; θ_i =68°; D = 380 nm)

In *p*-pol, the particles form large open clusters without a regular lattice structure (Figure 3.15 and 'Video 3.3: 250 nm Au *p*pol'). The entire array experienced oscillatory motion along the interference fringe direction, but the particles were stably trapped with respect to each other. In contrast, small PS particles trapped several interference fringes apart experience uncorrelated 1D Brownian motion

along the fringes.[1, 3-5] Addition of another Au particle caused rapid

rearrangement of the array until another stable (and seemingly disordered)

configuration was found. Particle spacings are incommensurate with the

interference fringes. Nevertheless, the fringes appear to stabilize arrays of Au

microspheres since particles were not stable trapped using orthogonal
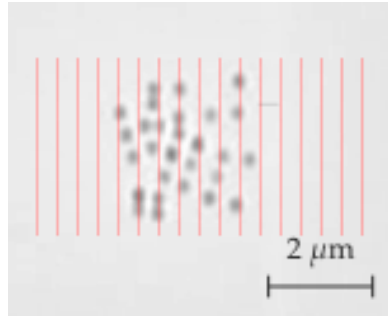
polarisations.

Figure 3.15: An open array of 250 nm Au particles in incident *p*-pol. Calculated

interference fringes are superimposed in red. (n_{BK7} =1.507; θ_i =68°; D = 380 nm)

3.6. Janus particles

Janus particles, named after the double-faced Roman god, are colloids with two sides of different chemistry or polarity.[12] The behaviour of Janus particles in our counter-propagating evanescent optical fields was of interest due to the anisotropy in refractive indices. We obtained half-Au coated 881 nm amino-modified silica microspheres courtesy of Olivier Cayre, who prepared them as follows: A dilute monolayer of silica microspheres was partially embedded in a PDMS elastomer *via* a gel trapping technique, and then coated first with a 10 nm layer of Cr and then with 20 nm of Au by thermal evaporation. The Janus particles were then retrieved using mechanical means, *i.e.* sticky-tape, washing and then centrifuge.[13]

The behaviour of Janus particles in AC fields has been studied by other researchers. In a low frequency AC field, half-Au coated PS microspheres of sizes 4.0 - 8.7 μm in water were oriented with the plane between their hemispheres aligned in the direction of the electric field, since this results in the largest induced dipole moment.[14] The Au-PS Janus microparticles then undergo induced charge electrophoresis (ICEP) motion perpendicular to the applied AC field with their dielectric hemisphere forward. Unlike homogenous particles that translate parallel to the AC field axis and are repelled from insulating walls, the Au-PS Janus microparticles were attracted towards the insulating cell walls.[15, 16]

Figure 3.16 shows the build up of an array of half-Au coated 881 nm amino-modified silica microspheres. The particles had a uniform appearance in brightfield illumination, suggesting that the plane between the Au-silica hemispheres is oriented parallel to the TIR interface. For comparison, optically trapped lines of uncoated 881 nm amino-modified silica microspheres are shown in Figure 3.17. The array of Janus particles seems qualitatively similar to that of 800 nm PS and 881 nm silica microspheres. When fewer than 6 particles

were trapped in a line, a uniform non-contact separation of 3D was observed. When more than 6 particles were trapped in a line, a modulated array of 'pairs' was once again observed, as was seen for 800 nm PS. The modulation persisted even when particles began to occupy a second row, but eventually collapsed into a close contact configuration with increasing particle numbers.

(a)

(c)

(b)

(d)
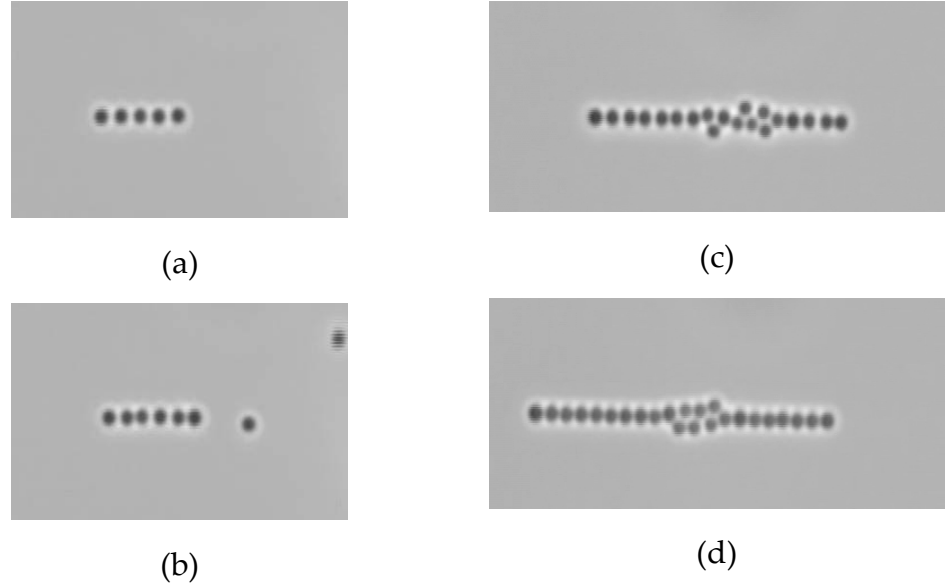
Figure 3.16: Build-up of a line of half-Au coated 881 nm silica microspheres showing (a) uniform separations of 3D; (b) modulated 'pairs'; (c) modulated separations persisting as particles sit in a 2nd row; and (d) particles in close contact as even more particles are trapped. (n_{BK7}=1.507; θ_i=64°; s-pol; λ=1064 nm)

(a)

(b)

Figure 3.17: Build-up of a line of uncoated 881 nm silica particles showing (a) uniform separations of 3D; and (b) modulated 'pairs'. (n_{BK7}=1.507; θ_i=64°; s-pol; λ=1064 nm)

Table 3.6 summarises the array spacings for half-Au coated and uncoated 881 nm silica. The modulated pair separations are slightly larger and incommensurate for the half-Au coated microspheres, but this may simply be a steric effect due to their larger size. Unfortunately, both the Janus particles and the uncoated 881 nm silica microspheres often adhere to the BK7 surface or to one another during trapping. This restricted the size of arrays that were held together purely by optically induced forces.

	Half-Au coated	Uncoated
Uniform spacing	1210±5 nm (=3.1D)	1200±5 nm (=3.1D)
Modulated pair Nearest neighbour	1125±5 nm; 965±5 nm	1050±5 nm; 950±5 nm
2nd Nearest neighbour	2090±5 nm (=5.4D)	2000±5 nm (=5.1D)

Table 3.6: Array spacings for lines of half-Au coated 881 nm amino-modified silica microspheres. (n_{BK7}=1.507; θ_i=64°; s-pol; λ=1064 nm; D =395 nm)

The behaviour of half-Au coated 881 nm silica microspheres in our evanescent wave optical traps is dominated by the behaviour of the uncoated silica microspheres. The skin depth of Au, δ is given by[17]

$$\delta = \frac{\lambda}{4\pi n'}$$
(3.1)

where n' is the complex part of the refractive index of Au. For $\dfrac{\lambda}{n_{H_2O}} = 798$ nm, n' ≈ 4.18,[10, 18] so $\delta = 15$ nm. Since the Au coating on the Janus particles is thicker than the skin depth, the half-coated hemispheres should behave like solid Au hemispheres. It is possible that the Au layer was 20 nm thick at the top, but thinner towards the equator of the Janus particle, which would contribute towards trapping behaviour that was dominated by the 881 nm silica core.

3.7. A discussion of the results presented here

In the previous sections, it can be seen that dielectric particles (PS, silica, and PEGMA-P2VP) of sizes 390-800 nm can be stably trapped in regular two-dimensional arrays. Arrays formed from smaller particles (390, 420 and 460 nm PS, and 380 nm PEGMA-P2VP) were observed to form commensurate square arrays when the beams were tightly focussed and incident close to θ_c (*i.e.* the evanescent field intensity was at its highest for the given setup). In *p*-pol and at larger incident angles, 460 nm PS were observed to form broken hex-2 arrays. These broken hex-2 arrays may be analogous to the 1-dimensional modulated lines formed by 800 nm PS. Larger dielectric particles (620, 700 and 800 nm PS, and 640 nm PEGMA-P2VP) formed hexagonal commensurate arrays, but spontaneous rearrangement to stable incommensurate arrays sometimes occurred.

The 380 and 640 nm PEGMA-P2VP arrays were all non-contact arrays, and showed similar qualitative behaviour when compared with arrays of PS particles. Arrays of sterically stabilised microspheres demonstrate that stable non-contact arrays do not result solely from a balance between optical forces acting to compress the array, and the short-range electrostatic repulsion between soft spheres.

The arrays formed by 250 nm Au colloids were surprising as they were optically bound relative to one another even when separated by relatively large distances. In contrast with the dielectric case, the individual gold colloids were able to reversibly stack away from the TIR interface in *s*-pol. This suggests that in *s*-pol there are sufficiently strong optical binding interactions perpendicular to the interface to stabilise such stacks.

References

1.   C. D. Mellor, D. Phil. Thesis, University of Oxford, 2005.

2.   J. M. Taylor, L. Y. Wong, C. D. Bain and G. D. Love, *Optics Express*, 2008, **16**, 6921-6929.

3.   C. D. Mellor, T. A. Fennerty and C. D. Bain, *Optics Express*, 2006, **14**, 10079-10088.

4.   C. D. Mellor, C. D. Bain and J. Lekner, in *Optical Trapping and Optical Micromanipulation II*, eds. K. Dholakia and G. C. Spalding, Proc. SPIE, 2005, vol. 6930, p. 352.

5.   C. D. Mellor and C. D. Bain, *Chemphyschem*, 2006, **7**, 329-332.

6.   J. M. Taylor, Doctoral thesis, Durham University, 2009.

7.   D. Dupin, S. Fujii, S. P. Armes, P. Reeve and S. M. Baxter, *Langmuir*, 2006, **22**, 3381-3387.

8.   K. Sasaki, J. I. Hotta, K. Wada and H. Masuhara, *Optics Letters*, 2000, **25**, 1385-1387.

9.   P. C. Chaumet and M. Nieto-Vesperinas, *Physical Review B*, 2000, **62**, 11185-11191.

10.   J. R. Arias-Gonzalez and M. Nieto-Vesperinas, *Optics Letters*, 2002, **27**, 2149-2151.

11.   M. A. Ordal, L. L. Long, R. J. Bell, S. E. Bell, R. R. Bell, R. W. Alexander Jr. and C. A. Ward, *Applied Optics*, 1983, **7**, 1099-1120.

12.   A. Walther and A. H. E. Muller, *Soft Matter*, 2008, **4**, 663-668.

13.   V. N. Paunov and O. J. Cayre, *Advanced Materials*, 2004, **16**, 788-791.

14.   S. Gangwal, O. J. Cayre, M. Z. Bazant and O. D. Velev, *Physical Review Letters*, 2008, **100**, 058302.

15.   M. S. Kilic and M. Z. Bazant, *Electrophoresis*, 2011, **32**, 614-628.

16.   T. M. Squires and M. Z. Bazant, *J Fluid Mech*, 2004, **509**, 217-252.

17.   H. C. v. d. Hulst, *Light scattering by small particles*, Dover, New York, 1981.

18.   M. A. Ordal, R. J. Bell, R. W. Alexander, L. L. Long and M. R. Querry, *Applied Optics*, 1987, **26**, 744-752.

4. Coherent Optical Trapping using a Ti:S Tunable Laser

Stable arrays of polystyrene microspheres were obtained using the Ti:sapphire optical trapping setup described in Section 2.2.2. In both the coherent and incoherent trapping experiments, there was a qualitative distinction between 'small' particles that form two dimensional arrays (390, 420, 460 and 520 nm PS), and 'larger' particles that form lines (620, 700 and 800 nm PS). It is therefore convenient to organise my results accordingly. Results in this Chapter have been obtained with a BK7 half-ball lens, and incident angle $\theta_i = 64.5°$. The interference fringe spacing, D, is listed in Table 2.3.

An array is commensurate with the interference fringes if lattice parameter a is an integer multiple of the fringe spacing D. However, a systematic error has been noted where the a/D values are consistently 2% lower than the nearest integer value. This is most likely a calibration error due to the use of a 1000 lines per mm diffraction grating film to calibrate the microscope. In the following discussion, if a/D is just under the nearest integer value by 4% or less, the array is considered commensurate.

4.1. Small polystyrene particles (390, 420 and 460 nm)

4.1.1. 390 nm PS

Arrays of 390 nm PS were commensurate with the interference fringes, and remain so as the wavelength was tuned from λ= 840 - 890 nm. In p-pol, particles occupied every other fringe in a hex2 array. In s-pol, arrays had a square-hex1 intermediate packing. As the wavelength (and interference fringe spacing, D) decreased in s-pol, expansion of the lattice parameter b occurred. When in s-pol at λ= 840 and 850 nm, no stable array was obtained. Since array parameter a is closely dictated by particle-fringe interaction, smaller D may act to destabilise arrays in s-pol as the particles become too large to occupy every fringe. However, in the case of 390 nm PS, the particles were too small for this to be the reason for array instability at λ= 840 - 850 nm. Larger 520 nm PS arrays were stably trapped for the full range of λ= 890 - 840 nm, with similar array spacings (Section 4.1.4).
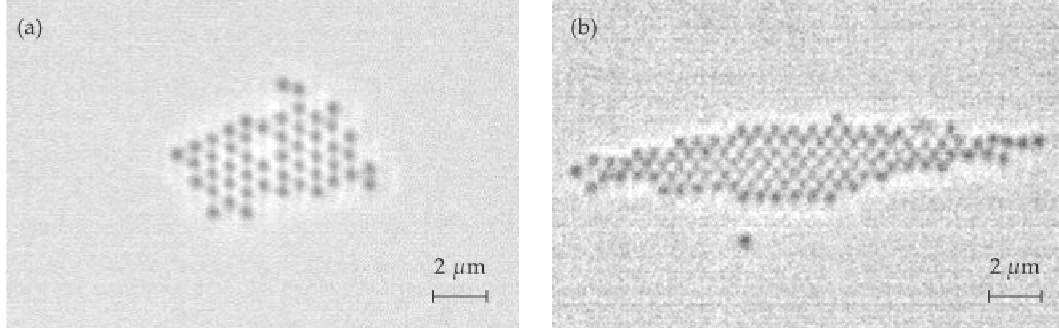
Figure 4.1: Arrays of 390 nm PS at λ= 880 nm: (a) hex2 array with every other interference fringe vacant in p-pol; and (b) square-hex1 intermediate in s-pol (n_{BK7} =1.507; θ_c =62.2°; θ_i =64.5°).

Wavelength, nm	*P*-pol			*S*-pol		
	a, nm	*a/D*	*b*, nm	*a*, nm	*a/D*	*b*, nm
890	1299±10	3.97	665±17	652±13	1.99	881±13
880	1289±7	3.99	699±23	644±13	1.99	778±15
870	1258±9	3.93	676±19	628±13	1.96	936±33
860	1240±11	3.92	696±19	622±15	1.97	955±30
850	1230±11	3.94	643±25	unstable	unstable	unstable
840	unstable	unstable	unstable	unstable	unstable	unstable

Table 4.1: Lattice parameters for arrays of 390 nm PS. Lattice parameters *a* and *b* are particle separations perpendicular and parallel to the interference fringes, respectively (n_{BK7} =1.507; θ_c =62.2°; θ_i =64.5°).

4.1.2. 420 nm PS

Arrays of 420 nm PS showed significantly different array packings and stability as the wavelength was varied. As previously discussed (Figure 1.9), PS particles are expected to experience no attraction towards bright or dark interference fringes for *ka* =1.985. This occurs for 420 nm PS microspheres when incident wavelength, λ_{air} = 886 nm. Commensurate arrays of 420 nm PS are therefore expected to occur only for incident wavelengths above and below the crossover point.

The qualitative behaviour of 420 nm PS arrays in *p*-pol can be described as follows (Figure 4.2): At λ= 880 and 890 nm, large stable commensurate arrays were obtained with broken hex2 packing. When λ= 870 nm, the array was mainly an incommensurate hex2, but with some transient broken-hex2 columns that appeared for <0.1 seconds before rearranging to hex2 again. When λ= 860 nm, a large commensurate hex2 array was observed, where every other fringe was occupied. Finally, when λ= 840 and 850 nm, the arrays once again were hex2 with transient rearrangements to producing unstable broken hex2 columns. Array parameters were not calculated for these unstable hex2-broken hex2 arrays, since neither type of array was sufficiently stable to analyse more

than 5 consecutive frames. Lattice parameters for arrays of 420 nm PS in *p*-pol are shown in Table 4.2. Broken hex2 array types (λ= 880 and 890 nm) are assigned doublet or triplet corresponding to repeating arrays with vacancies every third or fourth column, respectively. For broken hex2 arrays, *a* is quoted as two numbers: The smaller number is the distance between adjacent occupied fringes, and the larger number is the distance between occupied columns when separated by a vacant fringe. *a*/*D* for a broken hex2 array is the sum of both distances divided by the interference fringe spacing.

Wavelength, nm	Array type	*P*-pol		
		a, nm	*a*/*D*	*b*, nm
890	Broken hex2 (doublet)	411±9; 557±8	2.96	646±36
	Broken hex2 (triplet)	401±8; 499±8	3.98	633±33
880	Broken hex2 (doublet)	415±9; 549±8	2.98	619±22
	Broken hex2 (triplet)	395±7; 485±7	3.95	606±20
870	Hex2	864±22	2.70	582±26
860	Hex2	1240±13	3.92	667±25
850	Hex2 (transient broken)	Unstable	-	-
840	Hex2 (transient broken)	Unstable	-	-

Table 4.2: Lattice parameters for 420 nm PS trapped using coherent *p*-pol trapping beams (n_{BK7} =1.507; θ_c =62.2°; θ_i =64.5°). For broken hex2 arrays, *a* is quoted as two numbers: The smaller number is the distance between adjacent occupied fringes, and the larger number is the distance between occupied columns when separated by a vacant fringe. *a*/*D* for a broken hex2 array is the sum of both distances divided by the interference fringe spacing.
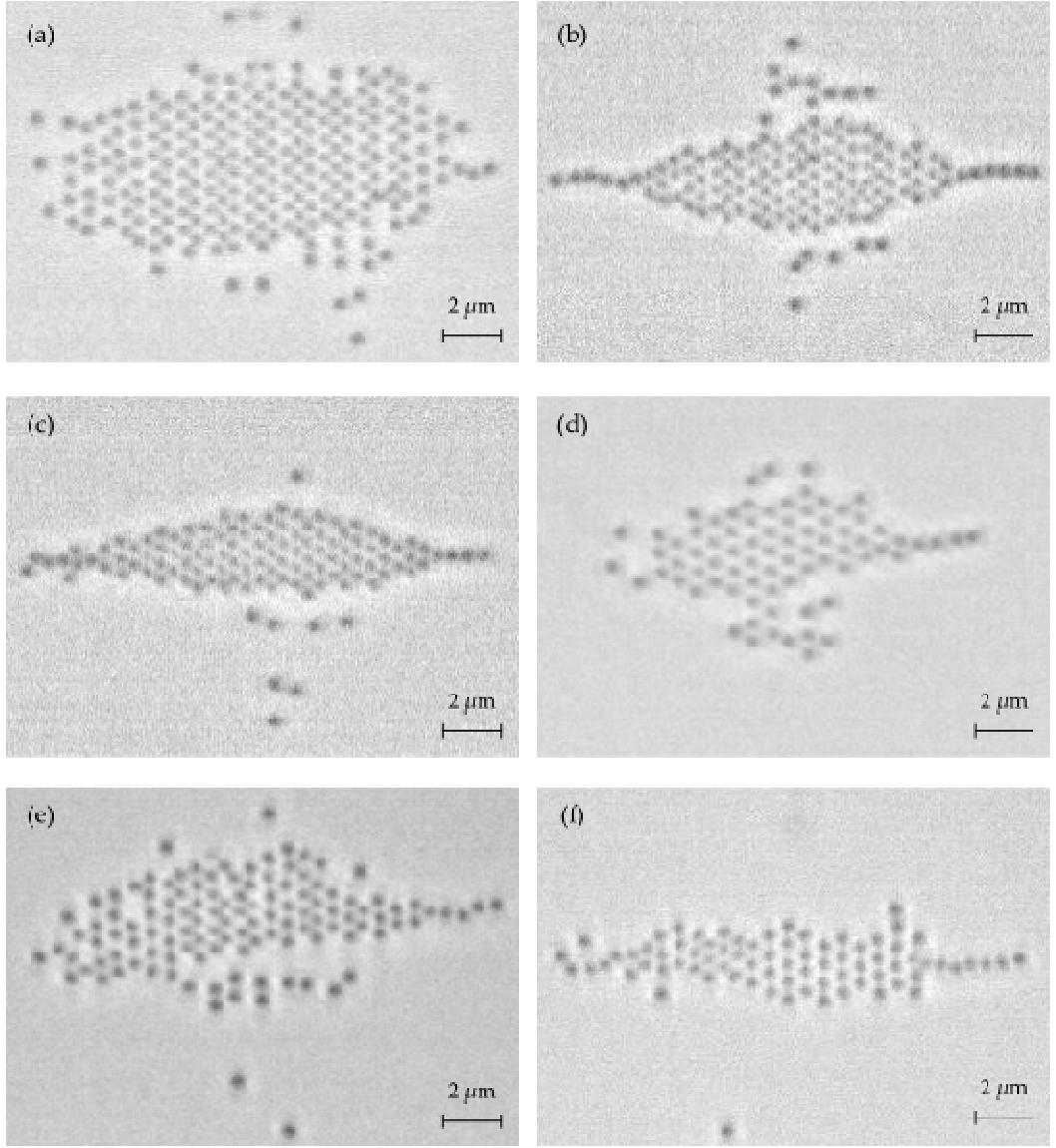
Figure 4.2: Arrays of 420 nm PS in *p*-pol at: (a) λ= 890 nm showing broken hex2; (b) λ= 880 nm showing broken hex2; (c) λ= 870 nm showing an incommensurate hex2; (d) λ= 860 nm showing an incommensurate hex2; (e) λ= 850 nm showing hex2 with transient broken hex2 structure; and (f) λ= 840 nm showing hex2. (n_{BK7} =1.507; θ_c =62.2˚; θ_i =64.5˚).

The qualitative behaviour of 420 nm PS arrays in *s*-pol can be described as follows: At λ= 890 nm, a large stable commensurate square-hex1 intermediate array was obtained. At λ= 880 nm, a large commensurate square-hex1 intermediate array was still obtained but with transient rearrangements to hex2 array and back via rotation of the unit cell. The large square-hex1 array also showed instability with respect to compression along the *y*-axis (interference fringe direction), which resulted in particles forming a two-layered array. At λ= 870 nm, the array packing was exactly hex1, but was incommensurate. The hex1 array also underwent compression along the *y*-axis, and thus formed a second trapped layer. At λ= 860 nm, a large incommensurate hex2 array was obtained. The ends of the hex2 array (where fewer particles occupy a column) occasionally rearranged to hex1 packing and back via rotations of the unit cell. At λ= 840 and 850 nm, the arrays were observed to be commensurate hex2, but were highly unstable with respect to rotations of the unit cell. Lattice parameters for arrays of 420 nm PS in *s*-pol are shown in Table 4.3

Wavelength, nm	Array type	*S*-pol		
		a, nm	*a/D*	*b*, nm
890	Square-hex1	622±17	1.90	809±12
880	Square-hex1	637±13	1.97	874±20
870	Hex1	490±19	1.53	864±12
860	Hex2	1026±17	3.25	621±22
850	Hex2	918±33	2.94	567±28
840	Hex2	904±21	2.93	549±24

Table 4.3: Lattice parameters for 420 nm PS trapped using coherent *s*-pol trapping beams (n_{BK7} =1.507; θ_c =62.2°; θ_i =64.5°).
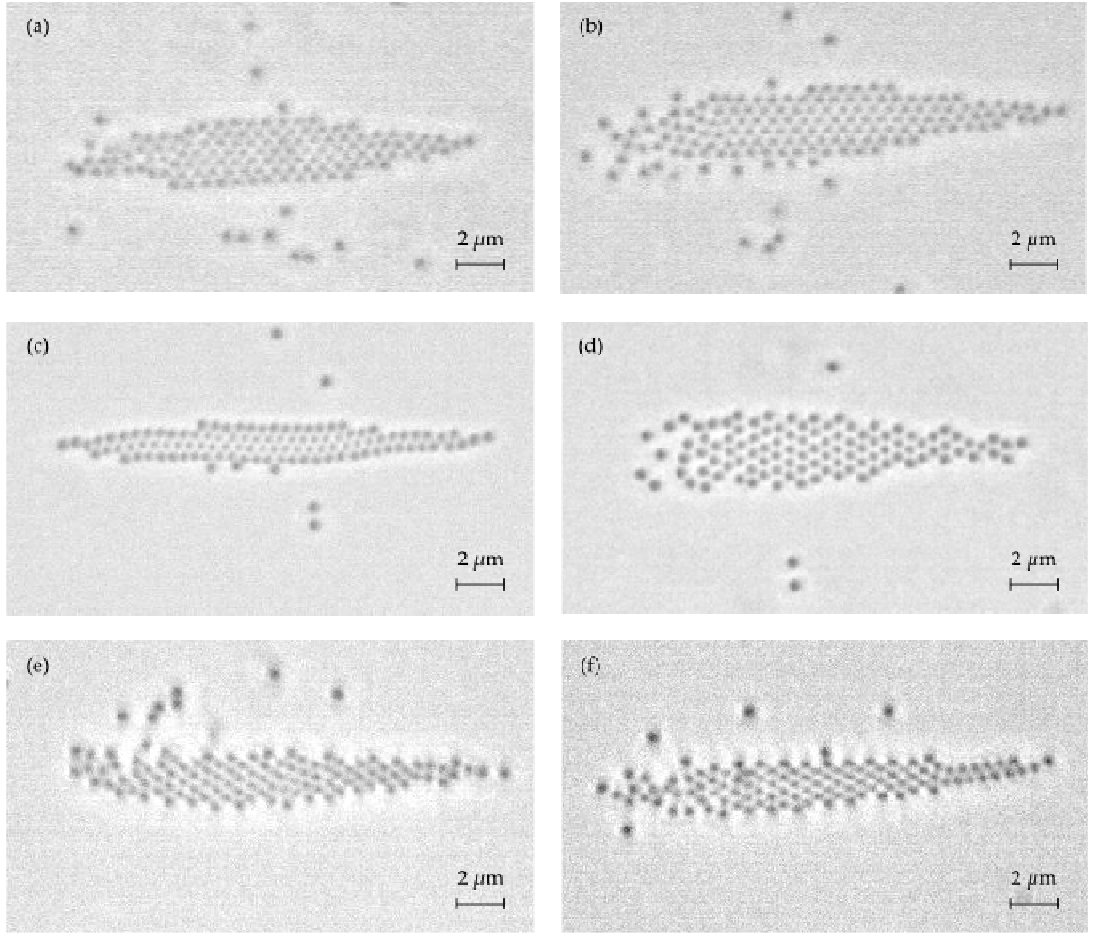
.

Figure 4.3: Arrays of 420 nm PS in *s*-pol at: (a) λ= 890 nm showing square-hex1 intermediate; (b) λ= 880 nm showing square-hex1 intermediate; (c) λ= 870 nm showing an incommensurate hex1; (d) λ= 860 nm showing an incommensurate hex2; (e) λ= 850 nm showing hex2; and (f) λ= 840 nm showing hex2. (n_{BK7} =1.507; θ_c =62.2˚; θ_i =64.5˚).

Array parameter *a* was commensurate in both *s*-pol and *p*-pol for incident wavelengths λ= 840, 850, 880 and 890 nm. At these incident wavelengths, particles positions were dictated by particle-fringe interactions. Incommensurate hexagonal arrays were obtained in *s*-pol at λ= 860 and 870 nm, and in *p*-pol at λ= 870 nm. Thus, it can be inferred that the crossover point (where individual particles experience no bright or dark fringe affinity) occurred for 420 nm PS between incident wavelengths λ= 860 to 870 nm. The theoretical crossover wavelength of λ= 886 nm is close (approximately 2% difference). The theoretical model does not account for reflection of the

85

scattered wave from the TIR interface, and this might account for the difference in crossover points.

In *p*-pol, 420 nm PS arrays were stable with respect to rotations of the unit cell. Particles scatter more strongly along the *y*-axis in *p*-pol, and this acts to stabilise particles occupying the same interference fringe.[1] In *s*-pol, the scattered field does not stabilise particles occupying the same fringe and so 420 nm PS arrays are less stable with respect to rotations of the unit cell. Rotational rearrangements occur more readily for smaller arrays or ends of larger arrays, *i.e.* where fewer particles occupy the same interference fringe, so there is still an energy barrier to such rotations that is a function of array size.

4.1.3. 460 nm PS

For λ= 860-890 nm in *p*-pol, arrays of 460 nm PS are incommensurate and have hex2 unit cells, as shown in Figure 4.4. Individual particles are not very stable within the array, as can be seen from the large errors in *a*- and *b*-parameters (Table 4.4). For λ= 840 and 850 nm in *p*-pol, no stable arrays are obtained.
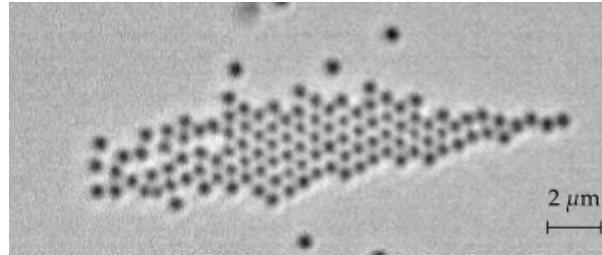
Figure 4.4: Arrays of 460 nm PS in *p*-pol at λ= 890 nm with an incommensurate hex2 packing. (n_{BK7} =1.507; θ_c =62.2°; θ_i =64.5°)

Wavelength, nm	P-pol		
	a, nm	a/D	b, nm
890	1039±48	3.18	643±49
880	1163±67	3.60	636±30
870	1033±144	3.23	625±27
860	1281±34	4.05	673±48
850, 840	Unstable	Unstable	Unstable

Table 4.4: Lattice parameters for 460 nm PS trapped using coherent *p*-pol trapping beams (n_{BK7} =1.507; θ_c =62.2°; θ_i =64.5°).

In *s*-pol, 460 nm PS initially formed long hex1 arrays (Figure 4.5). As the array increased in size beyond 3 filled rows, the hex1 array became increasingly unstable. Rotations of the unit cell from hex1 to hex2 and back were observed. Eventually, as more particles were trapped in the array, a stable incommensurate hex2 array was obtained. Table 4.5 shows the lattice parameters for both the hex1 and hex2 arrays obtained in *s*-pol. The hex1 arrays were incommensurate for λ= 880 and 890 nm, but commensurate for all other incident wavelengths. The hex2 arrays were incommensurate with no obvious trend.
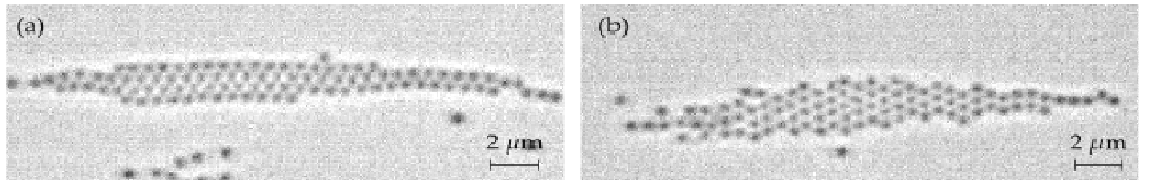
Figure 4.5: Arrays of 460 nm PS in *s*-pol at λ= 860 nm with (a) commensurate hex1; and (b) incommensurate hex2 packing. (n_{BK7} =1.507; θ_c =62.2°; θ_i =64.5°)

Wavelength, nm	Hex2			Hex1		
	a, nm	a/D	b, nm	a, nm	a/D	b, nm
890	1067±35	3.26	616±30	578±24	1.77	1033±23
880	986±49	3.05	609±32	605±19	1.87	1105±47
870	1109±16	3.47	654±21	630±18	1.97	1067±24
860	1067±35	3.38	637±27	627±22	1.98	1056±38
850	1233±18	3.90	665±22	619±18	1.98	1089±28
840	1212±18	3.92	661±44	610±18	1.97	1108±15

Table 4.5: Lattice parameters for 460 nm PS trapped using coherent *s*-pol trapping beams. Hex1 arrays were formed initially when there were 3 filled rows or less in an array. Hex2 was formed eventually as the array increases in size. (n_{BK7} =1.507; θ_c =62.2°; θ_i =64.5°)

Hex2 arrays of 460 nm PS in both *p*-pol and *s*-pol showed no obvious trend in lattice spacing with varying incident wavelength, λ or interference fringe spacing, D. However, the hex1 arrays in *s*-pol were largely commensurate, so the particles were still interacting with the interference fringes. Misalignment and loss of coherence in *p*-pol alone is not a likely cause, since the arrays are observed by switching between *s*- and *p*-pol before changing the wavelength. For 460 nm PS, ka = 2.29 and 2.16 for λ= 840 and 890 nm, respectively. At these ka values, the particles are expected to sit on dark fringes. However, ka=2.16 is not far from the crossover point and so the magnitude of the particle-fringe interaction is relatively small (see Figure 2.5). Optical binding forces are therefore more likely to overcome the particle fringe interaction, and possibly explains the incommensurate arrays observed here.

4.1.4. 520 nm PS

Arrays of 520 nm PS were stable and commensurate in both linear polarisations over the range λ= 840 - 890 nm. In *p*-pol, hex2 arrays were obtained with every other fringe occupied. In *s*-pol, a square-hex1 intermediate was obtained where lattice parameter a decreased as D became smaller, but lattice parameter b was constant (within the limits of statistical error). Array spacings for 520 nm PS

were strongly dictated by *D*, and were similar to the arrays formed by 390 nm
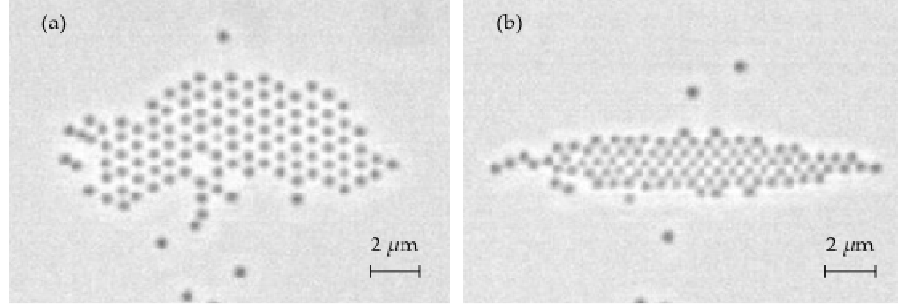PS (Section 4.1.1).

Figure 4.6: Arrays of 520 nm PS at λ= 860 nm: (a) in *p*-pol showing
commensurate hex2; and (b) in *s*-pol showing commensurate square-hex1
intermediate packing. (n_{BK7} =1.507; θ_c =62.2°; θ_i =64.5°)

Wavelength,	*P*-pol			*S*-pol		
nm	*a*, nm	*a/D*	*b*, nm	*a*, nm	*a/D*	*b*, nm
890	1300±19	3.98	695±30	649±17	1.98	847±26
880	1291±31	4.00	687±22	643±19	1.99	824±21
870	1274±15	3.98	686±50	633±18	1.96	837±14
860	1254±20	3.97	679±17	627±25	1.98	844±15
850	1243±18	3.98	673±53	619±23	1.98	854±26
840	1220±20	3.95	644±18	611±26	1.98	847±16

Table 4.6: Lattice parameters for 520 nm PS. (n_{BK7} =1.507; θ_c =62.2°; θ_i =64.5°)

4.2. Larger polystyrene particles (620, 700 and 800 nm)

Coherently trapped polystyrene particles of sizes 620, 700 and 800 nm formed line arrays. Off-axis trapping did occur, but the array became increasingly unstable and often breaks up before a full second row could be obtained. Longer arrays often displayed a flagellating motion which increased in frequency and amplitude as more particles joined the line. Taylor and Love[2] have shown that for a line of microparticles in counterpropagating Gaussian beam traps, small perturbations to the array can often be amplified and lead to off-axis circulation of the entire array. The scattered field from an off-axis particle has been simulated as an off-axis plume, which leads to other particles being drawn off-axis. In the work presented here, the flagellating motion may be an analogous case, where small perturbations are amplified by the off-axis scattering of particles in an array. Flagellating motion often led to one of several things:

- A short segment of the line breaking off, moving above/ below and rejoining the longer part of the line in a 'zipping together' motion. The long unstable line was reformed and could then repeatedly break up, and zip up.

- The line array (or a portion of it) becoming tilted relative to the x-axis. This seemed to stabilise the line with respect to flagellating motion and break up.

It was also possible to observe up to three stable line arrays in the evanescent trapping area. Stable two-dimensional arrays with regular structure have not been observed for 620, 700 and 800 nm PS using the Ti:S trapping setup, so only line arrays are discussed in this section.

Larger errors were recorded for particle spacings in line arrays. Contributing factors are:

- Line arrays consist of far fewer particles than the two-dimensional arrays of smaller PS particles. For example, the spacing quoted for a line of two particles is simply the separation averaged over 50 video frames, with its associated statistical error. For larger arrays, spacings were averaged over 50

video frames before being averaged over the number of rows or columns in that particular array. The particle spacings are therefore much more accurate for large stable arrays, and this is reflected by smaller statistical errors.

- The diffraction of light between particles that are close together can lead to asymmetric distortions of the imaged particle. Particles that are close together might therefore look further apart than they really are.

- The line arrays were less stably trapped along the y-axis, and underwent more translations and transient tilting distortions.

4.2.5. 620 nm PS

620 nm PS initially formed line arrays where particles were spaced apart, a typical example of which is shown in Figure 4.7. Particle spacings seemed to show two stable trapping length scales, one of which was commensurate while the other was just a little short of being commensurate (Table 4.7).
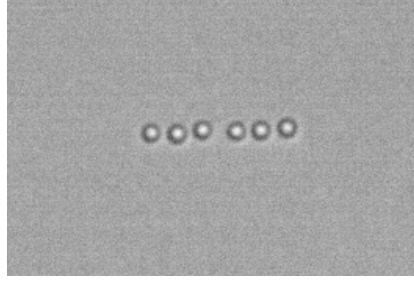
Figure 4.7: Line array of well spaced 620 nm PS at λ= 880 nm, in *p*-pol. (n_{BK7} =1.507; θ_c =62.2˚; θ_i =64.5˚)

Wavelength, nm	Polarisation	Commensurate		Incommensurate	
		a, nm	a/D	a, nm	a/D
890	*p*	977±6	2.99	1232±10	3.77
880	*p*	970±4	3.00	1257±8	3.89
850	*p*	918±2	2.94	1198±5	3.84
850	*s*	921±7	2.95	1165±23	3.73
840	*s*	921±3	2.98	1188±7	3.84

Table 4.7: Line spacings for arrays of 620 nm PS which do not contain compressed groups of particles. (n_{BK7} =1.507; θ_c =62.2˚; θ_i =64.5˚)

As the number of 620 nm PS particles increased in the line array, particles were trapped close together to form compressed groups of 2 or more particles. Within these compressed groups, particle spacings were just over $2D$, as 620 nm PS were too large to occupy every other dark fringe. When 3 or more particles were in a compressed group, particle spacings decreased below $2D$ and tended to the diameter of the microsphere. Similarly, when groups of compressed particles were next to each other, the spacing between them decreased below an integer multiple of D. Closely spaced particles in a compressed group appeared ellipsoidal, and were possibly squeezed out of the trapping plane in the z-direction(see Figure 4.8 below). (This ellipsoidal distortion is an imaging artefact due to the diffraction of light between closely spaced particles. The optical forces are too weak to actually deform PS microspheres.)
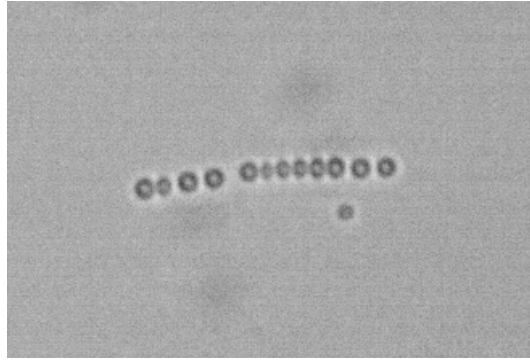
Figure 4.8: Line array of 620 nm PS at λ= 880 nm, in *p*-pol. A group of five particles is seen to be clustered together and appear ellipsoidal. The most closely spaced particles are only 620 nm apart, and are possibly squeezed out of the trapping plane in the z-direction. (n_{BK7} =1.507; θ_c =62.2°; θ_i =64.5°)

Wavelength, nm	Polarisation	Spaced		Compressed	
		a, nm	a/D	a, nm	a/D
890	p	931±5	2.85	676±7	2.07
	s	963±4	2.94	683±6	2.09
880	p	953±6	2.95	667±4	2.07
	s	936±5	2.90	681±10	2.11
870	p	934±7	2.92	682±7	2.13
	s	939±3	2.94	676±4	2.11
860	p	922±3	2.92	655±8	2.07
	s	931±3	2.95	653±7	2.06
850	p	918±2	2.94	736±5	2.36
	s	921±7	2.95	729±10	2.34
840	p	918±5	2.97	645±16	2.09
	s	-	-	-	-

Table 4.8: Line spacings for arrays of 620 nm PS which contain compressed groups of particles. 'Spaced' refers to particle spacings between single particles or between compressed groups. 'Compressed' refers to particle spacings within a tightly packed group. (n_{BK7} =1.507; θ_c =62.2°; θ_i =64.5°)

Table 4.8 lists the particles spacings for lines of 620 nm PS which contain compressed groups of particles. Lines of 620 nm PS were commensurate, as particle positions are strongly dictated by the interference fringes. The occurrence of compressed particle groups was often asymmetric about the centre of the trap. The presence of interference fringes provided an energy barrier to rearrangement of the line array, and so provided some kinetic stabilisation of asymmetric lines.

4.2.6. 700 and 800 nm PS

Line arrays of 700 and 800 nm PS are commensurate in both s-pol and p-pol, with particle separations of approximately 3D, 4D or 5D (Table 4.9 and Table 4.10). Particles did not form compressed groups, as was observed for 620 nm PS. This may simply be a consequence of larger particle size, or it may also indicate relatively weaker particle-fringe interaction (as one would expect for 700 nm PS from looking at Figure 2.5). Line arrays of 700 nm PS were distinctly less stable

with respect to particles hopping between fringes, and so in some cases particle spacings were calculated using as few as 15 consecutive video frames. Figure 4.9 and Figure 4.10 show line arrays of 700 and 800 nm PS, respectively.

Wavelength, nm	P-pol		S-pol	
	a, nm	a/D	a, nm	a/D
890	961±8, 1287±12, 1603±5	2.94, 3.94, 4.90	954±10, 1285±8	2.92, 3.93
880	944±4, 1254±5, 1578±13	2.92, 3.88, 4.89	924±15, 1266±10, 1606±17	2.86, 3.92, 4.97
870	966±8, 1253±4, 1569±8	3.06, 3.97, 4.97	1269±11	3.97
860	970±5, 1211±7, 1541±6	3.07, 3.83, 4.88	961±4, 1228±9	3.04, 3.88
850	963±12, 1222±12, 1536±12	3.09, 3.92, 4.92	1242±7, 1531±16	3.98, 4.91
840	915±8, 1227±5, 1505±6	2.96, 3.97, 4.87	1268±26	4.10

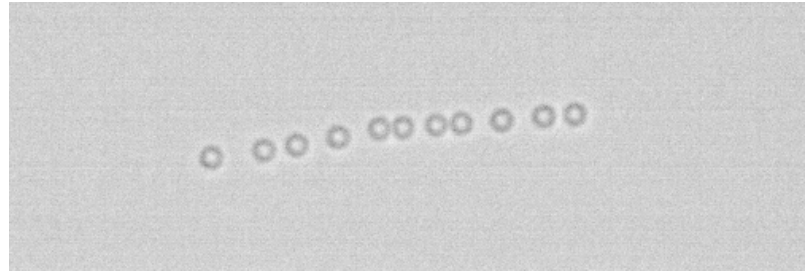*Table 4.9*: Line spacings for arrays of 700 nm PS. (n_{BK7} =1.507; θ_c =62.2°; θ_i =64.5°)

Figure 4.9: Line array of 700 nm PS at λ= 860 nm, in *p*-pol. (n_{BK7} =1.507; θ_c =62.2°; θ_i =64.5°)

Wavelength,	*P*-pol		*S*-pol	
nm	*a*, nm	*a/D*	*a*, nm	*a/D*
890	961±6, 1267±4	2.94, 3.85	984±6, 1280±7, 1594±14	3.01, 3.91, 4.87
880	958±4, 1251±7	2.96, 3.87	976±5, 1265±4, 1572±7	3.02, 3.92, 4.87
870	943±5, 1236±6, 1590±7	2.95, 3.86, 4.97	955±5, 1270±10, 1538±7	2.99, 3.97, 4.81
860	1004±6, 1522±7, 1876±7	3.18, 4.82, 5.94,	987±5, 1230±3, 1868±5	3.12, 3.89, 5.91,
850	-	-	942±5, 1205±7, 1525±5	3.02, 3.86, 4.89,
840	916±4, 1497±6, 1741±20	2.96, 4.84, 5.63	902±3, 1213±3, 1517±3	2.92, 3.92, 4.91

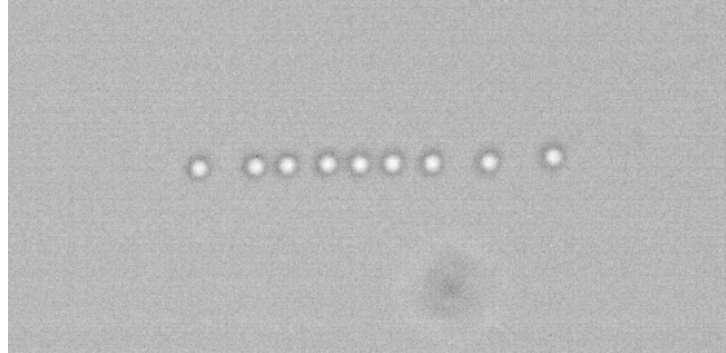*Table 4.10*: Line spacings for arrays of 800 nm PS. (n_{BK7} =1.507; θ_c =62.2°; θ_i =64.5°)

Figure 4.10: Line array 800 nm PS at λ= 860 nm, in *s*-pol. (n_{BK7} =1.507;

θ_c =62.2°; θ_i =64.5°)

References

1. J. M. Taylor, L. Y. Wong, C. D. Bain and G. D. Love, *Optics Express*, 2008, **16**, 6921-6929.

J. M. Taylor and G. D. Love, *Optics Express*, 2009, **17**, 15381-15389.

5. Incoherent Trapping using a Tunable Ti:S Laser

5.1. Small polystyrene particles (420, 460 and 520 nm)

Mutually incoherent laser beams can be used to optically trap 420, 460 and 520 nm PS particles. Stable two-dimensional arrays do not always form. Particles can still be attracted by the gradient forces, but continue 'jostling' about freely in the trapping area. A qualitative difference with the coherent trapping case is that particle movements experience no kinetic stabilisation when hopping between interference fringes. Thus, single particles and particles on the edges of the array move more readily within the trapping area.

5.1.1. 420 nm PS

Incoherent optical trapping of 420 nm PS produced a two dimensional array as shown in Figure 5.1. In *p*-pol, the arrays were hex2 with increasing stability and decreasing *a*-parameter as the incident wavelength was changed from λ= 840 nm to λ= 890 nm. In *s*-pol, the array was a tilted hex2 and a tilted hex1 at λ= 840 nm and λ= 890 nm, respectively. When λ= 865 nm in *s*-pol, the array was unstable with respect to rotations of the unit cell, and continuously rearranged between hex1 and hex2. Table 5.1 lists the lattice parameters for 420 nm PS in mutually incoherent beams. Errors associated with lattice parameter *a* showed a ten-fold increase when compared to coherently trapped arrays, due to the lack of particle-fringe interactions.

Wavelength,	*P*-pol		*S*-pol	
nm	*a*, nm	*b*, nm	*a*, nm	*b*, nm
840	1182±84	635±30	883±39	543±21
865	949±64	578±52	-	-
890	841±22	475±17	507±70	871±19

Table 5.1: Lattice parameters for incoherently trapped arrays of 420 nm PS. (*n*$_{BK7}$ *=1.507;* θ_c *=62.2˚;* θ_i *=64.5˚).*

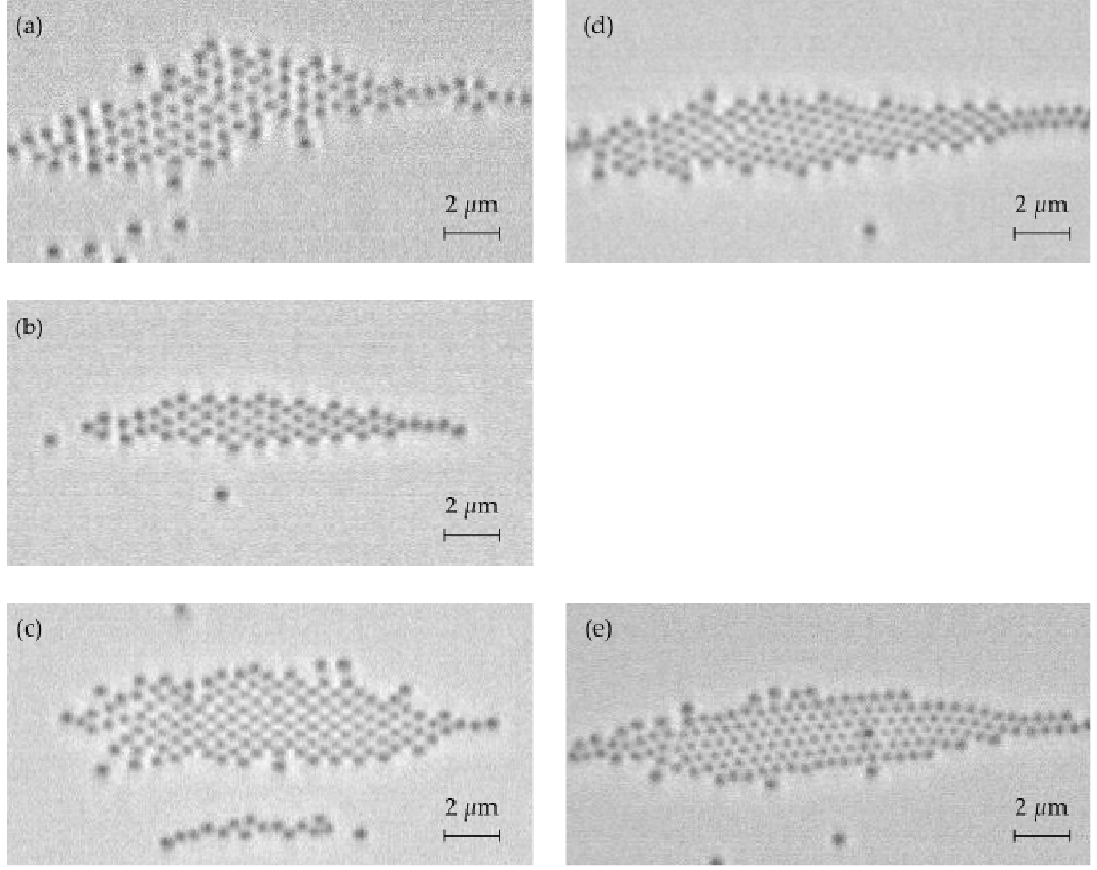*Figure 5.1:* Incoherently trapped arrays of 420 nm PS at: (a) λ= 840 nm in *p*-pol, showing hex2 with unstable columns; (b) λ= 865 nm in *p*-pol, showing stable hex-2; (c) λ= 890 nm in *p*-pol, showing stable hex-2; (d) λ= 840 nm in *s*-pol, showing tilted hex-2; and (e) λ= 890 nm in *s*-pol, showing tilted hex-1. (n_{BK7} = 1.507; θ_c = 62.2˚; θ_i = 64.5˚)

5.1.2.   460 nm PS

460 nm PS formed hex2 arrays in both polarisations, as shown in Figure 5.2. There were, however, two surprising behaviours for incoherently trapped 460 nm PS. Firstly, there was a decrease in lattice parameter a and b in s-pol as the wavelength was increased from λ= 840 nm to λ= 890 nm (Table 5.2). Secondly, the hex 2 arrays were very stable in s-pol and highly unstable in p-pol. For λ= 865 in p-pol, no stable array was observed even though a large number of particles was still localised within the trapping area.
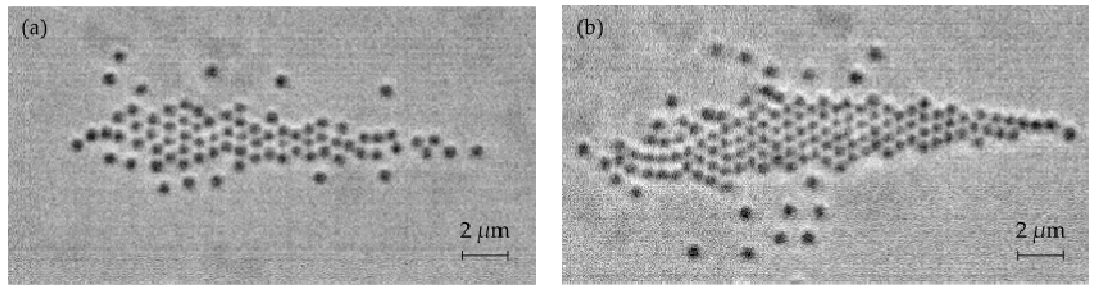

Figure 5.2: Incoherently trapped arrays of 420 nm PS at λ= 840 nm: (a) in p-pol, showing a hex2 array with unstable columns; and (b) s-pol, showing a large stable hex-2. (n_{BK7} = 1.507; θ_c = 62.2°; θ_i = 64.5°)

Wavelength,	P-pol		S-pol	
nm	a, nm	b, nm	a, nm	b, nm
840	1230±74	641±42	1068±41	639±23
865	-	-	1055±35	619±19
890	1093±97	663±36	1000±37	600±17

Table 5.2: Lattice parameters for incoherently trapped arrays of 460 nm PS. (n_{BK7} =1.507; θ_c =62.2°; θ_i =64.5°).

5.1.3. 520 nm PS

Incoherently trapped 520 nm PS formed hex2 or square-hex2 intermediate arrays in *p*-pol (Figure 5.3). At λ= 840 nm in *p*-pol, the array was hex-2. When λ= 865 nm, a hex2 array was formed initially, but this eventually rearranged to a square-hex-2 intermediate via compression in the *a* parameter. The square-hex2 intermediate array was still obtained when the incident wavelength was increased to 890 nm. In *s*-pol, no stable arrays were obtained for λ= 840 and 865 nm. Figure 5.4 shows a tilted hex1 array obtained in *s*-pol at λ= 890 nm. Lattice parameters for incoherently trapped arrays of 520 nm PS are listed in Table 5.3.
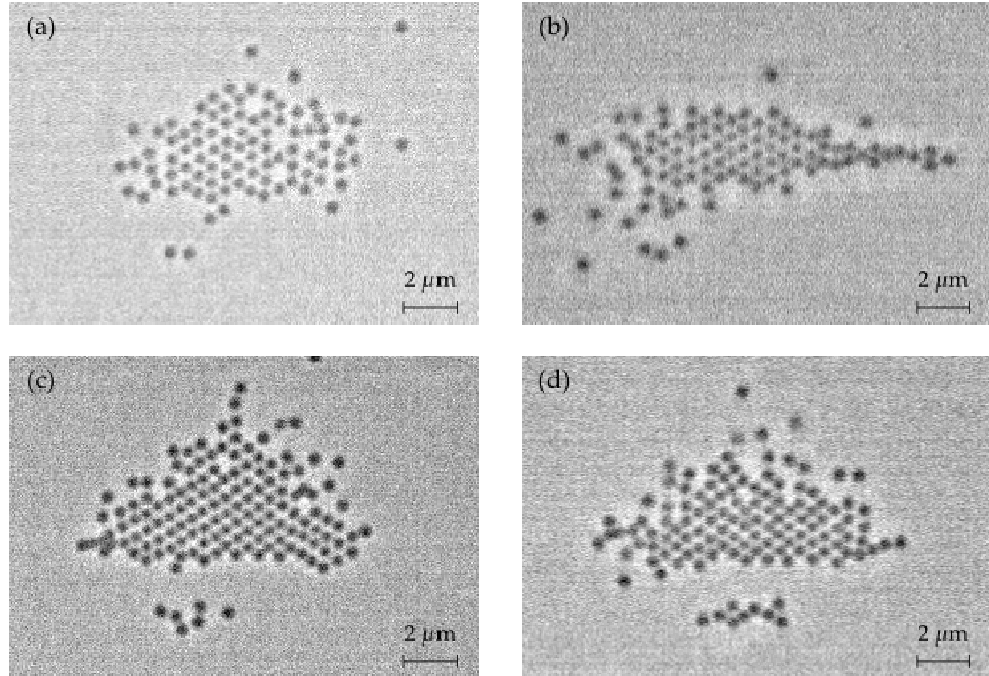

Figure 5.3: Incoherently trapped arrays of 520 nm PS in *p*-pol at: (a) λ= 840 nm, showing hex2; (b) λ= 865 nm, showing hex-2; (c) λ= 865 nm, showing square-hex-2 intermediate; and (d) λ= 890 nm, showing square-hex-2 intermediate. *(n_{BK7} = 1.507; θ_c = 62.2°; θ_i = 64.5°)*
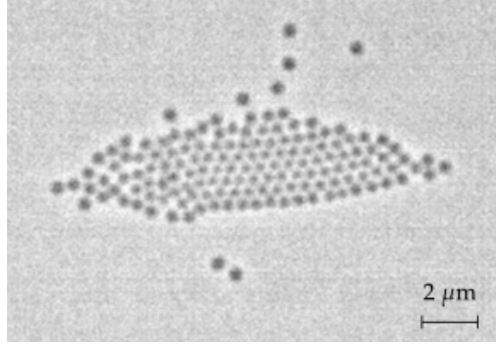
Figure 5.4: Incoherently trapped arrays of 520 nm PS in *s*-pol at λ= 890 nm, showing a tilted hex1. *(n_{BK7} = 1.507; θ_c = 62.2˚; θ_i = 64.5˚)*

Wavelength, nm	*P*-pol			*S*-pol		
	a, nm	*b*, nm	Unit cell	*a*, nm	*b*, nm	Unit cell
840	995±3	635±15	Hex2	-	-	-
865	1000±33	631±22	Hex2	-	-	-
	861±42	610±36	Square-Hex2			
890	870±40	625±43	Square-Hex2	508±71	899±18	Hex1

Table 5.3: Lattice parameters for incoherently trapped arrays of 520 nm PS. *(n_{BK7} =1.507; θ_c =62.2˚; θ_i =64.5˚).*

5.1.4.   A few points regarding incoherently trapped arrays of small PS

While the lattice parameters for incoherently trapped arrays of small PS often have large errors, or follow no immediately obvious trend, it is still useful to highlight a few general observations:

- The occurrence of arrays with different unit cell orientations (*e.g.* hex1, square and hex2) is not entirely due to interference fringes. Of note is the transition from hex2 to hex1 which occurred for 420 nm PS in *s*-pol when the incident wavelength was increased from λ= 840 to λ= 890 nm (Section 5.1.1).

- There appears to be a general trend for lattice parameter *a* to decrease with increasing incident wavelength. This was often accompanied by a more stable array. While lattice parameter *a* was expected to no longer be an integer multiple of be D (and this was observed), there is no obvious reason why *a* should decrease with increasing wavelength (see Table 5.1, Table 5.2, and Table 5.3).

- Broken hex2 arrays were not observed. This is expected, since interference fringes are necessary to stabilise periodic column vacancies (Section 3.2.1).

5.2. Larger polystyrene particles (620, 700 and 800 nm)

5.2.1. Lines of 620, 700 and 800 nm PS

Incoherent trapping of 620, 700 and 800 nm PS produced stable line arrays. The qualitative behaviour of incoherently trapped lines can be described as follows:

- Individual particles move easily along the x-axis as there is no confinement due to the absence of interference fringes. However, particles in a line array still maintain non-contact separations.

- Compressed groups do not occur as for coherently trapped lines of 620 nm PS (i.e. where particles occupy dark fringes $2D$ apart when they are too large to do so).

- For lines of more than 10 particles, it was observed that particles spacings towards the middle of the array were smaller than particle spacings at the ends, as shown in Figure 5.5. This effect was symmetric about the centre of the trapping area, in contrast to the asymmetric modulation of lines observed when interference fringes were present (Section 4.1.2). Without interference fringes, the reduced particle spacing was possibly due to stronger optical binding towards the centre of the array. This effect has been previously reported for optically trapped line arrays in counterpropagating beams.[1-3]

Figure 5.6 is a scatter plot of particle spacings vs particle position for lines of 10 or more 620 nm PS particles. Figure 5.7 is a scatter plot showing minimum and maximum particle spacings divided by the incident wavelength, vs the total number of particles in an incoherently trapped line array. For 620 nm PS, there seems to be a an increased difference between the smallest and largest particle spacings for longer lines. This trend is barely obvious for 700 and 800 nm PS (Figure 5.7 (b) and (c)). Particle spacings were much less stable for incoherently trapped lines, so this experiment may need repeating before any solid conclusions can be drawn. Better sample confinement may be needed to reduce convection in the sample medium during experiments, thus reducing fluctuations in particle spacing.
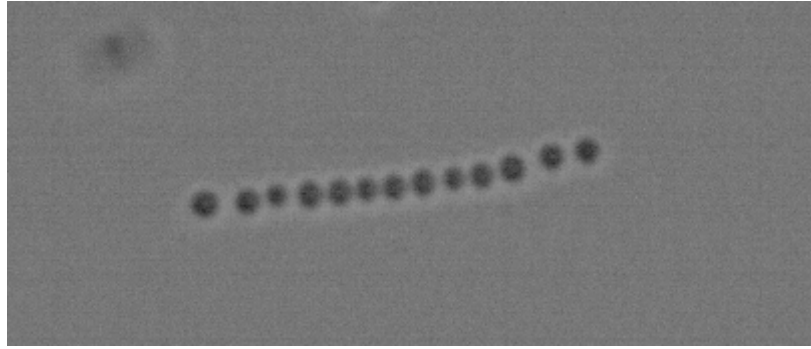
Figure 5.5: Incoherently trapped line array of 620 nm PS at λ= 865 nm, in *p*-pol. Particles spacings were seen to decrease towards the centre of the line. (n_{BK7} =1.507; θ_c =62.2°; θ_i =64.5)
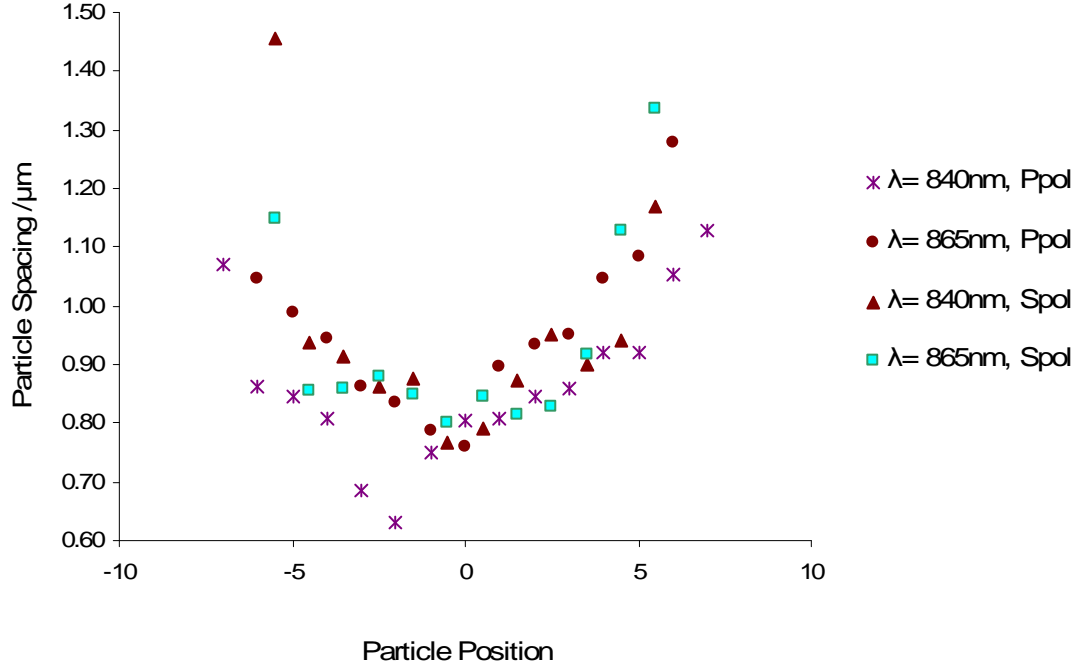
Figure 5.6: Scatter plot for particle spacings, vs particle position for lines of 10 or more 620 nm PS particles. Particle spacing is shown as the distance between adjacent particles, while particle positions are assigned so that the centre of the line array occurs at zero. If the array contains an odd number of particles, then the particle positions are integer values either side of zero. If the array contains an even number of particles, then the particle positions are *m*+0.5, where *m* is a positive or negative integer.

Figure 5.7: Scatter plot of minimum and maximum particle spacings divided by the incident wavelength, against the total number of particles in a incoherently trapped line array, for: (a) 620 nm PS; (b) 720 nm PS; and (c) 800 nm PS.

5.2.2. An open cluster of 800 nm PS

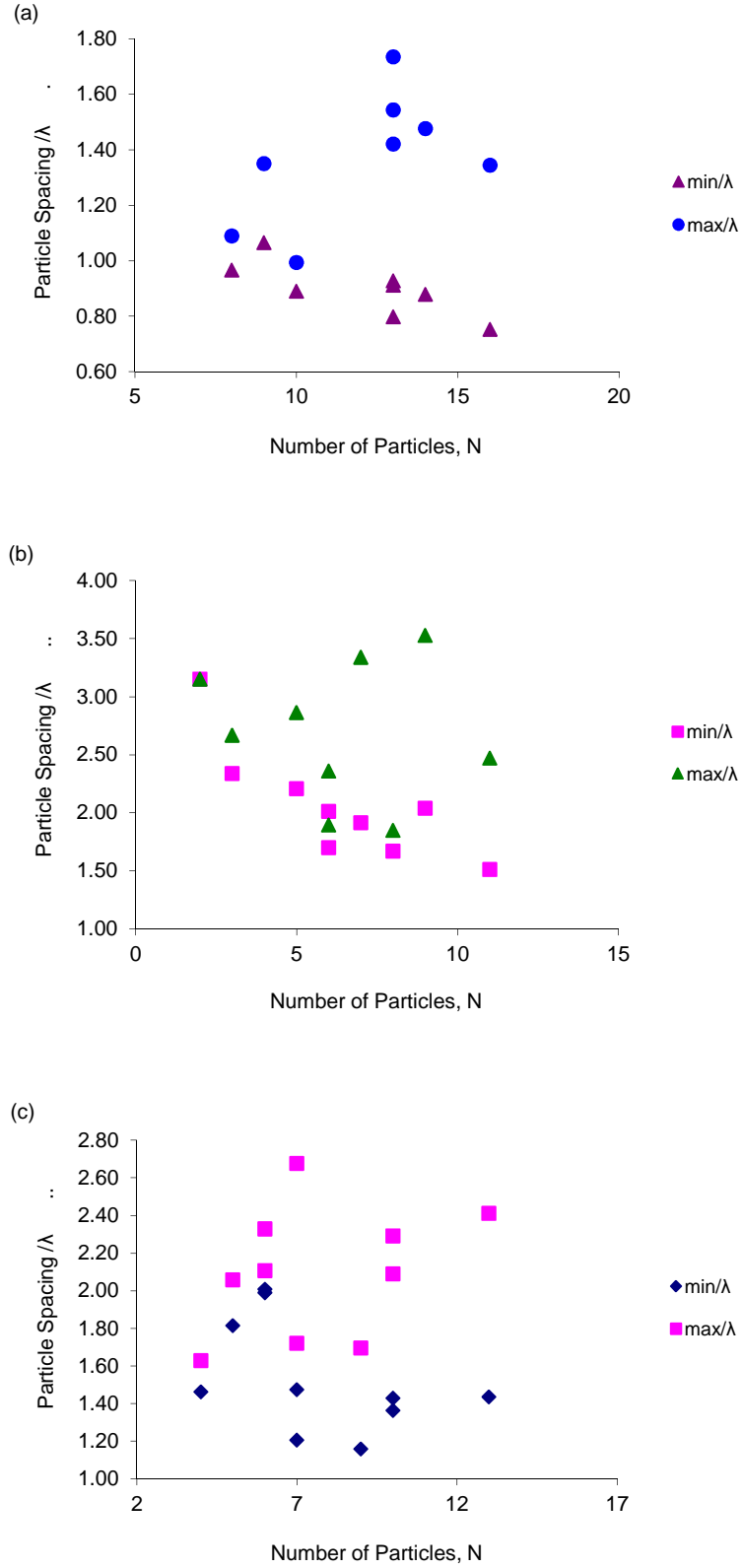Of note is the observation that during incoherent trapping stable two-dimensional arrays can be obtained (Figure 5.8 and 'Video 5.1: 800 nm incoherent open cluster'). These open clusters occurred in *p*-pol, and were observed for 700 nm PS at λ= 865 nm and 800 nm PS at λ= 840 nm. Open clusters were obtained from individual particles entering the trapping area one-by-one. Eventually, fluctuations in the system caused the open clusters to collapse, forming line arrays. The reverse rearrangement from line arrays to open clusters was not observed.

These open clusters are comparable to open clusters observed during coherent trapping of 250 nm Au (λ= 1064 nm in *p*-pol) (Section 3.5). It is remarkable that stable open clusters were observed for incoherently trapped PS (*i.e.* without the stabilisation of interference fringes), since the 250 nm Au array was unstable if orthogonally polarised beams were used.
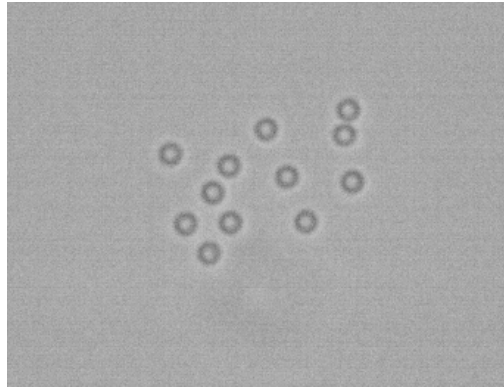
Figure 5.8: Incoherently trapped open array of 800 nm PS at λ= 840 nm, in *p*-pol. (n_{BK7} =1.507; θ_c =62.2°; θ_i =64.5)

References

1. R. Gordon, M. Kawano, J. T. Blakely and D. Sinton, *Physical Review B*, 2008, **77**, 24125.

2. M. Kawano, J. T. Blakely, R. Gordon and D. Sinton, *Optics Express*, 2008, **16**, 9306-9317.

3. J. M. Taylor and G. D. Love, *Optics Express*, 2009, **17**, 15381-15389.

6. Miscellaneous Interesting Phenomana

6.1. Optical guns

This phenomenon has been observed for 520 nm PS particles trapped in a multilayered array. When the incident angle is close to the critical angle (λ = 1064 nm; θ_i =53°; θ_c =51.6°; n_{SF10} =1.702) the penetration depth of the electric field, d_p = 640 nm, extends into the sample above a single layer array of 520 nm PS particles. Particles are seen to move from the single layer array to forming a second and even third layer of close packed particles, thus resulting in a three-dimensional multilayered array. Optical binding is a many-body, long-range interaction and as discussed previously, kinetically stable structures are readily formed during particle build up of arrays. In my experiments with 520 nm PS particles, the formation of several layers leads to a build up of strain in the array which is released by the ejection of a large number of particles from the array at speeds of ca. 130 μm s^{-1} (Figure 6.1 and 'Video 6.1: 800 nm PS popcorn'). The PS particles have low Reynolds number of approximately 10^{-4} and so the continued motion of large numbers of particles beyond the trapping area is not an inertial effect. A possible explanation is that the stream of particles ejected from the array acts as a waveguide that couples the evanescent field into a region of space beyond the incident laser spot.
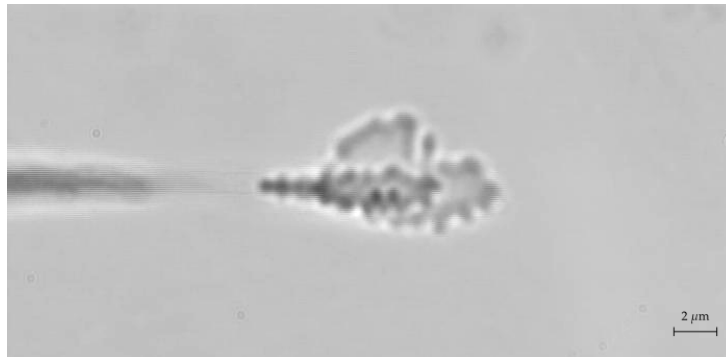
Figure 6.1: Large numbers of 520 nm PS particles being ejected at high speed from the array. *(θ_i =53°; θ_c =51.6°; n_{SF10} =1.702; λ = 1064 nm)*

6.2. Optical popcorn

This phenomenon has been observed while optically trapping arrays of 420 nm PS, 700 nm PS and 800 nm PS using the Ti:S setup (which is approximately twice the power of the λ=1064 nm Nd:YAG laser). Optical 'popcorn' sometimes forms from the most stably trapped arrays. The array is suddenly and inexplicably obscured by a large sphere, which shrinks rapidly into a cluster of particles (Figure 6.2 and 'Video 6.2: 800 nm PS popcorn'). This is not simply a large cluster that is drawn into the trapping area, as such clusters can be seen approaching the array. Secondly, there are fewer individual particles left in the array, with none having left the array by any other mechanism. It is therefore reasonable to conclude that some particles have 'popped' and then deflated. In the process, several particles become fused together. Hence, optical 'popcorn' seems to be an appropriate description.
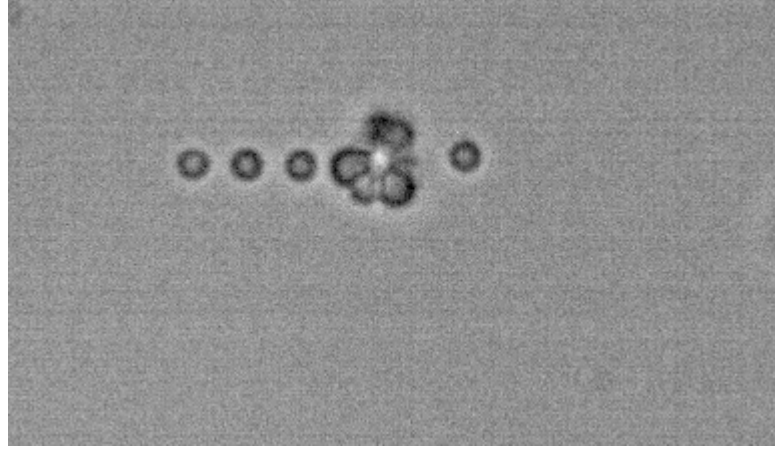

Figure 6.2: Optical 'popcorn' disrupts a line of 800 nm PS particles. (θ_i =64.5°; θ_c =62.2°; n_{BK7} =1.507; λ = 880 nm).

7. Conclusions and Further Work

In the preceding chapters, experimental observations have been presented for two different optical trapping setups (λ = 1064 nm Nd:YAG and λ = 840 –890 nm Ti:sapphire), for a number of microparticle sizes and materials. In this section, some general conclusions are presented.

i.   Increasing laser power is equivalent to lowering the temperature of the system, as the trapped particles are now in a deeper potential well. Experimental observations show that at higher laser powers fewer array types (*e.g.* 460 nm PS (Section 3.2.1))or more tightly packed arrays (*e.g.* 380 nm PEGMA-P2VP (Section 3.4))were obtained. This is counterintuitive, as one would expect a larger variety of array structures (corresponding to local potential energy minima) to be stable at low temperature (or high laser power). One explanation for these trends is that the interaction of the denser array with the field would have to lower the potential energy, since entropy is lowered also. The denser array would thus be stabilised at low temperatures (or higher laser powers) and destabilised at higher temperatures. Similarly, the more open structures would be favoured at higher temperatures due to higher potential energy but also increased entropy.

ii. There is a clear distinction between 'small' and 'large' PS microspheres that occurs for both optical trapping systems. Smaller PS particles, *i.e.* 390, 420, 460 and 520 nm, form stable two-dimensional arrays while larger PS particles, i.e. 700 and 800 nm, tend to form line arrays. Particles that are much smaller than the incident wavelength will tend to behave like dipoles which scatter according to $\sin^2 \theta_i$. Larger particles tend to interact with the field like ball lenses that refocus the light in the plane of incidence, therefore favouring the formation of lines. The tendency to form lines or plane arrays

is a function of *ka*, and so 620 nm PS was observed to form stable plane arrays for λ = 1064 nm, but not at shorter wavelengths.

iii. Hex1 arrays (*b* = √3 *a*) were observed only in *s*-pol for both optical trapping setups and all particle sizes studied. The scattered field from a particle in *s*-pol is mainly in the plane of incidence, which seems to favour hex1 packing. In *p*-pol, particles scatter significantly in the trapping plane, and this would seem to favour hex2 packing. However, trapping in orthogonal polarisations or increasing the array size in *s*-pol did lead to the rearrangement of hex1 into hex2 (Section 4.1.3). Hex1 packing also occurred for incoherently trapped arrays in *s*-pol(Section 4.1.2 and 4.1.4), so interference fringes were not necessary to stabilise the hex1 array. It is unclear why the orientation of the unit cell is sensitive to particle size, and incident polarisation. Accurate scattering calculation would be needed to explore this behaviour.

iv. Broken hex2 arrays occur in *p*-pol close to the first crossover point at which PS particles experience no force towards bright or dark fringes (*ka*=1.985). This is true for both optical trapping setups. When λ=1064 nm, broken hex-2 was observed for 460 and 520 nm PS, corresponding to *ka* = 1.81 and 2.05, respectively. When λ=890 nm, broken hex-2 was observed for 420 nm PS, corresponding to *ka* = 1.98. In *p*-pol, there is significant scattering along the fringe direction, which acts to stabilise chains of particles occupying the same bright fringe. The particles sizes that do form broken hex2 arrays are too large to sit on every fringe. The result of these two effects is that the lowest energy array is one containing column vacancies.

v. Coherent trapping of larger PS microparticles produced lines with modulated structures. For λ=1064 nm, 800 nm PS formed modulated lines with 'pair' or 'triplet' groupings due to a balance of optical trapping and optical binding forces. Adjacent 800 nm PS particles in modulated lines

showed incommensurate particles spacings, which could be attributed to optical binding. However, the repeating unit (i.e. distance between pairs + distance within pairs) was commensurate. These modulated lines can be thought of as the 1D equivalent of the broken hex array, which is also due to competing forces from optical trapping and binding (Section 3.2.4). For λ=840-890 nm, 620 nm PS formed lines which contained compressed groups of particles. While these compressed groups appear similar to those observed for 800 nm PS (λ=1064 nm), adjacent particles for lines containing 'pairs' and 'triplets' of 620 nm PS (λ=840-890 nm) are commensurate. However, as more particles join the compressed group, the particle spacing deviates from a multiple of D. The highly compressed groups (of more than three 620 nm PS particles) are possibly stabilised by optical binding, and are analogous to the incommensurate 'pairs' and 'triplets' observed for 800 nm PS (λ=1064 nm).

vi. Open arrays were observed for 250 nm Au (λ=1064 nm, p-pol)(Section 3.1) and 800 nm PS (λ=840 nm, p-pol, incoherent beams)(Section 5.2). The open cluster of 250 nm Au particles periodically rearranged due to random fluctuations (*e.g.* Brownian motion or laser power). The rearranged array was also stable but still had no repeating unit. This is possibly due to multiple energy minima separated by small energy barriers arising from significant higher order scattering by Au particles. Similarly, the open cluster of 800 nm PS was kinetically stabilised, as it eventually rearranged to a line array.

Optically trapped colloidal arrays showed highly complex and diverse behaviours which can be externally controlled by varying ka, incident polarisation, particle refractive index, or the mutual coherence of the evanescent fields. However, experimental work continues to provide anomalous arrays that are not yet accounted for with robust simulation. There continues to be much

room for experimental and theoretical work into understanding optical binding, as it could prove to be a powerful tool for the study of colloids, biological systems or even photonic crystals.

Further studies into phenomena associated with optical binding might include investigations such as:

i.   Experimental demonstration of fringe affinity of single and multiple particles based on the theoretical predictions of Taylor, as described in Chapters 1 and 2.

ii. Theoretical validation of the experimental observations made in Chapters 3 to 6, as some of the observed array behaviours remain unexplained.

iii. A more controlled and quantitative experimental study of different array stabilities as a function of number of trapped particles, incident polarisation, field intensity, and particle refractive index.